First Principles Studies of Complex Oxides for Energy Applications

BY

ALEJANDRO FEDERICO RÉBOLA
M.S. (University of Illinois at Chicago) 2009

THESIS

Submitted in partial fulfillment of the requirements
for the degree of Doctor of Philosophy in Physics
in the Graduate College of the
University of Illinois at Chicago, 2013

Chicago, Illinois

Defense Committee:

Serdar Öğüt, Chair and Advisor
Robert F. Klie
Christoph Grein
Tom Imbo
Peter Zapol, Argonne National Laboratory

Felix qui potuit rerum cognoscere causas

ACKNOWLEDGMENTS

I would like to thank my advisor Prof. Serdar Öğüt for his extraordinary lectures, for his advice, for his constant help during my career and for his outstanding human qualities. I would also like to thank my co-advisor Dr. Peter Zapol for the opportunity he gave me to work with him at the Argonne National Laboratory during part of my PhD and to be exposed to a wonderful group of people: Dr. Glen Ferguson, Dr. John Russell, Dr. Lei Cheng, Dr. Ujjal Das, Dr. Rajeev Assary. Among them I want to specially mention and thank Dr. Hakim Iddir and Dr. Weronika Walkosz for their friendship and enlightening discussions. I am very grateful to Dr. Kopinjol Baishya for bringing my attention to the Materials Modeling Group and for his constant help and friendship. I would like to thank my family for being always there, despite the time and the distance. Finally, I would like to thank Megan for her love, kindness and support during the last three years.

TABLE OF CONTENTS

TABLE OF CONTENTS (Continued)

CHAPTER **PAGE**

LIST OF TABLES

LIST OF FIGURES

LIST OF FIGURES (Continued)

FIGURE **PAGE**

LIST OF FIGURES (Continued)

LIST OF FIGURES (Continued)

FIGURE **PAGE**

LIST OF FIGURES (Continued)

LIST OF ABBREVIATIONS

BTE	Boltzmann Transport Equation
CCO	Calcium Cobaltite $(Ca_2CoO_3)(CoO_2)_{1.62}$
DFT	Density Functional Theory
DFT+U	DFT plus a Hubbard-like Correction Term
DOS	Density of States
GGA	Generalized Gradient Approximation
FL	Fermi Level
LDA	Local Density Approximation
LDA+U	L(S)DA plus a Hubbard-like Correction Term
LGO	$LaGaO_3$
LSDA	Local Spin Density Approximation
MAO	$MgAl_2O_4$
PAW	Projector Augmented Wave
PBE	Perdew-Burke-Ernzerhof (Functional)
PBE+U	PBE plus a Hubbard-like Correction Term
P-B	Poisson-Boltzmann (Equation)
PDOS	Projected Density of States

LIST OF ABBREVIATIONS (Continued)

RS	Rock Salt
SCF	Self-Consistent Field
SOFC	Solid Oxide Fuel Cell
VASP	Vienna Ab Initio Simulation Package
YSZ	Yttria Stabilized Zirconia

SUMMARY

In this thesis, I present results and analyses of first principles calculations based on Density Functional Theory (DFT) to examine the structural, electronic and lattice properties of two complex oxide systems: the misfit-layered thermoelectric $Ca_3Co_4O_9$ (CCO) and a polar interface containing the solid oxide electrolyte $LaGaO_3$ (LGO). In Chapter 1, I present a general introduction and the motivation for the study of these systems. This is followed by a brief summary of the fundamental ideas in DFT and the different theoretical methods employed in my calculations in Chapter 2. In Chapter 3, I present results and discussion related to the electronic structure of CCO calculated by means of increasing order Fibonacci approximants. In Chapter 4, I focus on the lattice and thermal properties of this material, in particular, the calculation of the thermal conductivity by combining first principles results with the Boltzmann transport equation. In Chapter 5, I propose and analyze the computational design of a polar interface in order to increase the ionic conductivity of LGO. Finally, in Chapter 6 I present a summary and the conclusions of my studies.

CHAPTER 1

INTRODUCTION

Complex oxides have been fascinating the scientific community for many years, and they have been the subject of many experimental as well as theoretical investigations. The reasons are various. On the one hand, they exhibit a very wide range of physical properties, such as colossal magneto-resistance, two dimensional electron gas, (multi)-ferroism, superconductivity, thermoelectricity, ionic conductivity, to mention a few, which make them exceptional candidates for many technological applications. Together with the possiblity of developing better and more efficient computer memories, thermoelectric devices, transistors, solid oxide fuel cells, they open a very promising route in the quest for renewable, environmentally safe and affordable sources of energy. One of the factors that makes oxides appealing for renewable energy applications is that in many cases they can operate at high temperatures where other materials would start to decompose and usually release toxic residues to the environment. In addition, various properties of complex oxide materials can be easily tuned by decreasing/increasing the oxygen partial pressure. Many of these properties have posed scientific challenges that have not yet found a clear theoretical explanation, such as the microscopic origin of high temperature superconductivity in the cuprates [1]. Moreover, due to the many recent advances in oxide hetero-structure synthesis, new and surprising phenomena are continuously discovered by experimentalists. A recurring theme along this line is the synthesis of complex oxide structures in close proximity with each other or with conventional electronic materials giving rise to novel

and exciting phases that are not found in the initial constituents. Among the wide variety of complex oxides, in this thesis I will concentrate on transition metal oxides, in which much of the interesting physics stems from the fact that transition metal elements can be found in more than one oxidation state when bonded to oxygen.

In this thesis, I will present results and analyses of my first principles studies on two complex oxide materials that can have potential energy applications. In both studies, I will apply similar first principles methods based on Density Functional Theory (DFT), the framework and the extensions of which will be explained in some detail in Chapter 2. In spite of this similarity with respect to the main method to be employed, the research to be presented in the remaining Chapters will actually involve two approaches that are philosophically different: In the first part (Chapters 3 and 4), I will focus on the misfit-layered thermoelectric $Ca_3Co_4O_9$ (CCO), a complex bulk material composed of two incommensurate subsystems along one of the lattice dimensions resulting in a structure that is, in principle, non-periodic. In this study, mostly due to the complexity of the structure, the theory lags significantly behind the large number of experimental results. Accordingly, in Chapters 3 and 4, I will mainly investigate whether a suitable structural model can be developed in order to understand the existing experimental observations. The efforts of these sections can then be directed towards the establishment of a working basis that will enable future theoretical studies on CCO to lead or work in close synergy with experimental efforts. In the second part of the thesis (Chapter 5), I will take advantage of the well-established successes of DFT in order to guide experiment in the synthesis of a new ionically conducting material. By computational design of a heterostructure, I will explore the

possibility of enhancing the ionic conductivity of the perovskite $LaGaO_3$ (LGO). My results and possible future research directions will be summarized in Chapter 6. In the remaining part of this Chapter, I will focus on some of the basic ideas behind thermoelectricity and ionic conductivity in solid-oxide fuel cells and how these desirable properties can be achieved in the two particular systems, bulk CCO and LGO interfaces, to be examined in this thesis.

1.1 Thermoelectric Materials

There is no doubt that the future of humankind depends on the development of more efficient, renewable and cleaner sources of energy. The discovery of new ways of generating energy would not only benefit the environment, and consequently improve human life, but it will also contribute to global peace and prosperity. This quest is one of the major challenges of modern science, and a great deal of effort is needed in order to find good answers. Concurrent with this search, another important problem that can be addressed is related to the observation that a large percentage of the energy we use today is lost in the form of waste heat. For instance, it is estimated that 70% of the energy consumed by a car is released as waste heat [2]. If we could reuse even part of that energy, it would be a very important gain. From thermodynamics, we know that the upper limit for the efficiency of a thermal machine is given by the efficiency of the Carnot engine. Therefore, assuming that the operational temperature of a car is of the order of 400 K (which can be verified by checking the temperature gauge of almost any car), the maximum percentage that can be recycled can thus be estimated as $(1 - 300/400) \times 100 = 25\%$, where I have assumed the temperature of the environment to be around 300 K. Although this is not a very large efficiency, in the big picture it would constitute an extraordinary progress.

Much of the interest in thermoelectric materials is due to the fact that they offer a clean and simple way to reuse part of the waste heat by converting it into electricity.

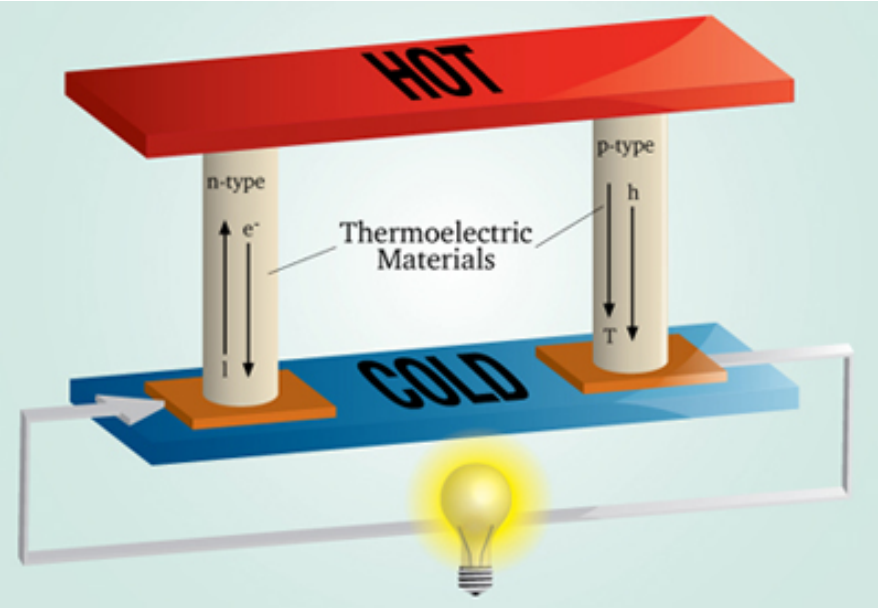

Figure 1. Schematic representation of power generation by thermoelectric materials. Two types of thermoelectrics are needed for the circuit to work: $p-$type (hole conducting) and $n-$type (electron conducting). Adapted from Texas Tech University website [3].

The capacity to convert heat into electricity is quantified by the figure of merit, defined as

$$ZT = \frac{\sigma S^2}{(\kappa_e + \kappa_l)} T, \tag{1.1}$$

where T is the temperatue, σ the electrical conductivity, and κ_l and κ_e the lattice and electronic contribution to the thermal conductivity, respectively, and S the Seebeck coefficient. The latter, also known as thermopower, is defined as $S = \frac{E}{\nabla T}$. When two ends of a material are set at

different temperatures, resulting in a temperature gradient ∇T, mobile charge carriers diffuse towards the cold region building up an electric field (E). If the carriers are electrons then a negative charge builds up at the cold end, and thus the directions of E and ∇T are opposite; if the carriers are holes, the cold end has instead a positive charge, and as a result E and ∇T point in the same direction. These two cases correspond to $p-$ ($S > 0$) and $n-$type ($S < 0$) thermoelectrics, respectively. In order to convert thermal energy into electricity it is necessary to have circuit where the two types of thermoelectrics, p and n, are simultaneously operating between the heat source and the cold side, as schematically shown in Figure 1. Typical values for the figure of merit for different materials are displayed in Figure 2. Good thermolelectrics are characterized by ZT values of 1 or above. For instance, Bi_2Te_3 exhibits a $ZT \approx 1$ at 400 K, the Bi_2Te_3/Sb_2Te_3 superlattice a $ZT \approx 2.4$ at 300K [4] and PbTe/PbSeTe quantum dots a $ZT \approx 1$, also at room temperature [5]. However, many of these popular thermoelectrics present several disadvantages: they are often unstable at higher temperatures (most materials are limited to the $200 - 700$ K range); they may decompose releasing toxic or harmful elements to the environment; many of them are made of expensive/rare constituents, which makes them unaffordable for a large number of applications.

Although a good thermoelectric material is characterized by a high Seebeck coefficient, a high electrical conductivity and a low thermal conductivity, these quantities very often compete with each other and are hard to optimize simultaneously. One of the reasons is the Wiedemann-

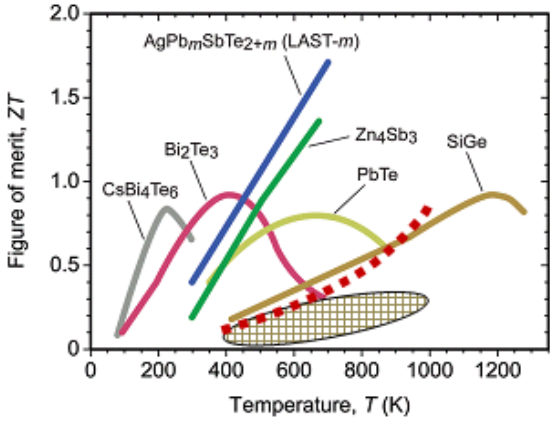

Figure 2. TE performance (in terms of ZT) of different TE materials summarized as a function of temperature [6, 7]. Cross-hatched area shows typical reported values of manganite and titanate systems [6]. The highest reported values for any metal oxide [8] to-date are indicated by the dotted line.

Franz law that relates the electrical conductivity to the electronic contribution to the thermal conductivity as

$$k_e = L\sigma T, \tag{1.2}$$

where $L = 2.44 \times 10^{-8} W\Omega K^{-2}$ is the Lorenz constant. Accordingly, reducing κ_e would also reduce σ, which would negatively affect the figure of merit. On the other hand, a high electrical conductivity is usually related to a periodic (ordered) crystal structure, which consequently would reduce the scattering rate of phonons, thus increasing the lattice contribution to the thermal conductivity, again affecting the figure of merit negatively. Last but not least, a high electrical conductivity would also tend to neutralize the electric field that results from the Seebeck effect. A way to overcome this conflict is to work with a material where one or more substructures have the electrical properties of crystalline systems while the rest behaves like an

amorphous solid, thus exhibiting a low thermal conductivity. This is known as the "Phonon-Glass and Electron-Crystal" criterion for nano-structured thermoelectrics proposed by Slack [9]. A particular type of materials that adjust to these requirements are the denominated layered-cobaltites, characterized by CoO_2 layers of CdI_2 type, made of edge-shared CoO_6 octahedra, and separated by one or more layers belonging to a distorted or disordered subsystem. A schematic of the structures of different layered cobaltites is shown in Figure 3. They can be classified by the number the number of intermediate layers between the CoO_2 sheets. Apart from the remarkable thermoelectric properties some of these type of materials exhibit (see Figure 2), layered cobaltites are in general chemically inert, very stable at high temperatures and their constituents are usually cheap and abundant on Earth, making them auspicious for technological applications. Among these materials CCO ($n = 3$ in Figure 3) stands out as the best candidate (together with Na_xCoO_2) for a $p-$type thermoelectric.

As mentioned above, Chapters 3 and 4 of this thesis will be devoted to studying the properites of the misfit-layered CCO, which is composed of two subsystems with phonon-glass/electron-crystal behavior. This complex structure offers no minor challenges for its analysis, since these two subsystems are incommensurate with each other making the whole structure non-periodic, while first principles computational methods for studying bulk materials typically rely on the underlying periodicity of the structure. In Chapter 3, I will study the electronic structure of CCO by means of increasing order rational approximants. I will show that good agreement with various experimental observations about the electronic conductivity of this material can be obtained when electron correlations are taken into account using an extension of

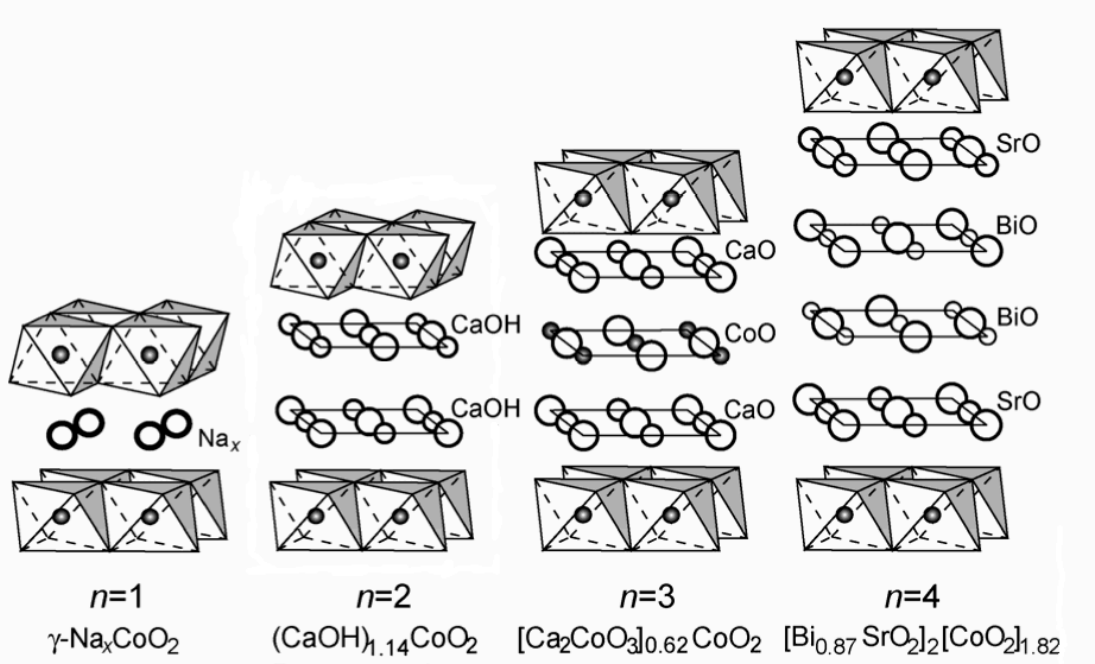

Figure 3. Schematic representation of the crystal structure of the layered cobalt oxides: n indicates the number of atomic planes in the blocking layer situated between the CoO_2 layers. CCO corresponds to the $n = 3$ layered cobaltite. Adapted from Shizuya *et al.* [10].

DFT, commonly referred to as the "DFT+U approximation". In Chapter 4, I will focus on the other aspect of the figure of merit, i.e. the thermal conductivity. I will use my conclusions from Chapter 3 in order to construct a model that makes it possible to predict the lattice and thermal properties of CCO and to validate my computations with existing experimental data.

1.2 Ionic conductors

Solid oxide fuel cells (SOFCs) are one of the most promising ways of generating clean and renewable energy in a highly efficient way. By converting stored chemical energy directly into usable electricity, they are capable of overcoming the efficiency limitations associated with combustion such as the Carnot limit mentioned in the previous section [11]. Moreover, they

mostly do not release pernicious gases to the atmosphere, or do it only in very small amounts; for example, a SOFC using H_2 as fuel would only dispose heat and water. Figure 4 shows the schematics of a typical SOFC. The fuel (H_2) is electro-oxidized at the anode and recombined with the O^{2-} ions coming from the cathode through the solid electrolyte to produce H_2O. This reaction,

$$H_2(g) + O^{2-} \rightarrow H_2O(g) + 2e^- \tag{1.3}$$

releases two electrons that via an external circuit are transfered to the cathode where molecular oxygen (present in air) is reduced to oxide ions:

$$\frac{1}{2}O_2(g) + 2e^- \rightarrow O^{2-}. \tag{1.4}$$

This mechanism is similar to that of a battery, with the difference that a SOFC works as long as a constant flow of fuel is supplied with practically no degradation. Much of the recent excitement about SOFCs comes from the fact that on stand-alone applications they can reach efficiencies of up to 65% in the conversion of chemical energy into work, which is twice the corresponding values of internal combustion engines [11]. In more sophisticated cycles that combine heat and power applications using SOFCs, the efficiency can reach values above 85%. Another remarkable advantage of SOFCs is that due to their fuel flexibility they could easily adapt to existing hydrocarbon fuel infrastructure, rising the efficiency and reducing the emission of pollutants. However, practical applications of SOFCs are limited by a high operational temperature ($\approx 900°C$). Reducing their operational temperature would result in the use of less

expensive metallic materials as interconnects, more stability and durability, since there will be less degradation and faster responses to start-up and shut-down procedures, which is one of the major limitations for their applicability in portable power and transportation markets [11, 12]. Another reason to reduce SOFC operational temperatures is the fact that the efficiency of a SOFC working at lower temperatures would increase, since it is not subject to the limitations imposed by the Carnot cycle. There is then a strong motivation to develop new SOFCs able to perform at a lower, or at least, intermediate temperatures (600-800°C).

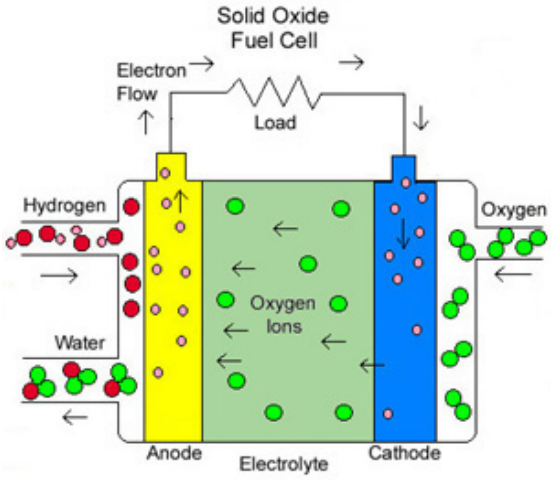

Figure 4. Schematic of a SOFC. Adapted from Earnest Garrison website [13].

As mentioned above, the basic components of a SOFC are a cathode, an anode, and a solid oxygen ion (O^{2-}) conducting electrolyte. The choice of the anode and the cathode is determined in terms of chemical and thermomechanical stabilibity with the electrolyte. Due to its high stability, the most commonly used electrolyte is YSZ (yttria stabilized zirconia).

However, since low-temperature SOFCs would require higher ionic conductivities in order to work, new and better solid electrolytes should be found. One of the best candidates is the perovskite $LaGaO_3$ (LGO), which exhibits a very high oxide ion conductivity when doped with either Sr or Mg [12]. Since the dopants have a lower valence than the substituted atoms, they require charge compensation which can be achieved by the formation of positively charged oxygen vacancies. These vacancies eventually create the empty levels that allow O^{2-} to diffuse across the electrolyte towards the anode in the SOFC. However, doping creates its own problems: Although dopants increase the number of positively charged oxygen vacancies in LGO, they can also lead to interactions (scattering, formation of clusters) that decrease their mobility, thus reducing the ionic conductivity. In this thesis, I will study the possibility of creating an alternative mechanism to increase the number of oxygen vacancies in LGO without the limitations imposed by doping. This will be the subject of Chapter 5, where the idea of a negatively charged (001) interface between LGO and $MgAl_2O_4$ (MAO) will be explored. Along the (001) direction both LGO and MAO structures can be viewed as an alternation of positively and negatively charged planes (Figure 5). It is well known that systems with a net polar charge at the interface require some charge compensation mechanism [14]. Otherwise a net total dipole moment would build up inside the material, leading to a potential that diverges proportionally to the thickness, producing what is known as the polar catastrophe. The main idea in this investigation is the possibility that positively charged oxygen vacancies could be a very favorable compensation mechanism in this interface due to the observations that both LGO and MAO are bulk insulators with large band gaps, and that all elements involved typically appear with single

valences (*e.g*, 2+, 3+, 3+, and 3+, for Mg, Al, La, and Ga, respectively) making electronic compensation an unlikely mechanism. Moreover, since vacancy formation energies are higher in MAO (as will be shown in Chapter 5), they are very likely to be located in LGO, therefore, enhancing the number of ionic carriers. Experimental work based on my computational design of this interface is currently being investigated at Argonne National Laboratory.

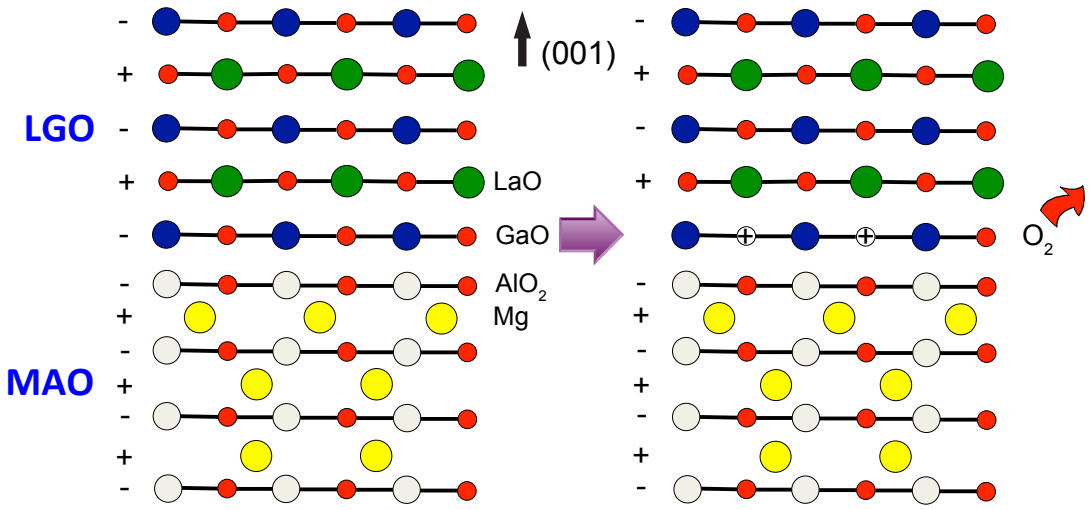

Figure 5. Schematic of a negatively charged (001) LGO//MAO interface where positively charged oxygen vacancies compensate the polarity.

CHAPTER 2

MODELING METHODS

In this chapter I present a succint overview of the theoretical methods that will be used in this thesis. I start by describing important features of Density Functional Theory (DFT), the method I have employed for my first principles studies of complex oxides materials. The Hohenberg-Kohn theorems, which establish the theoretical grounds for all the later developements in DFT, are enuntiated and briefly discussed, followed by a description of some of the different methods that make it possible to apply DFT to the study of real materials. These methods comprise the Kohn-Sham approach, exchange-correlation functionals, plane-waves and pseudopotentials, and have been demonstrated to be remarkably successful in practical applications. Next, I briefly discuss the DFT+U approach, which attempts to correct some of the problems with DFT, when applied to the study of strongly correlated systems. The final part of this chapter explains the way in which data obtained from DFT calculations can be used to evaluate different macroscopic properties of a material, such as the vibrational spectra, specific heat and thermal conductivity.

2.0.1 Interacting Electron Gas Problem

Since the times of Demokritos inquisitive people have tried to undertstand the macroscopic properties of a system in terms of its most elemental components. Such a quest involves the simultaneous understanding of, first, the fundamental properties of the microscopic individual

constituents, and, second, the way in which these constituents interact with each other in order to give rise to the macroscopic properties we observe. With the development of quantum mechanics during the first part of the twentieth century, it became possible to understand most of the fundamental properties governing single particles such as protons, electrons, photons, etc. According to quantum mechanics, the properties of a system of N particles are determined by a $3N$-variable-wavefunction obeying the Schrödinger equation. Taking into account that the number of atoms of a macroscopic material is of the order of 10^{23} ($\approx$ Avogadro's number), and that these atoms are in turn composed of nuclei and electrons, it is clear that it is no trivial task to solve the Schrödinger equation for a realistic system. A calculation involving such a number of variables will largely exceed current computational capacities. It is then necessary to resort to approximations and to an alternative approach, different from the bare wavefunction description, if we want to apply quantum mechanics to realistic systems such as solid state materials.

The full many body Hamiltonian of a solid can be expressed as [15]

$$\begin{aligned}\hat{H} = &-\frac{\hbar^2}{2m_e}\sum_i \nabla_i^2 + \sum_{i,I}\frac{Z_I e^2}{|\mathbf{r_i}-\mathbf{R_I}|} + \frac{1}{2}\sum_{i\neq j}\frac{e^2}{|\mathbf{r_i}-\mathbf{r_j}|} \\ &-\frac{\hbar^2}{2M_I}\sum_I \nabla_I^2 + \frac{1}{2}\sum_{I\neq J}\frac{Z_I Z_J e^2}{|\mathbf{R_I}-\mathbf{R_J}|},\end{aligned} \tag{2.1}$$

where lower case letters correspond to electrons and capitals to nuclei with charge Z_I and mass M_I, and m_e and e are the electron mass and charge, respectively. This Hamiltonian can be greatly simplified by noticing that since nuclei are much more massive than electrons, they

move much slower, and therefore the many body problem can be solved for the electrons only, without taking into account the motion of the nuclei. This is the so-called Born-Oppenheimer approximation. After this simplification the Hamiltonian of the many body problem is reduced to

$$\hat{H} = -\frac{\hbar^2}{2m_e}\sum_i \nabla_i^2 + \frac{1}{2}\sum_{i\neq j}\frac{e^2}{|\mathbf{r_i}-\mathbf{r_j}|} + E_{II}, \tag{2.2}$$

where E_{II} is the (constant) part of the Hamiltonian representing interaction between ions. In this way the many body problem is reduced to a merely electronic Hamiltonian that is much easier to solve. However, the many body problem thus posed is still very hard to solve for a realistic system, and therefore, it is necessary to resort to a different approach. The genius of the Density Functional Theory developed by Hohenberg, Kohn and Sham, consists in a reformulation of the problem. First, the $3N$-variables wavefunction is replaced by a density, depending only on three Cartesian components. This is achieved by means of two theorems formulated by Hohenberg-Kohn in 1964. The first theorem asserts that for any system of interacting particles the external potential V_{ext} is uniquely determined (up to an additive constant) by the ground state particle density. The second theorem establishes that the ground state density can be obtained by minimizing a universal functional of the density $n(\mathbf{r})$, which can be expressed as

$$E_{\text{HK}}[n] = T[n] + E_{\text{int}}[n] + \int d^3r V_{\text{ext}} n(\mathbf{r}). \tag{2.3}$$

However, the second of Hohenberg-Kohn theorems is a proof of existence and does not provide a practical recipe to construct the functional. In 1967, Kohn and Sham came up with the *ansatz* that triggered the development of what is now known as Density Functional Theory.

The method proposed by Kohn and Sham relies on the assumption that the ground state density corresponding to the interacting system can be represented by the ground state density of a system of non-interacting particles. In this auxiliary system the effect of interactions and correlations is contained in an effective potential, and the single particle Hamiltonian has the form (in atomic units, $\hbar = m = e = 1$)

$$\hat{H} = -\frac{1}{2}\nabla^2 + V_{\mathrm{KS}}, \tag{2.4}$$

The density can then be expressed in terms of the eigenfunctions or orbitals, ϕ_i, of this Hamiltonian

$$n(\mathbf{r}) = \sum_{i=1}^{N} |\phi_i(\mathbf{r})|^2, \tag{2.5}$$

where there is one particle per $\phi_i(\mathbf{r})$ orbital and N the total number of particles. The independent particle kinetic energy is given by

$$T_s = \sum_{i=1}^{N} \int d^3\mathbf{r} \phi_i^*(\mathbf{r}) \left(-\frac{1}{2}\nabla^2\right) \phi_i(\mathbf{r}) \tag{2.6}$$

And the total energy functional from Equation 2.3 can now be recast as

$$E_{\mathrm{KS}}[n] = T_s[n] + E_{\mathrm{Hartree}}[n] + E_{\mathrm{xc}}[n] + \int d^3\mathbf{r} V_{\mathrm{ext}} n(\mathbf{r}), \tag{2.7}$$

where

$$E_{\mathrm{Hartree}}[n] = \frac{1}{2}\int d^3\mathbf{r} d^3\mathbf{r}' \frac{n(\mathbf{r})n(\mathbf{r}')}{|\mathbf{r}-\mathbf{r}'|}, \tag{2.8}$$

and $E_{\mathrm{xc}}[n]$ is an energy functional that accounts for the effects of exchange and correlation. The effective potential is generated by all the terms on the right hand side of Equation 2.7 other than the independent-particle kinetic energy $T_s[n]$, and it is obtained by taking the variation of the sum of the energies with respect to the density

$$\begin{aligned} V_{\mathrm{KS}}(\mathbf{r}) &= \frac{\delta E_{\mathrm{Hartree}}[n]}{\delta n(\mathbf{r})} + \frac{\delta E_{\mathrm{xc}}[n]}{\delta n(\mathbf{r})} + V_{\mathrm{ext}}(\mathbf{r}) \\ &= \frac{1}{2}\int d^3r' \frac{n(\mathbf{r}')}{|\mathbf{r}-\mathbf{r}'|} + \frac{\delta E_{\mathrm{xc}}[n]}{\delta n(\mathbf{r})} + V_{\mathrm{ext}}(\mathbf{r}). \end{aligned} \tag{2.9}$$

However, one of the major challenges of DFT is that the exact form of the $E_{\mathrm{xc}}[n]$ is not known and has to be approximated. The two most popular approximations for the exchange-correlation energy will be discussed in the next section.

2.0.2 Exchange-Correlation Functionals

The great simplification introduced by the Kohn-Sham approach is that by explicitly separating long-range interactions, such as the Hartree contribution, in the expression of the total

energy (Equation 2.7), the remaining exchange-correlation part, $E_{\rm xc}[n]$, can be reasonably approximated as a local or quasilocal functional of the density

$$E_{\rm xc}[n] = \int d\mathbf{r} n(\mathbf{r}) \epsilon_{\rm xc}\left([n], \mathbf{r}\right). \tag{2.10}$$

Since according to the Hohenberg-Kohn theorem this functional should be a universal functional of the density, the value of $\epsilon_{\rm xc}\left([n], \mathbf{r}\right)$ can then be calculated by considering the exchange-correlation energy for the uniform electron gas. In this way

$$E_{\rm xc}[n] = \int d\mathbf{r} n(\mathbf{r}) \epsilon_{\rm xc}^{\rm unif}\left([n], \mathbf{r}\right), \tag{2.11}$$

and the whole problem reduces to finding accurate approximations to $\epsilon_{\rm xc}^{\rm unif}\left([n], \mathbf{r}\right)$, which can be achieved by means of Quantum Monte Carlo Methods. The simplest approximation for the exchange correlation energy assumes that this functional is local in character, and it is known as the Local Spin Density Approximation (LSDA, but often simply referred as LDA). Within LSDA Equation 2.11 can be expressed as (spin-polarized case)

$$E_{\rm xc}^{LSDA}[n^{\uparrow}, n^{\downarrow}] = \int d^3 n(\mathbf{r}) \epsilon_{\rm xc}^{\rm unif}\left(n^{\uparrow}(\mathbf{r}), n^{\downarrow}(\mathbf{r})\right) \tag{2.12}$$

where $n^{\uparrow}$ and $n^{\downarrow}$ are the charge densities corresponding to spin up and spin down electrons, respectively.

Although the LDA method should, in principle, only be applicable to systems with slowly varying densities, LDA has proven to be remarkably and unexpectedly successful in the study of many systems that do not satisfy this condition, such as atoms and molecules. The applicability of LDA to these systems is mainly justified by a good agreement with experiment, and it should always be carefully tested. Two of the reasons why LDA performs well far beyond the limits of slow varying densities are, first, the fact that it provides a reasonable approximation for the exchange-correlation hole interaction and, second, a systematic cancellation of errors due to overestimations and understimations of the exchange-correlation energy (as carefully explained in [16], p. 183). However, this cancellation is only approximate, and the overall tendency of LDA is to overestimate binding energies, which results in wrong ionization energies and smaller lattice parameters.

The first step beyond the LDA is to consider exchange-correlation energies that not only depend on the density but also on the magnitude of its gradient. This approach is known as the Generalized Gradient Approximation (GGA). The non-local functional can then be expressed as

$$E_{\mathrm{xc}}^{GGA}[n^{\uparrow}, n^{\downarrow}] = \int d^3 n(\mathbf{r}) \epsilon_{\mathrm{xc}}^{\mathrm{unif}} \left(n^{\uparrow}, n^{\downarrow}, \left|\nabla n^{\uparrow}\right|, \left|\nabla n^{\downarrow}\right|, ... \right) \tag{2.13}$$

By preserving most of the good features of LDA and by expanding it to take inhomogeneities into account, GGA methods predict atomization energies of molecules in much better agreement with experiment [17] than LDA. Numerous GGA functionals have been proposed, and the most popular are the ones developed by Becke (B88), Perdew and Wang (PW91), and Perdew, Burke, and Enzerhof (PBE). Although a significant improvent is obtained in the study of

atoms and molecules by correcting the overbinding introduced by LDA, GGA does not perform significantly better in the study of solids where the electronic density is rather uniform. In many cases it overcorrects the exchange-correlation energy making it too low, which results in an overestimation of the lattice parameters. In practical applications to real systems, in particular in the study of solids, the reason for choosing one exchange-correlation functional or the other is usually provided in the context of agreement with experimental data.

2.0.3 Plane Waves

As we saw in previous sections, by writing the Hamiltonian in terms of the electron density and by mapping the initial system into a non-interacting one, the Kohn-Sham approach allows us to simplify the many body problem considerably. In the case of solids, however, the problem thus reduced is still formidable, given the very large number of electrons and ions involved. More simplifications are needed in order to use the Kohn-Sham method in practical applications. This can be achieved (i) by taking full advange of the periodicity and the symmetry of the structure and (ii) by noticing that while the valence electrons interact with each other and with the nucleus, core electrons are almost inert and not significantly involved in bonding. In this section we will be only concerned with (i) and will leave (ii) for the next section.

First we notice that in the case of solids it is very convenient to write the Kohn-Sham orbitals in terms of plane-waves since it allows us to take full advantange of the periodicity of the structure of the crystal. According to Bloch's Theorem, the eigenstates ϕ of a one-electron

Hamiltonian $\hat{H} = -\frac{\hbar^2}{2m}\nabla^2 + U(\mathbf{r})$, where $U(\mathbf{r}) = U(\mathbf{r}+\mathbf{R})$ for all $\mathbf{R}$ in a Bravais lattice, can be expressed as [18]

$$\phi_{\mathbf{k},n}(\mathbf{r}) = e^{i\mathbf{k}\cdot\mathbf{r}} u_{\mathbf{k},n}(\mathbf{r}), \tag{2.14}$$

where the functions $u_{\mathbf{k},n}$ have the same periodicity as the potential, i.e., $u_{\mathbf{k},n}(\mathbf{r}) = u_{\mathbf{k},n}(\mathbf{r}+\mathbf{R})$, for all $\mathbf{R}$ in the Bravais lattice. Fourier transforming $u_{\mathbf{k},n}$, we obtain

$$\phi_{\mathbf{k},n}(\mathbf{r}) = e^{i\mathbf{k}\cdot\mathbf{r}} \sum_{\mathbf{G}} c_{\mathbf{k},n}(\mathbf{G}) e^{i\mathbf{G}\cdot\mathbf{r}}, \tag{2.15}$$

where $\mathbf{G}$ are the reciprocal vectors, defined by $e^{i\mathbf{G}\cdot\mathbf{R}} = 1$. The electronic density can then also be expressed in terms of these orbitals and their occupations,

$$n(\mathbf{r}) = \sum_{\mathbf{k},n} \sum_{\mathbf{G}'} f_{\mathbf{k},n} c^*_{\mathbf{k},n}(\mathbf{G}') c_{\mathbf{k},n}(\mathbf{G}) e^{i(\mathbf{G}-\mathbf{G}')\cdot\mathbf{r}}, \tag{2.16}$$

where $f_{\mathbf{k},n}$ represents the occupation of state $\phi_{\mathbf{k},n}(\mathbf{r})$. The corresponding total kinetic energy is

$$T = \frac{1}{2} \sum_{\mathbf{k},n} \sum_{\mathbf{G}} f_{\mathbf{k},n} \left| c_{\mathbf{k},n}(\mathbf{G}) \right|^2 \left| \mathbf{k}+\mathbf{G} \right|^2 \tag{2.17}$$

where the sums over $\mathbf{k}$ run over the entire Brillouin zone. Since in practical implementations we are not able to perform an infinite summation over $\mathbf{G}$ nor over a very large number of $\mathbf{k}$-points, it is necessary to set a cutoff vector for the wavefunction and to devise a clever way in order to perform summation over the Brillouin zone. The first is achieved by setting a cutoff (E_{cut})

for the kinetic energy of the plane-waves such that summations for a given **k** only run over **G** vectors that satisfy

$$\frac{|\mathbf{G}+\mathbf{k}|^2}{2} \leq E_{\text{cut}}. \tag{2.18}$$

By taking into account the point group symmetry of the crystal, **k** summations over the whole Brillouin zone can be reduced to a much smaller set of **k**-points (special **k**-points) over the so-called Irreducible Brillouin zone. Different schemes for the generation of this set of **k**-points have been proposed [19–21] but the most widely used is the one developed by Monkhorst and Pack [21], which is the scheme adopted for the calculations in this thesis.

2.0.4 Pseudopotentials

Most of the chemical and bonding properties of atoms are determined by the outer shell (or valence) electrons, while the inner shell (or core) electrons are rather inert, since they are more strongly bound and closer to the nuclei. The whole atom can then be represented by the valence electrons immersed in an effective potential (or pseudopotential) determined by the core electrons and the nucleus. In this way the many-body Hamiltonian can be simplified enormously by reducing the number of electrons. In a system of many atoms, such as a solid, the total potential experienced by the valence electrons is obtained as the sum of all the individual pseudopotentials of each atom, and this corresponds to the external potential V_{ext} appearing in the Kohn-Sham Equation (2.9).

In the previous section, I mentioned about the advantages of writing the Kohn-Sham equations in terms of plane-waves, expecting to keep the number of required wavefunctions as small as possible (without suffering much in accuracy). However, one difficulty we encounter is

that valence wavefunctions are highly oscillatory inside the core region (see [18]: p. 194) and thus their expansion in terms of plane waves would require, in principle, a very large number of terms. Luckily, this problem can be overcome using pseudopotentials and working with so-called pseudo-wavefunctions for valence states, rather than the true "all-electron" wavefunctions. This is explained briefly below:

Calling $|\psi_c\rangle$ and $|\psi_v\rangle$ the exact solutions of the Schrödinger equation for core and valence electrons, we have

$$\hat{H}\,|\psi_{c,v}\rangle = E_{c,v}\,|\psi_{c,v}\rangle \tag{2.19}$$

Our goal is to map the valence wavefunctions $|\psi_v\rangle$ into a new set of smoother functions, that can be then better approximated by a much smaller number of plane-waves. Following this idea, we define a new set of slowly varying valence wave-functions $|\phi_v\rangle$ such that

$$|\phi_v\rangle = |\psi_v\rangle + \sum_c \langle\psi_c\,|\,\phi_v\rangle\,|\psi_c\rangle \tag{2.20}$$

It is straightforward to show that the $|\phi_v\rangle$'s thus defined satisfy a Schrödinger-like equation with an effective Hamiltonian with the same eigenvalues as the original valences wave-functions

$$\hat{H}_{\text{eff}}\,|\phi_v\rangle = E_v\,|\phi_v\rangle\,, \tag{2.21}$$

where

$$\hat{H}_{\text{eff}} = \hat{H} + \sum_c (E_v - E_c)\,|\psi_c\rangle\,\langle\psi_c|\,. \tag{2.22}$$

The effective potential $\hat{v}_p$ felt by valence electrons can then be expressed as

$$\hat{v}_p = \hat{v} + \sum_c (E_v - E_c) \left|\psi_c\right\rangle \left\langle\psi_c\right| , \tag{2.23}$$

where $\hat{v}$ corresponds to the bare potential due to the nucleus. Since the second term on the right hand side of Eq. (2.22) corresponds to a repulsive potential (since $E_v > E_c$), the pseudopotential $\hat{v}_p$ felt by the valence electrons is therefore much weaker than the true potential due to the nucleus.

2.0.5 Projector Augmented Wave (PAW) Method

One of the drawbacks of the pseudopotential method outlined in the previous section is that the information on the all-electron wavefunction in the core region is lost. This can affect the calculation of different properties such as hyperfine parameters and electric field gradients. In addition, the pseudopotential method does not provide any explicit way to determine a priori the reliablity of the approximation and is, in general, subject to transferability errors. An alternative method is the projector augmented wave (PAW) method proposed by Blöchl in 1994. One of the main advantages of the PAW method is that it gives access to full wavefunctions and densities, and it is exact if a sufficient number of basis wavefunctions are considered inside the core. The main idea of PAW is to map a smooth auxiliary wavefunction $|\tilde{\psi}_n\rangle$ into the true all-electron Kohn-Sham single particle wave function $|\psi_n\rangle$ by means of an operator $\hat{T}$ such that

$$|\psi_n\rangle = \hat{T} \, |\tilde{\psi}_n\rangle \, . \tag{2.24}$$

The Kohn-Sham equation can then be written as

$$\hat{T}^\dagger \hat{H} \hat{T} \left|\tilde{\psi}_n\right\rangle = \epsilon_n \hat{T}^\dagger \hat{T} \left|\tilde{\psi}_n\right\rangle . \tag{2.25}$$

Since the true wavefunctions are already smooth at a certain distance from the core, the form of $\hat{T}$ is such that it only modifies the wavefunction close to the nuclei:

$$\hat{T} = 1 + \sum_a \hat{T}^a, \tag{2.26}$$

where $\hat{T}^a$ only acts around a certain radius around atom a (augmentation sphere). The next step is to expand the true wavefunction in a basis of partial waves $|\tilde{\phi}_i^a\rangle$ inside the augmentation spheres. For each of these partial waves a corresponding auxiliary smooth partial wave is also defined, requiring that

$$\left|\phi_i^a\right\rangle = (1 + \hat{T}^a) \left|\tilde{\phi}_i^a\right\rangle . \tag{2.27}$$

Since $\hat{T}^a$ does nothing outside the augmentation sphere, it is clear that $\phi_i^a(r) = \tilde{\phi}_i^a(r)$ in this region. After some mathematical manipulation, it can be shown that the

$$\hat{T} = 1 + \sum_a \sum_i \left(\left|\phi_i^a\right\rangle - \left|\tilde{\phi}_i^a\right\rangle \right) \left\langle \tilde{p}_i^a \right| , \tag{2.28}$$

where $\langle \tilde{p}_i^a |$ is a projector operator such that $\langle \tilde{p}_i^a | \tilde{\phi}_j^a \rangle = \delta_{i,j}$ inside the augmentation spheres. By recasting Equation 2.24, the all electron Kohn-Sham wavefunction can be expressed as

$$\psi_n(\mathbf{r}) = \tilde{\psi}_n(\mathbf{r}) + \sum_a \sum_i \left(\phi_i^a(\mathbf{r}) - \tilde{\phi}_i^a(\mathbf{r}) \right) \langle \tilde{p}_i^a | \tilde{\psi}_n \rangle \,, \tag{2.29}$$

where the smooth and numerically more convenient wavefunction $\tilde{\psi}_n(\mathbf{r})$ is obtained by solving Equation 2.25. In this way, the highly oscillatory Kohn-Sham wavefunctions are decomposed into two contributions: auxiliary wavefunctions which are smooth everywhere and a contribution which contains rapid oscillations but that only acts in the core region for each atom. As a result, within the PAW method each part can be treated separetely. Smooth delocalized wavefunctions can be efficiently represented by using coarse Fourier or real space grids (*e.g.* plane waves), while localized contributions can be expressed in terms of centered radial grids (*e.g.* Gaussians, polynomials, Bessel functions). Within the PAW method, information about the core region is not lost and the Kohn-Sham all electron wavefunctions can be retrieved at any time.

2.0.6 Corrections to DFT: DFT + U

Although the DFT methods outlined above are able to accurately describe the ground states of many materials, they fail to provide a good account of systems with strong onsite electron interactions due to highly localized orbitals. The main reason for this is that in the Kohn-Sham approach the many-body problem is mapped into a non-interacting system with a one-electron exchange-correlation assumed to be either local (LDA) or semi-local (GGA) but with no orbital dependence in the functionals. The effect of correlations is thus treated in a mean field fashion,

favoring delocalized solutions of the many body problem. The failures of this approach are more notorious in systems that contain transition metal or rare-earth elements with partially filled d (or f) shells. When applying the Kohn-Sham method with an orbital-independent potential to such a system, one typically obtains a partially filled d band with metallic structure. For example, the electronic structures of transition-metal oxides NiO and CoO have long been known to be poorly described by traditional DFT methods [22]. The calculated LDA bandgap for NiO is 0.2 eV against an experimental value near 4 eV, and CoO is predicted to be metallic, while experimentally it exhibits a 2.4 eV bandgap [22]. The application of GGA, by partly taking into account non-local effects, improves these values slightly: 0.5 and 0.8 eV for the NiO and CoO-bandgaps, respectively, but these are still considerably smaller than the corresponding experimental values.

The LDA+U method was first introduced by Anisimov *et al.* in order to include electron-electron interactions due to localized orbitals into the exchange-correlation functional [23]. Although initially applied to LDA functionals, the acronym "LDA+U" also stands for methods that involve LDA or GGA-type calculations coupled with additional orbital-dependent interactions [15]. The form of the added term in the LDA/GGA functionals is derived from a Hubbard-type Hamiltoninan model, where the additional interactions are usually considered only for highly localized atomic-like orbitals on the same site. Within this approach the total

energy is treated as a functional of the electron density as well as a function of the occupation numbers of d or f orbitals given by n_i. The simplest form of this functional is [22]

$$E_{LDA+U} = E_{LDA} - UN(N-1)/2 + U\sum_{i,j} n_i n_j \tag{2.30}$$

where the term in the middle is the mean field interaction of $d(f)$-electrons already included in E_{LDA}, and hence, has to be substracted in order to avoid double counting. The corresponding orbital energies are the derivatives of the total energy with respect to the occupations n_i: [22]

$$\epsilon_i = \partial E/\partial n_i = \epsilon_{LDA} - U\left(\frac{1}{2} - n_i\right) \tag{2.31}$$

Note that the gap between fully occupied ($n_i = 1$) and empty ($n_i = 0$) orbitals is given by the Coulomb parameter U, thus reproducing the qualitative behavior of a Mott-Hubbard insulator. In a similiar fashion we can extract the orbital dependent potential as the variations with respect to the orbital occupation

$$V_i = \delta E/\delta n_i = V_{LDA} + U\left(\frac{1}{2} - n_i\right) \tag{2.32}$$

This indicates that for occupations that are initially larger than 1/2, the U contribution to the potential is attractive, inducing electrons to localize in this particular orbital, while on the other hand if the initial occupation is smaller than 1/2 electrons the opposite occurs and empty states are favored.

2.0.7 Phonons and Finite Difference Method

At finite temperature (T), atoms forming a crystalline lattice vibrate around their equilibrium positions with an amplitude depending on the value of T. In equilibrium, the ions of a lattice are located at the sites $\vec{R}_{ni} = \vec{R_n} + \vec{\tau_i}$, where $\vec{R_n}$ are the lattice vectors and $\vec{\tau_i}$ the basis positions in the unit cell. If these ions deviate from their equilibrium positions by a small amount $\vec{s_{ni}} = \delta\vec{R}_{ni}$, then their total kinetic energy can be expressed as

$$K_{\text{ions}} = \sum_{n,i} \frac{1}{2} M_i \left[\frac{d\vec{s_{ni}}}{dt}\right]^2 = \frac{1}{2} \sum_{n,i,\alpha} M_i \left[\frac{ds_{ni\alpha}}{dt}\right]^2, \tag{2.33}$$

where the subscript α corresponds to the Cartesian directions. On the other hand, the potential energy of the ions can be written as a Taylor expansion

$$V = \frac{1}{2} \sum_{n,i,\alpha,m,j,\beta} \frac{\partial^2 E}{\partial R_{ni\alpha} \partial R_{mj\beta}} s_{ni\alpha} s_{mj\beta}. \tag{2.34}$$

where E is the total energy of the ions. In the expression, third or higher order terms have been neglected (Harmonic Approximation), and the first order term vanishes, since the system is assumed to be in equilibrium when the ions are at postions $\vec{R}_{ni}$.

The so-called force constant matrix $F_{ni\alpha;mj\beta}$ is defined as

$$F_{ni\alpha;mj\beta} = \frac{\partial^2 E}{\partial R_{ni\alpha} R_{mj\beta}}. \tag{2.35}$$

The dimension of this matrix is $\dim(F) = d \times \nu \times N$, where d is the dimension of the space, ν the number of atoms in the basis, and N the number of primitive cells in the system. The equation of motion for the ions in the crystal can then be written as

$$M_i \frac{d^2 s_{ni\alpha}}{dt^2} = -\frac{\partial E}{\partial R_{ni\alpha}} = -\sum_{mj\beta} F_{ni\alpha;mj\beta} s_{mj\beta} \tag{2.36}$$

We then look for solutions of the form $s_{ni\alpha}(t) = \frac{1}{\sqrt{M_i}} \tilde{u}_{ni\alpha} e^{-i\omega t}$, obtaining the eigenvalue equation

$$\omega^2 \tilde{u}_{ni\alpha} = \sum_{mj\beta} \tilde{D}_{ni\alpha;mj\beta} \tilde{u}_{mj\beta} \tag{2.37}$$

where $\tilde{D}_{ni\alpha;mj\beta}$ is the dynamical matrix, defined as

$$\tilde{D}_{ni\alpha;mj\beta} = \frac{1}{\sqrt{M_i M_j}} F_{ni\alpha;mj\beta}. \tag{2.38}$$

Because of translational symmetry $\tilde{D} = \tilde{D}(\vec{R_n} - \vec{R_m})$, we should look for solutions of the form $\tilde{u}_{ni\alpha} = u_{i\alpha} e^{i\vec{q}\cdot R_n}$, which is the same as Fourier transforming Equation 2.38. In this way by defining

$$D_{i\alpha;j\beta} = \sum_{\vec{R}} \tilde{D}_{ni\alpha;mj\beta} e^{-i\vec{q}\cdot\vec{R}}, \tag{2.39}$$

then the eigenvalue equation can be cast as

$$\sum_{j,\beta} D_{i\alpha;j\beta} u_{j\beta} = \omega^2 u_{i\alpha}, \tag{2.40}$$

or, i.e.,

$$\overleftrightarrow{D}\,(\vec{q}) \cdot \vec{u} = \omega^2 \vec{u}. \tag{2.41}$$

The solutions to the eigenvalue equation are labeled by $\vec{q}$'s belonging to the first Brillouin zone and the dimension of $\vec{u}$ is $d \times \nu$. By solving Equation 2.41, we obtain the $d \times \nu$ normal phonon modes and their corresponding frequencies (for N values of $\mathbf{q}$ in the first Brillouin zone).

Within the Finite Difference Method, force constants in Equation 2.35 are approximated as

$$F_{ni\alpha;mj\beta} = -\frac{\Delta E}{s_{ni\alpha} s_{mj\beta}} = -\frac{f_{ni\alpha}}{s_{mj\beta}}. \tag{2.42}$$

where $f_{ni\alpha}$ is the force acting on ion ni in the direction α when ion mj is displaced by a small amount in direction β. Making use of this approximation, the Finite Difference Method within DFT works in the following way: Obtain the equilibrium configuration for the structure with the maximum possible accuracy (i.e. forces of the order of $\approx 10^{-4}$ eV/Å); displace atom j along direction β keeping all the other atoms fixed; calculate $F_{ni\alpha;mj\beta}$ for all the i ions in the unit cell by using Equation 2.42. This last step is usually done in a cell large enough (supercell) to minimize spurious interactions of an atom with its periodic images. Once all the different components of $F_{ni\alpha;mj\beta}$ have been calculated, the dynamical matrix is determined by Equation 2.38. Thus, by diagonalizing this matrix the normal modes of the system can be obtained.

Equation 2.38 can be rewritten in a more explicit form

$$D(\mathbf{q})\mathbf{e}_{\mathbf{q},s} = \omega^2_{\mathbf{q},s}\mathbf{e}_{\mathbf{q},s}, \tag{2.43}$$

where each phonon mode is represented by $\mathbf{q}$, belonging to the first Brillouin zone, and s, the band index, which runs over $d \times \nu$ values. The eigenvector $\mathbf{e}_{\mathbf{q},s}$ is $(d \times \nu)$-dimensional, and its components corresponds to the d Cartesian components of each of the ν ions in the unit cell.

2.0.8 Thermal Properties

2.0.8.1 Constant Volume Heat Capacity

Once we have determined the phonon dispersion for the system, the heat capacity at constant volume can be obtained from quantum statistical mechanics for bosons:

$$C_v = \left.\frac{\partial u}{\partial T}\right|_V = \sum_{\mathbf{q},s} k_B \left[\frac{\hbar\omega(\mathbf{q},s)}{k_B T}\right]^2 \frac{\exp(\hbar\omega(\mathbf{q},s)/k_B T)}{\left[\exp(\hbar\omega(\mathbf{q},s)/k_B T) - 1\right]^2}, \tag{2.44}$$

where $\mathbf{q}$ is a reciprocal lattice vector and $\omega(\mathbf{q},s)$ is the frequency of the corresponding normal mode. As I mentioned in the previous section these frequencies are obtained from DFT calculations combined with the Finite Differences Method.

2.0.8.2 Boltzmann Transport Equation and Thermal Conductivity

According to Fourier's Law, the heat flux ($\vec{q}$) across a material and the temperature gradient are related by:

$$\vec{q} = -\kappa\nabla T, \tag{2.45}$$

where the proportionality constant κ (positive) is defined as the thermal conductivity. Since heat flux can be achieved from both lattice vibrations and transfer of electrons, the thermal conductivity can be expressed as

$$\kappa = \kappa_e + \kappa_{ph}, \tag{2.46}$$

where κ_e and κ_{ph} are the contributions due to electrons and phonons, respectively. The electrical thermal conductivity is related to the eletronic conductivity through the Wiedemann-Franz Law:

$$k_e = L\sigma T, \tag{2.47}$$

where $L = 2.44 \times 10^{-8}$ W Ω K^{-2} is the Lorenz constant. Since for the systems considered here, the electronic contribution to the thermal conductivity is typically smaller than the lattice contribution, I will concentrate on the latter.

First we notice that the total energy per unit time carried by phonons of energy $\hbar\omega(\mathbf{q}, s)$ moving with veloctity $v(\mathbf{q}, s)$ is given by $f_{\mathbf{q}s}\hbar\omega(\mathbf{q}, s)\vec{v}(\mathbf{q}, s)$, where $f_{\mathbf{q}s}$ is non-equilibrium distribution function. The total heat flux in the material is then obtained by summing over all the phonon modes

$$\vec{q} = \hbar \sum_{\mathbf{q},s} f_{\mathbf{q},s}\omega_{\mathbf{q},s}\vec{v}_{\mathbf{q},s} \tag{2.48}$$

For small deviations from equilibrium, the relaxation-time approximation assumes that the rate at which the distribution function $f_{\mathbf{q},s}$ returns to equilibrium is proportional to the deviation:

$$-\vec{v}_{\mathbf{q},s} \cdot \frac{\partial f^0_{\mathbf{q},s}}{\partial T}\nabla T = \frac{f_{\mathbf{q},s} - f^0_{\mathbf{q},s}}{\tau_{\mathbf{q},s}}, \tag{2.49}$$

where $f^0_{\mathbf{q},s}$ corresponds to the equilibrium distribution function (Bose for phonons) and $\tau_{\mathbf{q},s}$ the relaxation time. Since in general the thermal conductivity of a real material is not isotropic, we define a thermal conductivity tensor such that

$$q_\alpha = -\sum_\beta \kappa_{\alpha\beta} \left(\nabla T\right)_\beta . \tag{2.50}$$

By combinig Eq. (2.22), (2.25) and (2.26), the thermal conductivity tensor can be obtained as

$$\kappa_{\alpha\beta} = \hbar \sum_{\mathbf{q},s} v^\alpha_{\mathbf{q},s} v^\beta_{\mathbf{q},s} \tau_{\mathbf{q},s} \omega(\mathbf{q},s) \frac{\partial f^0_{\mathbf{q},s}}{\partial T}, \tag{2.51}$$

where the superscripts α, β correspond to the Cartesian components. In the same way as previously in the case of the constant volume heat capacity, $\omega(\mathbf{q},s)$ can be obtained by using DFT combined with the Finite Differences Method. The phonon group velocities can be calculated from the phonon dispersion by taking into account that

$$v^\alpha_{\mathbf{q},s} = \frac{\partial \omega_{\mathbf{q},s}}{\partial q_\alpha}. \tag{2.52}$$

In the analysis of different properties of a solid, many times one is also interested in determining the relative contributions coming from individual atoms or group of atoms of different substructures. For instance, in the study of the electronic structure, the partial Densitiy of

States (PDOS) gives the projection of the total DOS over the different atoms. Following the same spirit, the Projected Thermal Conductivity for atom μ is defined as

$$\kappa_{\alpha\beta,\mu} = \hbar \sum_{\mathbf{q},s} |\mathbf{e}^{\mu}_{\mathbf{q},s}|^2 v^{\alpha}_{\mathbf{q},s} v^{\beta}_{\mathbf{q},s} \tau_{\mathbf{q},s} \omega(\mathbf{q},s) \frac{\partial f^0_{\mathbf{q},s}}{\partial T}, \tag{2.53}$$

where $\mathbf{e}^{\mu}_{\mathbf{q},s}$ is the subvector determined by the components of the normal mode eigenvector corresponding to atom μ. Since the eigenvectors are orthonormal, it is easy to verify that the total thermal conductivity can be obtained by the sum over all the N individual atoms in the unit cell

$$\kappa_{\alpha\beta} = \sum_{\mu}^{N} \kappa_{\alpha\beta,\mu}. \tag{2.54}$$

CHAPTER 3

FIRST PRINCIPLES STUDIES OF THE MISFIT-LAYERED CALCIUM COBALTITE

3.1 Introduction

Transition metal oxides have been the focus of many experimental, theoretical, and computational studies, as they exhibit a wide range of functional properties including colossal magneto-resistance, two-dimensional electron gas, (multi)-ferroism, and superconductivity, to name a few. It was suggested a while ago that bringing two transition metal oxides with different properties in close proximity with each other might result in the emergence of novel and exciting phases not seen in either bulk structure [24, 25]. For example, one such novel phase stabilized by combining an insulating oxide with a distorted rocksalt structure and a Mott-insulator oxide can exhibit high efficiency thermoelectric transport [26]. Such a combination would not only satisfy the subsystem approach, where one subsystem fulfills the role of the "electron crystal" while the other acts as a "phonon glass", but the interfacial effects can also be expected to lead to a significant enhancement of the electron transport, not seen in pure bulk phases. Incommensurately-layered cobalt oxides [27–31, 10], in particular $Ca_3Co_4O_9$, (CCO), also reported as $(Ca_2CoO_3)(CoO_2)_{1.62}$, represent one such system, where the close proximity between the layers of rocksalt (RS) Ca_2CoO_3 and hexagonal CoO_2 results in a high in-plane Seebeck coefficient, S, and more importantly, a high thermoelectric figure of merit, ZT, at

elevated temperatures. Furthermore, CCO stands out as the only layered cobalt oxide system containing one cation with nominally different oxidation states in both subsystems, namely Co^{2+} in the RS layers and Co^{4+} in the hexagonal CoO_2 layers. This makes CCO an ideal system for studying effects such as charge transfer or orbital ordering both experimentally and theoretically.

Since the pioneering experimental study of Masset *et al.* [32] who reported the structural model of CCO along with its temperature-dependent magnetic and transport properties, there have been several other experimental studies about the structural, electronic, magnetic, and thermoelectric properties of CCO in its pristine [32–48] as well as doped forms with various types of cation substitutions [49–56]. The structure of CCO was reported to be monoclinic with two misfit-layered subsystems, a distorted RS-type Ca_2CoO_3 layer sandwiched between two CdI_2-type CoO_2 layers along the $c-$direction. Both subsystems share the same a and c lattice parameters, but they are incommensurate along the b direction. Among the experimental studies to date, of particular importance is the study by Takeuchi *et al.* [36] who investigated the electronic structure of CCO using high resolution photoemission spectroscopy and demonstrated that the large thermoelectric power of CCO could be well accounted for with the Boltzmann-type metallic electrical conduction. The authors also argued that the metallic conduction in CCO was due to the hexagonal CoO_2 layer, not the RS subsystem. This suggestion was also supported by resistivity and Hall measurements of Eng *et al.* [41] who argued that the transport properties of CCO were essentially governed by itinerant holes in the CoO_2 layers.

In spite of significant experimental effort to characterize and improve its thermoelectric properties, there have been few theoretical or computational studies on CCO [46, 57, 58]. To some extent, this is due to the computational challenge posed by modeling an incommensurate crystal. Asahi *et al.* carried out the first *ab initio* calculations on CCO within the framework of density functional theory (DFT): Using an approximate unit cell of composition $(Ca_2CoO_3)_4(CoO_2)_6$, they performed a comprehensive study of the structural, electronic, magnetic, and thermoelectric properties of CCO [57]. While the computations of Asahi *et al.* provided a great deal of information at the microscopic level to aid in the interpretation of experiments and accounted for some of the experimental observations, their finding that only the RS subsystem contributes to the density of states at the Fermi level was later shown to be in contradiction with the interpretations of Takeuchi *et al.* from their photoemission experiments.

In the present study, I report results from first principles calculations performed within a DFT framework on CCO using structural models with systematically increasing unit cell sizes. As mentioned before, the composition of CCO can be described relatively well as $(Ca_2CoO_3)(CoO_2)_{1.62}$ which means that the composition ratio of the two subsystems is very close to the golden mean $\tau = (1+\sqrt{5})/2 \approx 1.618$, which commonly appears in the study of quasicrystals [59]. Taking into account that τ is the limit of the sequence of the ratios of consecutive Fibonacci numbers $F(n+1)/F(n) = 2, 3/2, 5/3, 8/5, 13/8, ... \to \tau$, I model the incommensurate structure of CCO by using supercells with composition $(Ca_2CoO_3)_{2F(n)}(CoO_2)_{2F(n+1)}$. Using the same terminology as in the study of quasicrystals [59], I call such supercells "rational approximants" to CCO. In this study, I consider four consecutive approximants of increasing

supercell sizes, namely the 3/2, 5/3, 8/5, and 13/8 approximants, the smallest of which is the one considered by Asahi *et al.* For each approximant, I determine the structural and electronic properties using local and gradient-corrected exchange-correlation functionals, as well as using the DFT+U formalism [23, 60] to account for enhanced electron correlations. I show that good agreement with photoemission experiments can be obtained when correlations are taken into account in the RS subsystem, while the size of the approximant plays a secondary role. The rest of the paper is organized as follows. In the next section, I outline the computational methods and parameters used in this study. The results and discussion of my first principles computations for the structural, electronic, magnetic, and thermoelectric properties of various approximants used to model CCO within DFT and DFT+U are presented in Sec. III. I conclude with a brief summary in Sec. IV.

3.2 Computational Methods and Parameters

Monoclinic unit cells of CCO were constructed for the different rational approximants. The lattice parameters were initially set at the experimental values [33] along the periodic directions as $a = 4.83$ Å, $c = 10.84$ Å, and $\beta = 98.13°$. The periodicities of the Ca_2CoO_3 RS and CoO_2 hexagonal subsystems along the b direction are incommensurate with each other. As a result, CCO can be stoichiometrically expressed as $(Ca_2CoO_3)(CoO_2)_{b_1/b_2}$, where b_1 and b_2 correspond to the periodicities of the RS and CoO_2 subsystems along the incommensurate b direction, respectively. The corresponding experimental values are $b_1^{\rm exp} = 4.56$ Å and $b_2^{\rm exp} = 2.82$ Å, yielding $b_1^{\rm exp}/b_2^{\rm exp} \approx 1.62$. In order to build the different rational approximants with composition $(Ca_2CoO_3)_{2F(n)}(CoO_2)_{2F(n+1)}$ I took the initial lattice parameters b of the monoclinic unit cell

along the incommensurate direction by an average, such that $2b = F(n)b_1^{\rm exp} + F(n+1)b_2^{\rm exp}$. This results in starting periodicities of $b_{\rm RS}$ and $b_{\rm CoO_2}$ for the two subsystems, where $2b_{\rm RS} = b_1^{\rm exp} + F(n+1)b_2^{\rm exp}/F(n)$ and $2b_{\rm CoO_2} = b_2^{\rm exp} + F(n)b_1^{\rm exp}/F(n+1)$. In the present study, I considered four rational approximants for CCO, namely the 3/2, 5/3, 8/5, and 13/8 approximants with 42, 66, 108, and 174 atoms in the unit cell, respectively. The initial lattice parameters b along the incommensurate direction for those approximants are 8.79, 13.89, 22.68, and 36.57 Å, respectively. Various views of unit cell for the unrelaxed 5/3 approximant are shown in Figure 6.

The calculations were performed using the projector augmented wave (PAW) method as implemented in VASP [61]. All internal as well as lattice parameters (a, b, c, β) were allowed to relax in the structural optimizations, where I used a plane wave cutoff of 530 eV and a residual force criterion of 0.02 eV/Å. During structural optimizations, I used Monkhorst-Pack (MP) **k**-point grids of $6 \times 3 \times 3$, $6 \times 2 \times 3$, $6 \times 2 \times 3$, and $4 \times 1 \times 2$ for the 3/2, 5/3, 8/5, and 13/8 approximants, respectively. For the density of states calculations, I used the same cutoff energy and the tetrahedron method with MP grids of $12 \times 6 \times 6$, $12 \times 4 \times 6$, $12 \times 2 \times 6$, and $12 \times 2 \times 6$ for the 3/2, 5/3, 8/5, and 13/8 approximants, respectively. The calculations were performed within the local (spin) density approximation (LDA) using the Ceperley Alder (CA) functional [62], as well as with the generalized gradient approximation using the Perdew-Burke-Ernzerhof (PBE) functional [63]. I have carefully examined the dependence of the results on the choice of the exchange-correlation functional, and note that the main conclusions reported in this paper do not have a significant dependence on this choice. Accordingly, unless otherwise noted, all

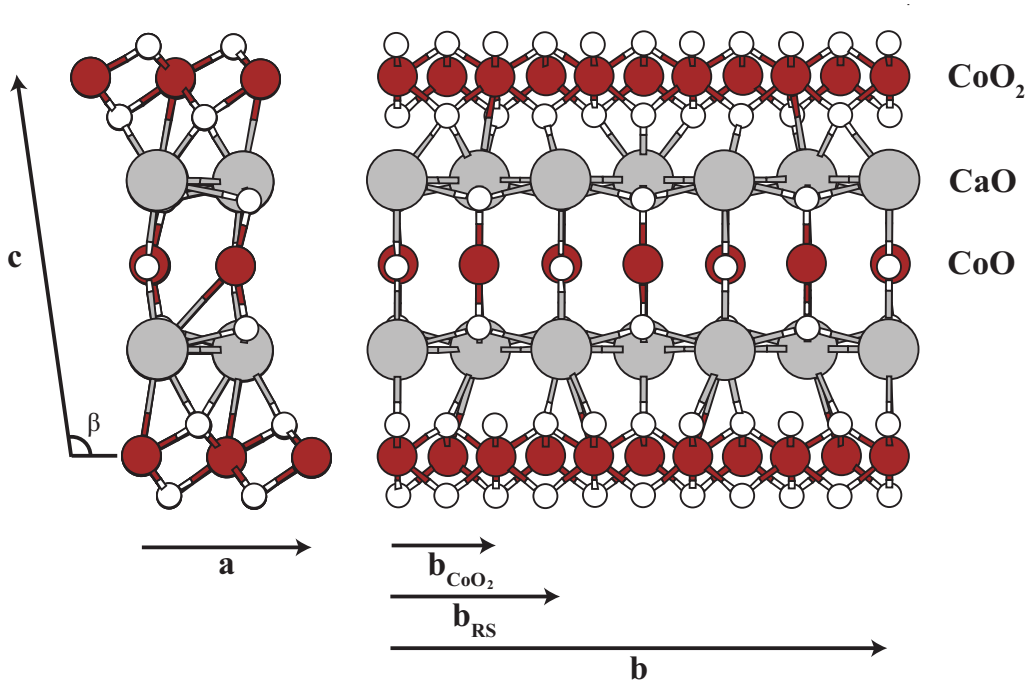

Figure 6. The structure of the unrelaxed 5/3 rational approximant of CCO (one unit cell plus an extra CoO_2 layer) along the b (left) and a (right) directions. The large gray, medium-sized dark (red), and small white circles represent Ca, Co, and O atoms, respectively. The particular atoms in CoO_2 and RS subsystems with fractional coordinates given in Tables II and IV are labeled on the left. The periodicities b_{CoO_2} and b_{RS} of the CoO_2 and RS subsystems are shown on the right.

results for the atomic and electronic structures of CCO are reported for the LDA-CA exchange-correlation functional. The calculations were performed for the ferromagnetic spin configuration of the Co atoms. The initial magnetic moments for all Co atoms were set at 1.3 μ_B. I tested the dependence of the convergence to the correct ground state on the initial magnetic moment by restarting all computations for the 3/2 and 5/3 approximants with different starting moments of 2.0, 1.5, and 1.0 μ_B.

In order to provide a better description of the correlations between the rather localized d electrons of Co, I also performed LDA+U computations for all rational approximants of CCO following Dudarev's approach [64], as implemented in VASP. With $J = 1$ eV, I considered values of 3, 5, and 7 eV for the on-site Coulomb repulsion term U. Values near $U = 5$ eV were suggested and successfully used in previous DFT calculations carried out on Na_xCoO_2 and CoO_2 [65, 66]. In addition, I also computed the effective U parameters for Co atoms in the RS and CoO_2 subsystems from first principles using a linear response approach [67], as implemented in the Quantum Espresso package [68]. The results from these computations will be discussed in the next section.

3.3 Results and Discussion

3.3.1 Structural parameters

Starting with the experimental lattice and internal parameters as described above, full structural optimizations were carried out on all approximants. The results for the relaxed lattice parameters are displayed in Table I. For the a and c lattice parameters, we observe no significant variations as a function of the approximant used. Within LDA, a and c are underestimated by

$\sim 1.5-2\%$ and $\sim 3\%$, respectively. Along the incommensurate direction, on the other hand, the relaxed lattice parameters b_{RS} and $b_{\mathrm{CoO_2}}$ are, by construction, expected to show larger variations with respect to the approximant size. This is indeed what we observe in Table I, where b_{RS} and $b_{\mathrm{CoO_2}}$ converge somewhat slowly to values near 4.5 and 2.8 Å, respectively, which are slightly underestimated with respect to experimental values, consistent with the trends observed within LDA. Repeating the calculations with PBE exchange-correlation functional, I find that the lattice parameters are slightly $(1-2\%)$ overestimated compared to experimental values, as expected. As shown in Table I for the 3/2 approximant, the agreement with experiment is slightly better with the PBE functional compared to LDA, especially for the c lattice parameter.

TABLE I

Experimental and computed (within DFT) lattice parameters for all the rational approximants. The lengths of the lattice parameters are given in Å.

Approximant	a	b_{RS}	$b_{\mathrm{CoO_2}}$	c	β
3/2 (LDA)	4.73	4.29	2.86	10.52	98.13°
3/2 (PBE)	4.89	4.39	2.92	10.92	98.14°
5/3 (LDA)	4.75	4.57	2.74	10.50	98.31°
8/5 (LDA)	4.76	4.47	2.79	10.50	98.25°
13/8 (LDA)	4.76	4.50	2.77	10.48	98.28°
Experimental	4.83	4.56	2.82	10.84	98.13°

Fractional coordinates for the internal parameters computed for all the approximants are shown in Table II along with the experimental values. The agreement with experimental values is quite reasonable (within a few percent), except for the fractional coordinates of Co along the $a-$axis in the RS subsystem and O1 along the $c-$axis in the CoO_2 subsystem where the

TABLE II

Experimental and computed (within DFT) fractional coordinates for all the rational approximants. See Figure 6 for the atom labels. Unless otherwise noted, all results are from computations performed within LDA.

		Experimental		3/2		3/2 (PBE)		5/3		8/5		13/8	
Subsystem	Atom	a	c	a	c	a	c	a	c	a	c	a	c
CoO_2	Co	0.000	0.000	0.000	0.000	0.000	0.000	0.000	0.000	0.000	0.000	0.000	0.000
	O1	0.363	0.084	0.363	0.089	0.364	0.090	0.363	0.093	0.364	0.092	0.363	0.093
	O2	0.636	0.896	0.632	0.907	0.636	0.910	0.637	0.907	0.636	0.908	0.637	0.907
RS	Ca1	0.182	0.281	0.174	0.272	0.179	0.276	0.173	0.278	0.177	0.276	0.176	0.277
	Ca2	0.312	0.727	0.313	0.724	0.317	0.724	0.314	0.722	0.317	0.724	0.316	0.723
	Co	0.702	0.505	0.794	0.498	0.799	0.500	0.799	0.500	0.799	0.500	0.800	0.500
	O1	0.718	0.338	0.689	0.329	0.691	0.333	0.691	0.333	0.694	0.333	0.693	0.333
	O2	0.183	0.497	0.188	0.498	0.203	0.500	0.182	0.500	0.180	0.500	0.179	0.500
	O3	0.837	0.677	0.795	0.666	0.799	0.667	0.799	0.667	0.801	0.667	0.800	0.667

deviations from experiment increase to around 10%. When we repeat the calculations with the PBE exchange-correlation functional, most of the fractional coordinates get closer to experimental values, however, the coordinate of O2 along the $a-$axis in the RS subsystem becomes significantly worse, in agreement with Asahi's earlier results [57]. Overall, the choice of the exchange-correlation functional does not seem to affect the agreement of the computed internal coordinates with experimental values. We also observe that the internal parameters are not very sensitive to the choice of the approximant, with average deviations staying near 3% and 2% along the $a-$ and $c-$axes, respectively, for all approximants considered.

The structures were also fully re-optimized within the DFT+U formalism. The resulting lattice parameters for $U = 5$ eV are displayed in Table III. The inclusion of U does not result in a significant change for a and b lattice parameters or the angle β. However, the c lattice constants increases by $\sim 1\%$ within LDA. The inclusion of U within PBE decreases the lattice constants slightly, and generally results in better agreement with experimental values. The fractional coordinates computed with $U = 5$ eV are shown in Table IV. Overall, the PBE and

LDA results are observed to be rather close to each other for the fractional coordinates. The agreement with experimental values, on the other hand, is not particularly better compared to $U = 0$ case.

TABLE III

Experimental and computed (within DFT+U) lattice parameters for all the rational approximants using $U = 5$ eV. The lengths of the lattice parameters are given in Å.

Approximant	a	b_{RS}	$b_{\mathrm{CoO_2}}$	c	β
3/2 (LDA+U)	4.75	4.24	2.83	10.65	98.20°
3/2 (PBE+U)	4.89	4.36	2.91	10.95	98.20°
5/3 (LDA+U)	4.75	4.58	2.75	10.54	98.34°
8/5 (LDA+U)	4.74	4.46	2.79	10.58	98.28°
13/8 (LDA+U)	4.76	4.50	2.77	10.58	98.28°
Experimental	4.83	4.56	2.82	10.84	98.13°

TABLE IV

Experimental and computed (within DFT+U) fractional coordinates for all the rational approximants using $U = 5$ eV. See Figure 6 for the atom labels. Unless otherwise noted, all results are from computations performed within LDA+U.

		Experimental		3/2		3/2 (PBE+U)		5/3		8/5		13/8	
Subsystem	Atom	a	c	a	c	a	c	a	c	a	c	a	c
CoO_2	Co	0.000	0.000	0.000	0.000	0.000	0.000	0.000	0.000	0.000	0.000	0.000	0.000
	O1	0.363	0.084	0.365	0.093	0.366	0.093	0.364	0.095	0.365	0.094	0.364	0.094
	O2	0.636	0.896	0.635	0.907	0.634	0.907	0.636	0.906	0.635	0.906	0.636	0.906
RS	Ca1	0.182	0.281	0.175	0.268	0.178	0.274	0.174	0.275	0.178	0.273	0.176	0.273
	Ca2	0.312	0.727	0.318	0.732	0.317	0.724	0.316	0.725	0.320	0.727	0.319	0.727
	Co	0.702	0.505	0.797	0.500	0.794	0.500	0.794	0.500	0.799	0.500	0.795	0.500
	O1	0.718	0.338	0.688	0.335	0.687	0.333	0.687	0.335	0.691	0.334	0.691	0.336
	O2	0.183	0.497	0.212	0.500	0.211	0.500	0.206	0.500	0.208	0.500	0.207	0.500
	O3	0.837	0.677	0.793	0.665	0.793	0.667	0.795	0.665	0.798	0.666	0.797	0.665

I note that full optimization of the unit cells (for both $U = 0$ and $U \neq 0$) leads to the emergence of interesting structural patterns along the incommensurate b direction as a function of the approximant size. In particular, the RS unit of composition Ca_2CoO_3 forms various n-unit clusters. Using the notation $X \equiv Ca_2CoO_3$ for the sake of simplicity and denoting an $n-$unit Ca_2CoO_3 cluster by X_n, the arrangement of atoms along the b direction can be viewed as $X_n - X_m - ...$, where each X_n cluster is separated from its neighbors slightly due to the buckling of the O-Co-O chains along the c direction, but still joined with each other along the b direction with Ca-O bonds. As shown in Figure 7, the relaxation leads to the emergence of a $X_3 - X_1$ structural pattern for the 3/2 approximant composed of one 3-unit and one 1-unit clusters along the b direction. The 5/3 approximant can be viewed as two identical 3-unit clusters, $X_3 - X_3$ joined with each other. The 8/5 approximant can similarly be viewed as a $X_3 - X_2 - X_3 - X_2$ pattern fitting within one b lattice parameter. The most complicated pattern occurs for the 13/8 approximation, composed of various $1-$, $2-$, $3-$, and $4-$unit clusters, and is of the form $X_4 - X_2 - X_1 - X_2 - X_4 - X_3$. The particular pattern adopted by a given approximation is related to the incommensurate nature of the CoO_2 and RS subsystems, and depends critically on how the system can minimize the total energy globally within the constraints imposed by the ratio of the Fibonacci numbers. The effects of these structural patterns on the electronic structure of CCO will be discussed toward the end of the next section.

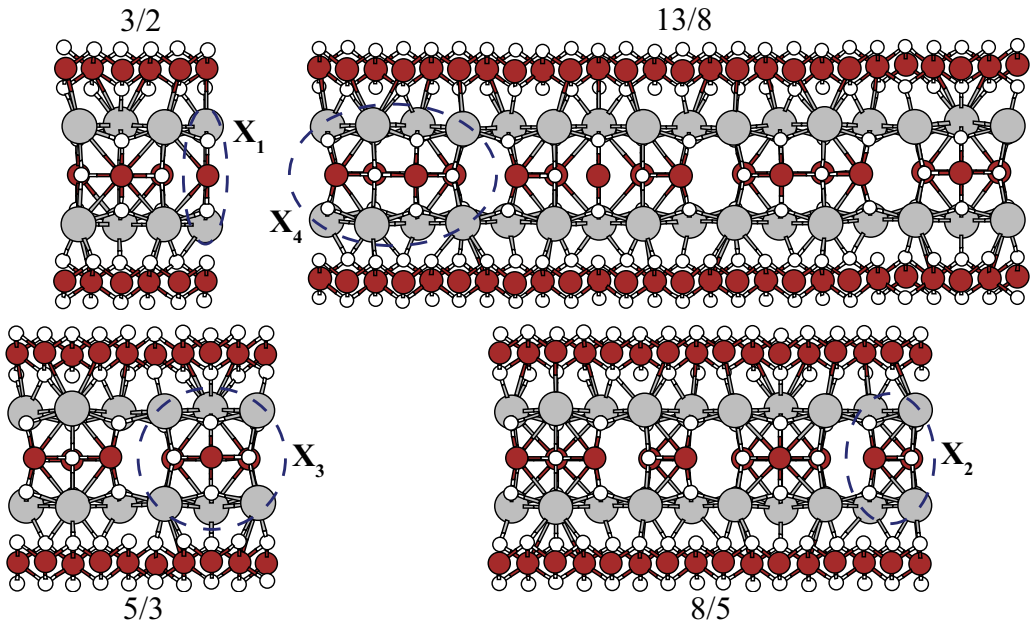

Figure 7. The relaxed structures (with $U = 5$ eV) of all approximants along the a direction. Each structure shows one unit cell plus an extra CoO_2 layer along the c direction. The structural patterns, mentioned in the text, composed of $n-$unit $X \equiv Ca_2CoO_3$ clusters that occur along the b direction are clearly visible. Representatives for $n = 1$, 2, 3, and 4 are shown with dashed ellipses and denoted as X_n.

3.3.2 Electronic Properties

3.3.2.1 Density of States Analysis

In order to gain insight into the transport properties of CCO I focused on the different contributions to the density of states (DOS) around the Fermi level (E_f) from the two subsystems, RS and CoO_2. While I performed the DOS analyses for all the approximants considered, in what follows I will first present our results in detail for the 5/3 approximant and later comment on the trends as a function of the approximant.

Figure 8 shows spin-polarized total DOS for CCO. Low-energy features in the range of -21 to -16 eV correspond to states that originate from the Ca $3p$ and O $2s$ orbitals, and the features at high energies around 8 eV correspond to the unoccupied Ca $3d$ levels. The states from -8 to 3 eV around E_f are due to strong hybridization among O $2p$ and Co $3d$ orbitals. The contributions to the DOS at E_f are primarily from one of the spin channels (down), as E_f falls in a pseudogap in the spin-up channel. There is a (real) gap in the electronic DOS for the spin-down channel in the vicinity of E_f as well, but that occurs ~ 0.2 eV above E_f. Similar features were observed for the total DOS of the 3/2, 8/5 and 13/8 approximants.

Figure 9 shows the site-projected partial DOS (PDOS) for Co $3d$ orbitals in the RS and CoO_2 subsystems; in each plot the PDOS are displayed after averaging over all Co atoms in the particular subsystem. The Co $3d$ states in the CoO_2 subsystem have a small, but finite, contribution to the DOS at E_f only in the spin-down channel, where E_f lies ~ 0.3 eV below the gap. The Co $3d$ states in the RS subsystem, on the other hand, contribute to the DOS at E_f in both spin channels. Comparing Figure 8 and Figure 9, one can see quite well that in

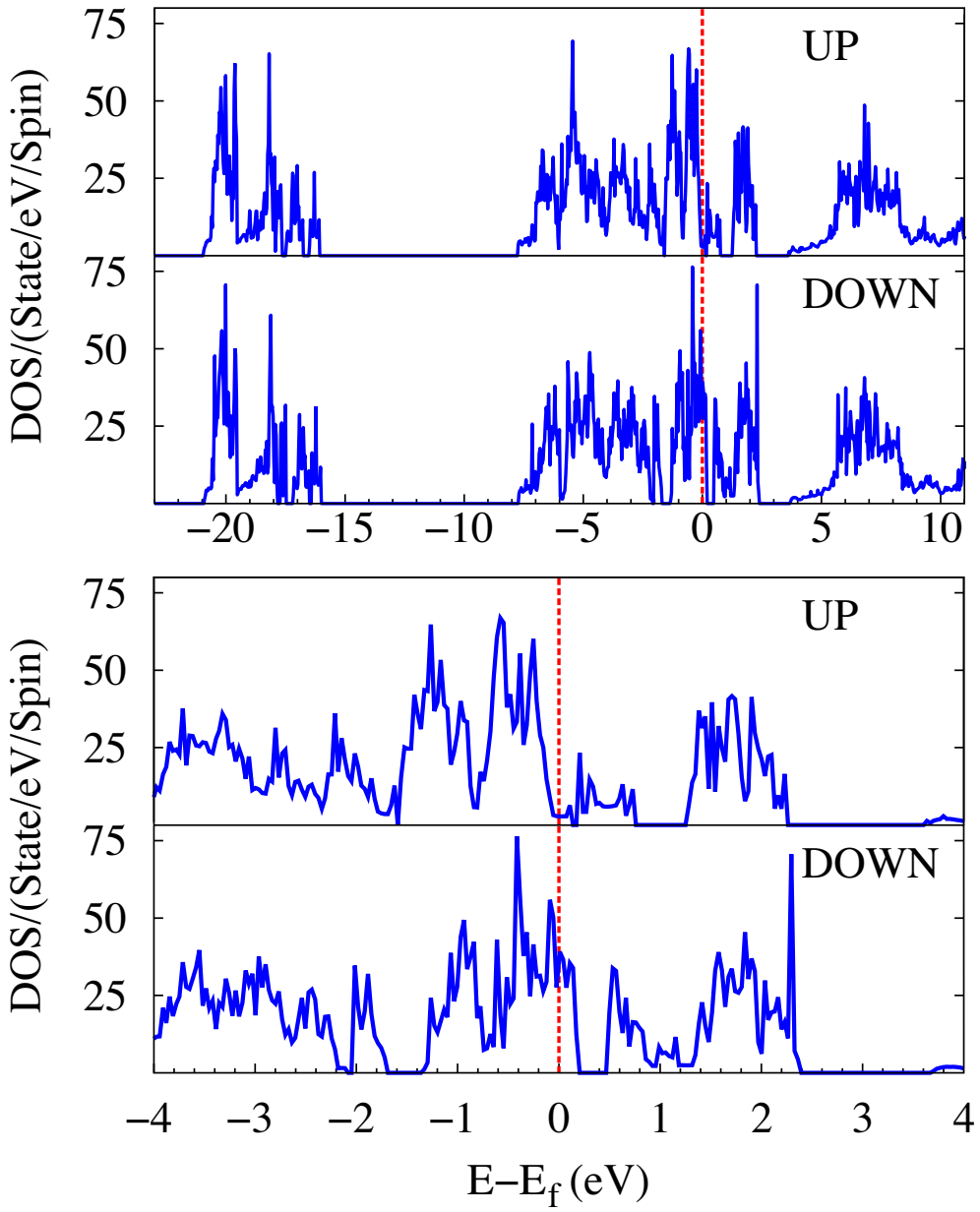

Figure 8. Total DOS (showing spin-up and spin-down channels) computed for the 5/3 rational approximant. The lower panel shows the details of the total DOS within ±4 eV of the Fermi level, which is denoted by the (red) vertical dashed line.

the spin-up channel the DOS in the immediate vicinity of E_f is controlled primarily by states originating from Co $3d$ orbitals in the RS system, while both subsystems contribute to DOS near E_f in the spin-down channel.

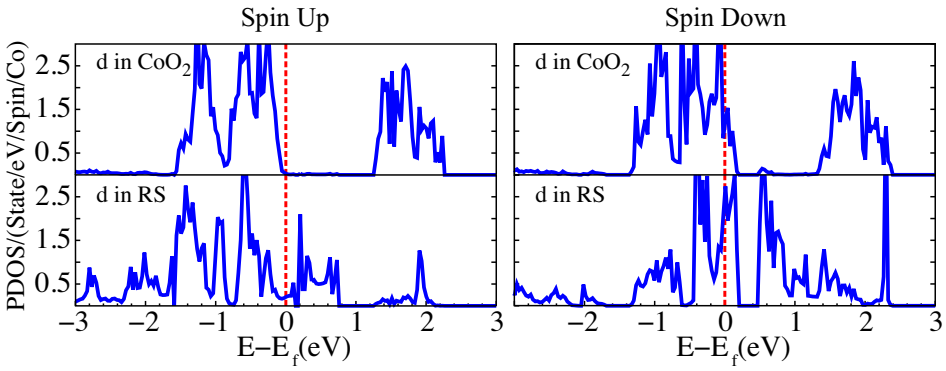

Figure 9. Partial DOS projected into $d-$orbitals of Co atoms in the CoO_2 (upper panels) and the RS (lower panels) subsystems in the spin-up (left) and spin-down (right) channels. The Fermi level is shown with the (red) vertical dashed lines.

The PDOS projections into magnetic angular momentum (m) resolved Co d orbitals in each subsystem are shown in Figure 10 and Figure 11 for the CoO_2 and RS subsystems, respectively. We observe that t_{2g} bands of the CoO_2 system are fully occupied in the spin-up channel. In the spin-down channel, they are mostly, but not fully occupied, contributing to the finite DOS at E_f. The e_g bands of the CoO_2 system, on the other hand, are fully unoccupied lying $\sim$1.2 eV above E_f (Figure 10). In the RS subsystem, all three $t_{2g,\uparrow}$ bands are occupied while the $e_{g,\uparrow}$ bands are partially occupied. In the minority-spin channel, one of the t_{2g} bands, $d_{xy,\downarrow}$,

is noticeably lower in energy and is almost fully occupied, while the other two are partially occupied. The $e_{g,\downarrow}$ bands of the RS system are mostly unoccupied (Figure 11).

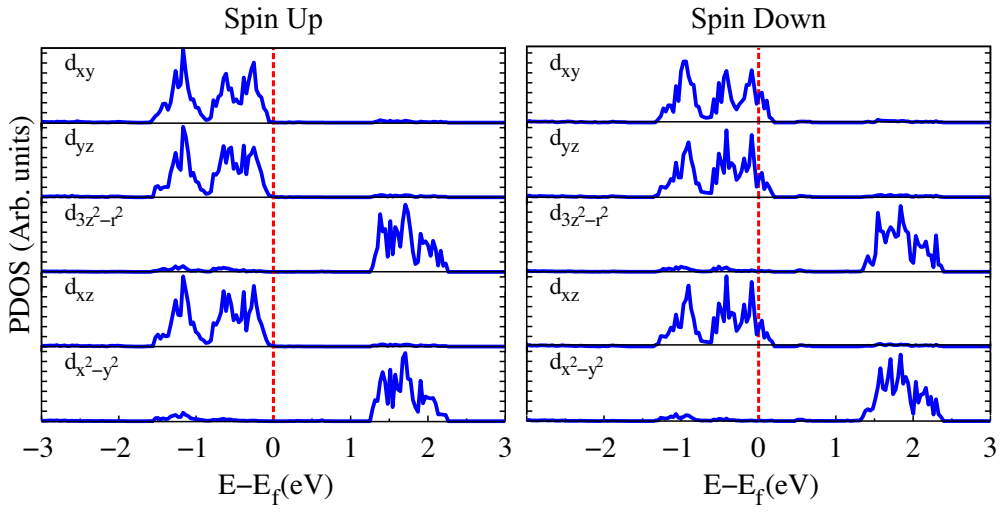

Figure 10. Spin-up (left) and spin-down (right) partial DOS projected into $m-$resolved $d-$orbitals of Co atoms in the CoO_2 subsystem. The Fermi level is shown with the (red) vertical dashed lines.

While there are some differences between our results for the RS subsystem and previous computations of Asahi *et al.*, the differences are mostly minor and the agreement between the two sets of DFT calculations is reasonably good for the RS subsystem. The main difference between our results and those of Asahi *et al.*, which has implications for transport properties of CCO, occurs in the CoO_2 subsystem: Namely, while I find that $3d$ orbitals of the CoO_2 system contribute to the DOS at E_f (Figure 9 upper panel or the spin-down panel of Figure 10), Asahi *et al.* do not find any contribution from this subsystem to the DOS at E_f which falls

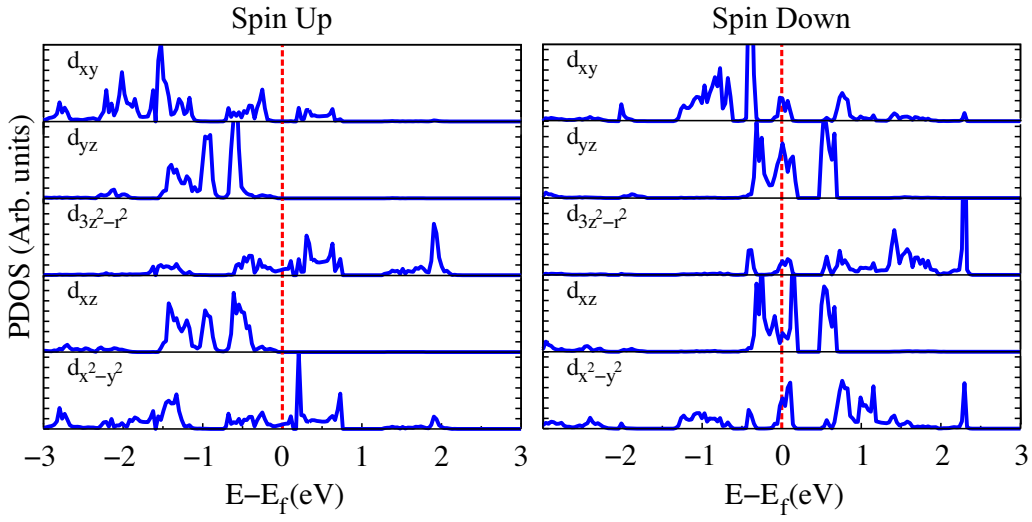

Figure 11. Spin-up (left) and spin-down (right) partial DOS projected into $m-$resolved $d-$orbitals of Co atoms in the RS subsystem. The Fermi level is shown with the (red) vertical dashed lines.

in the crystal-field gap of the CoO_2 $3d$ states setting these Co atoms to be in the low-spin Co^{3+} ($S = 0$) state. In contrast, our results suggest that a fraction of the Co atoms in the CoO_2 subsystem are in the Co^{4+} state due to the partially occupied $t_{2g,\downarrow}$ bands that cross E_f. The finding of no contribution to DOS from the CoO_2 system, therefore, led Asahi *et al.* to conclude that the conductivity of CCO must be due to the RS subsystem while the CoO_2 subsystem would be acting merely as a charge reservoir. This reasonable conclusion is, however, contradicted by resonant photoemission spectroscopy experiments carried out by Takeuchi *et al.* [36] who argued that the valence band in an energy from E_f to 1 eV below it is dominated by the electronic structure of the CoO_2 layer, with very little, if any, contribution from the RS subsystem. My results presented so far are not in good agreement with this experimental observation, either, as we find that both subsystems contribute to the DOS at E_f. In fact,

as shown in Figure 9 and comparisons of Figure 10 and Figure 11, we observe that there is significantly more contribution to the DOS at E_f from the RS subsystem.

3.3.2.2 DOS Analysis within DFT+U

In searching for a possible explanation for this discrepancy, I considered the effect of electron correlations by including the on-site Coulomb interactions in the DFT+U formalism for the Co $3d$ orbitals. While I used a range of U values from 3 to 7 eV and also performed first principles computations of U using a linear response approach for Co atoms in both subsystems, in what follows I will present my results for $U = 5$ eV which is a reasonable value based on previous DFT studies on similar systems [65, 66].

Figure 12 shows the total DOS for both spin channels computed for the 5/3 approximant with $U = 5$ eV. In contrast to the behavior displayed in Figure 8 for $U = 0$, E_f now falls in a gap in the spin-down channel. CCO is still predicted to be a metal, since there is a small, but finite, DOS at E_f in the spin-up channel. As shown Figure 13 which displays the Co $3d$ contributions from the two subsystems, the metallicity of CCO is now almost entirely due to the CoO_2 subsystem with a negligible contribution from the RS subsystem in the spin-up channel. Compared to behavior observed in Figure 9, the inclusion of the Hubbard U, therefore, results in a significant change in the contributions from the RS subsystem to the DOS around E_f, while there is hardly any change in the contributions from the CoO_2 subsystem. Angular momentum resolved projections into various $3d$ orbitals belonging to the CoO_2 and RS subsystems (Figure 14 and Figure 15, respectively) also verify this; the only significant change for the CoO_2 subsystem is that the unoccupied e_g bands now lie ~ 2.3 eV above E_f (Figure 14).

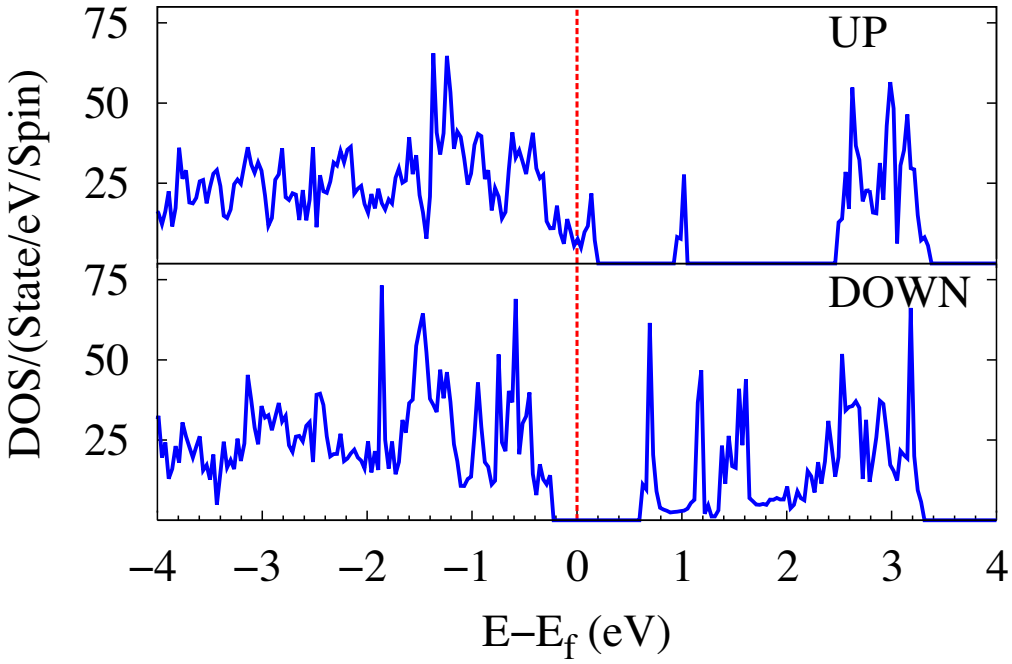

Figure 12. Total DOS (showing spin-up and spin-down channels) computed for the 5/3 rational approximant within LDA+U. The Fermi level is shown by the (red) vertical dashed line. The calculations are performed with $U = 5$ eV.

For the RS subsystem, on the other hand, the e_g bands no longer contribute to the DOS at E_f, as they do for the $U = 0$ case. In addition, the only fully occupied $m-$resolved band in the spin-down channel is $d_{xy,\downarrow}$, and all the other previously ($U = 0$) partially occupied orbitals are now unoccupied (Figure 15). These results show that inclusion of electron correlations beyond the mean-field description of DFT with a Hubbard U leads to agreement with experimental observations about the nature of states near E_f [36, 41].

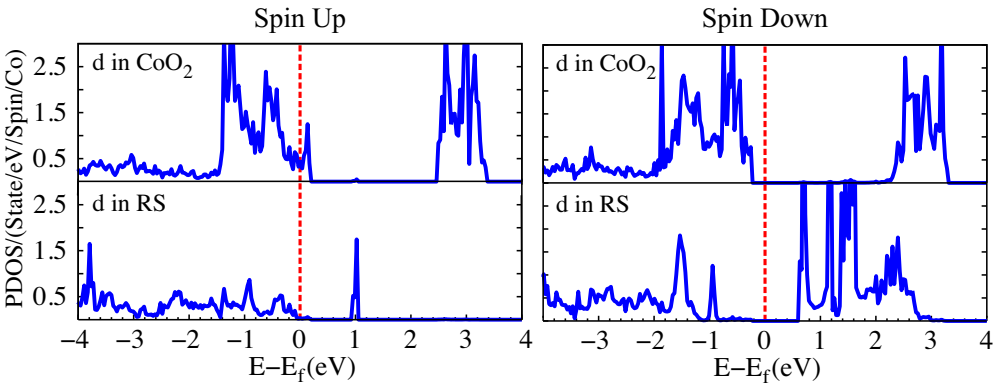

Figure 13. Partial DOS, computed with LDA+U, projected into $d-$orbitals of Co atoms in the CoO_2 (upper panels) and the RS (lower panels) subsystems in the spin-up (left) and spin-down (right) channels. The Fermi level is shown with the (red) vertical dashed lines. The calculations are performed with $U = 5$ eV.

As is well-known, the energy correction introduced by the Hubbard U in the DFT+U method penalizes partial occupation of the localized orbitals, hence, favoring either fully occupied or empty orbitals. In the CoO_2 subsystem, since most of the states are already almost fully

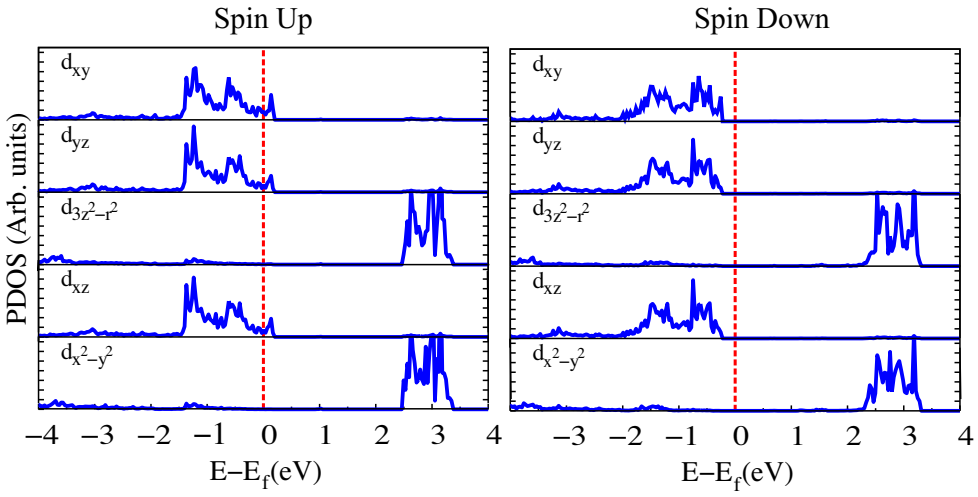

Figure 14. Spin-up (left) and spin-down (right) partial DOS, computed within LDA+U, projected into $m-$resolved $d-$orbitals of Co atoms in the CoO_2 subsystem. The Fermi level is shown with the (red) vertical dashed lines. The calculations are performed with $U = 5$ eV.

occupied (t_{2g}) or empty (e_g), the introduction of the Hubbard term leaves the nature of the states near E_f practically unchanged with the exception of increasing the band gap by $\sim$1 eV. In the case of the RS subsystem on the other hand, several partially occupied states near E_f are split when the Hubbard U is introduced, placing E_f in a gap of Co $3d$ states. It is important to note that this does not mean that the electron correlations are less important in the CoO_2 subsystem. Our first principles computations for the magnitude of U using a linear response theory yield values of 5.4 and 8.1 eV for Co in the RS and CoO_2 sublattices, respectively. However, even such a large U value for the CoO_2 subsystem does not result in a significant change in the behavior of states near E_f, the only change being a slightly larger crystal field splitting between the t_{2g} and e_g states. What controls the position of E_f when U is introduced,

is the energy gain due to the redistribution of the Co $3d$ bands from the RS subsystem to energies fully above and below E_f.

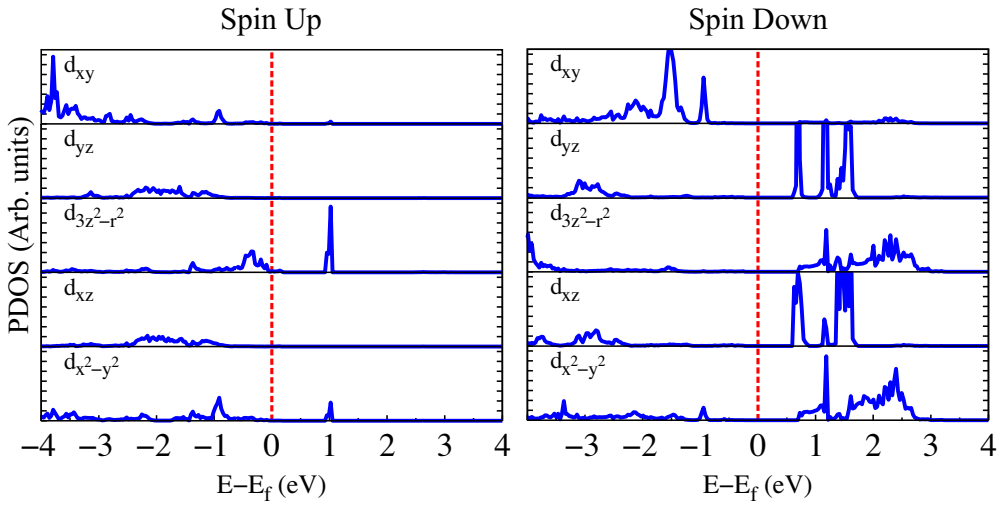

Figure 15. Spin-up (left) and spin-down (right) partial DOS, computed within LDA+U, projected into $m-$resolved $d-$orbitals of Co atoms in the RS subsystem. The Fermi level is shown with the (red) vertical dashed lines. The calculations are performed with $U = 5$ eV.

3.3.2.3 Evolution with respect to Approximant Size

Figure 16 and Figure 17 show how the d projected PDOS around Co atoms in the CoO_2 and RS subsystems, respectively, evolve as a function of the approximant size. The results displayed are for $U = 5$ eV; the general trends as a function of approximant size do not change appreciably for other values of U including $U = 0$. As seen in Figure 16, in the spin-down channel E_f falls in a gap of PDOS projected into the d orbitals of the Co atoms in the CoO_2 subsystem (13/8 approximant is an exception to this, see below), while in the spin-up channel

Co $3d$ states contribute significantly to the DOS at E_f giving rise to the metallic behavior. For projections into Co atoms in the RS subsystem (Figure 17), again E_f lies in a gap of d states in the spin-down channel. In the spin-up channel, on the other hand, the PDOS at E_f remains quite small compared to the contribution from the CoO_2 subsystem, but is not zero. The smallest (almost zero) value of PDOS at E_f is obtained for the 5/3 approximant. For other approximants, the contribution increases in a non-monotonic fashion.

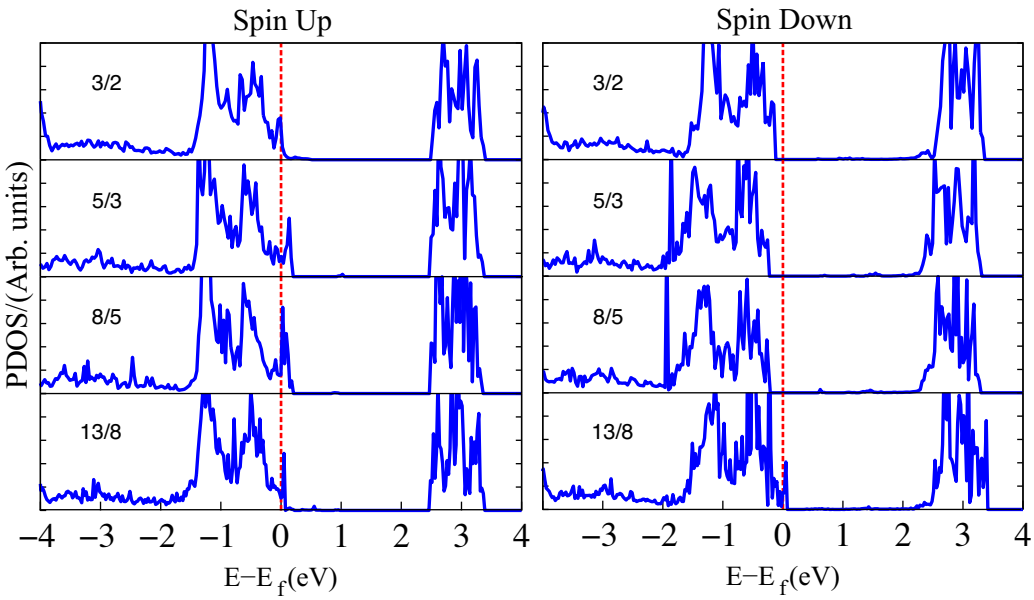

Figure 16. Partial DOS, computed within LDA+U, projected into d-orbitals averaged over all Co atoms in the CoO_2 subsystem for the 3/2, 5/3, 8/5 and 13/8 rational approximants. The Fermi level is shown with the (red) vertical dashed lines. The calculations are performed with $U = 5$ eV.

I have examined the reason behind the slight variations in the contributions to the DOS around E_f, in particular, from the RS subsystem, and find the answer in the details of the arrangements of the (Ca_2CoO_3) RS structure into particular $n-$unit clusters, as discussed at the

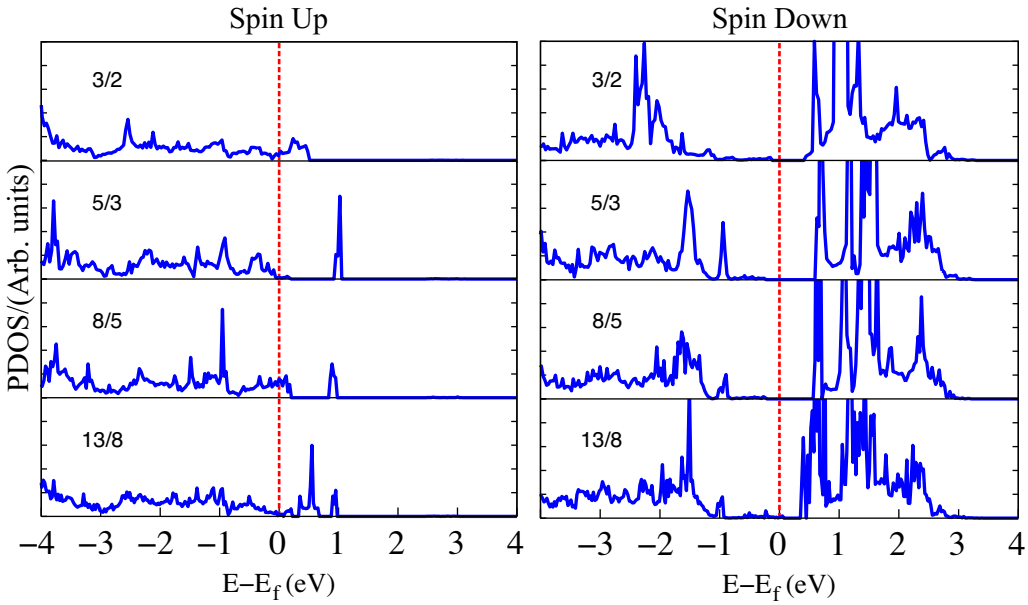

Figure 17. Partial DOS, computed within LDA+U, projected into d-orbitals averaged over all Co atoms in the RS subsystem for the 3/2, 5/3, 8/5 and 13/8 rational approximants. The Fermi level is shown with the (red) vertical dashed lines. The calculations are performed with $U = 5$ eV.

end of the last section. As might be inferred from the middle panel of the spin-up channel PDOS displayed in Figure 15, the relevant orbital that gives rise to small contributions to DOS from the RS subsystem around E_f is $d_{3z^2-r^2}$. For the 5/3 approximation with an almost vanishing contribution to the DOS at E_f from the RS subsystem, there are two identical $(Ca_2CoO_3)_3$ clusters stacked along the b direction. Within each $(Ca_2CoO_3)_3$ cluster, two of the three Co atoms are symmetry-equivalent resulting in 2 distinct Co atoms. Of these two Co atoms, the Co-O interatomic distances for the rather distorted CoO_6 octahedra are such that when electron correlations are taken into account with a Hubbard U, for one of them the $d_{3z^2-r^2,\uparrow}$ orbital is fully occupied, while for the other, it is fully unoccupied and gives rise to the sharp peak observed ~ 1 eV above E_f. The formation of such fully occupied or unoccupied $e_{g,\uparrow}$ orbitals results in practically no contribution to the PDOS from the RS subsystem. However, any time

the RS subsystem contains other types of clusters (such as the 1-, 2-, and 4-unit clusters) found in all other approximants, we observe that the Co atoms from such units contribute slightly to the DOS at E_f, as they are no longer able to accommodate the necessary number of electrons fully below E_f by neatly pairing up with other Co atoms in the relevant cluster, as they can do with a $(Ca_2CoO_3)_3$ cluster. Hence, we find that the (small) contributions to the DOS at E_f from the RS subsystem are correlated with the presence of $1-$, $2-$, and $4-$unit clusters in them. The 13/8 approximant which contains the largest number of such clusters within one unit cell has, accordingly, a relatively large number of RS-derived e_g-like states in the vicinity of E_f. This analysis, along with the interpretations from the photoemission[36] and transport[41] experiments suggests that increasing the unit cell size along the incommensurate direction by going to larger and larger approximants may not necessarily lead to better models for CCO, and the "magic" 5/3 approximant does a good job for modeling the electronic properties of CCO, when correlations are taken into account.

3.3.3 Magnetic Properties

As mentioned earlier, my calculations were performed starting from a ferromagnetic initial configuration for all Co atoms in the structure. Since it is very common for these types of spin-polarized calculations to get trapped in local minima, especially when carried out within the DFT+U framework, I tested different initial magnetizations of 1.0, 1.3, 1.5, and 2 μ_B, in order to check the convergence to the correct ground state. Table V shows the final magnetic moments averaged over Co atoms in the RS and CoO_2 subsystems, in addition to the total magnetization per Co atom (M_{ave}) computed with different exchange-correlation functionals,

$U = 0$ and 5 eV, for all rational approximants considered. The magnetization primarily arises from Co atoms in the RS subsystem; the average magnetic moment in the CoO_2 subsystem is at least one order of magnitude smaller than that in the RS subsystem. The value of M_{ave} increases when the calculations are performed within the DFT+U framework compared to the corresponding regular DFT calculation. Furthermore, M_{ave} computed with PBE is always larger than that computed with the LDA exchange-correlation functional for both $U = 0$ and 5 eV, however, the difference between PBE+U and LDA+U values for M_{ave} is considerably less compared to that between the PBE and LDA values. This is the same observation I reported earlier for the structural parameters, in particular, for the predicted fractional coordinates. If

TABLE V

Averaged magnetic moments (in μ_B) for Co atoms belonging to the RS and CoO_2 subsystems and averaged magnetic moment per cell per Co (M_{ave}) for the different approximants, performed within standard DFT and DFT+U, with LDA and PBE exchange-correlation functionals. The value of the Hubbard parameter is $U = 5$ eV.

Approximant	Ex-corr	RS	CoO_2	M_{ave}
3/2	LDA	1.66	-0.11	0.78
	LDA+U	2.76	-0.03	1.34
3/2	PBE	2.26	0.18	1.26
	PBE+U	2.94	0.10	1.49
5/3	LDA	1.50	0.22	0.88
	LDA+U	2.75	-0.13	1.19
5/3	PBE	2.08	0.12	1.07
	PBE+U	2.86	-0.16	1.19
8/5	LDA	1.53	0.19	0.89
	LDA+U	2.77	-0.10	1.24
13/8	LDA	1.48	0.20	0.87
	LDA+U	2.71	0.00	1.29

we consider the trends as a function of the approximant size, we observe that the convergence is fairly fast, *e.g.* at the LDA level, the M_{ave} values for the 3/2, 5/3, 8/5, and 13/8 rational approximants are 0.78, 0.88, 0.89, and 0.87 μ_B, respectively. The computed M_{ave} that seems to have converged to a value near 0.88 μ_B is underestimated compared to the experimentally measured value near 1.3 μ_B for temperatures of less than 400 K [32]. Within LDA+U, on the other hand, the computed M_{ave} (for $U = 5$ eV) are 1.34, 1.19, 1.24, and 1.29 μ_B, respectively, converging to a value near 1.3 μ_B, in excellent agreement with the experimentally reported value. These results show that the inclusion of electron correlations within DFT+U improves the agreement with experiment regarding not only the contribution of the two subsystems to the DOS near E_f but also the computed magnetic moments as well.

3.3.4 Seebeck Coefficient of CCO

The results from the DOS analysis presented above can be used to obtain an estimate for the Seebeck coefficient (thermopower) S of CCO within the framework of Heikes formula: [69]

$$S = -\frac{k_B}{e} \ln\left(\frac{g_3}{g_4}\frac{x}{1-x}\right), \tag{3.1}$$

where x is the concentration of Co^{4+} ions, and g_3 and g_4 the degeneracies (including both spin and orbital degrees of freedom) for the Co^{3+} and Co^{4+}, respectively. Based on my results for the 5/3 approximant with $U = 5$ eV, I assume that S is determined solely by the contribution from the CoO_2 subsystem. As inferred from Figure 14, the Co atoms in the CoO_2 subsystem are in a low-spin (LS) configuration, and in a mixed-valence state of Co^{3+} ($t^3_{2g,\uparrow}e^0_{g,\uparrow}$) and Co^{4+}

($t^2_{2g,\uparrow}e^0_{g,\uparrow}$). We determine the concentration x from ratio of unoccupied $t_{2g,\uparrow}$ PDOS to the whole area under the $t_{2g,\uparrow}$ PDOS curve from $\sim$ -1.5 eV to $\sim$ 0.2 eV, averaging over the three orbitals. We find a value near 0.3. Setting the degeneracies for the LS configurations of Co^{3+} and Co^{4+} as $g_3 = 1$ and $g_4 = 6$, we thus arrive at a value for $S \sim 227$ μVK^{-1}.

My computed value for S is significantly larger than the value of 41 μVK^{-1} obtained by Asahi *et al.* [57] in their analysis of CCO using the 3/2 approximant. The reason for the large discrepancy can readily be attributed to the differences in the electronic structures of CCO as obtained in the respective first principles studies. In particular, Asahi *et al.* assume no contribution to the Seebeck coefficient from the CoO_2 subsystem, as E_f falls in crystal-field gap of Co d states in the CoO_2 subsystem, and the contribution from the RS subsystem is computed using x, g_3, and g_4 as inferred from their ($U = 0$) calculation. As mentioned before, these findings of Asahi *et al.* are not in agreement with results from the photoemission experiments of Takeuchi *et al.* This observation led us to consider electron correlations within a DFT+U framework that indeed led to the finding of a vanishing DOS at E_f from the RS subsystem. Even with this improvement, the agreement of our computed value for $S \sim 227$ μVK^{-1} with the experimental values near 135 μVK^{-1} (Refs. [32, 37, 48]) is only somewhat fair. However, one should take into account the fact that S has a rather sensitive dependence on x. For example, a value of $x = 0.56$ would result in perfect agreement with experiment. The concentration of Co^{4+} ions was indeed inferred to be $x \sim 0.5$ in recent electron energy-loss spectroscopy studies of Yang *et al.*[43], who reported an average Co valence of 3.5 in the CoO_2 subsystem. One should also keep in mind that the computations are based on the pristine

5/3 approximant model of CCO, and defects and unintentional doping in real materials could change the measured Seebeck coefficient significantly. Finally, I note that my value of $x \sim 0.3$, while not leading to very good agreement with experiment for the values of S as described above, is rather consistent with the amount of doping (interpreted as Co^{4+} content) obtained from transport measurements of Limelette *et al.* [38] and Eng *et al.* [41] who find values near 0.32 and 0.36, respectively. In future studies, it would be instructive to use the computed band structure directly within Boltzmann transport formalism [70] in order to obtain an independent estimate of the Seebeck coefficient.

3.4 Summary

I have reported results on and analyses of first principles calculations, performed within the framework of standard DFT and DFT+U, for misfit-layered CCO modeled by rational approximants with systematically increasing unit cell sizes. The structural parameters computed within DFT and DFT+U are found to be in reasonably good agreement with experimental values and previous computations. The standard DFT calculations predict a large contribution to the DOS at E_f from the RS subsystem, in disagreement with results from photoemission experiments. When electron correlations are taken into account within a DFT+U formalism, d states derived from Co atoms in the RS subsystem are observed to have very little, if any, contribution to DOS at E_f, and the states that give rise to the metallic conductivity of CCO are essentially all derived from Co atoms in the hexagonal CoO_2 subsystem, in agreement with results from photoemission data. It is interesting to note that even though my first principles linear response calculations for the Hubbard U indicate a value for Co atoms belonging to the

CoO_2 subsystem (8.1 eV) that is significantly larger than that for Co atoms in the RS subsystem (5.4 eV), the introduction of U does not result in a significant change in the nature of states derived from the Co atoms in the CoO_2 subsystem, since the relevant t_{2g} states associated with the CoO_2 subsystem are nearly fully occupied and the e_g states fully unoccupied. The impact of U on the RS subsystem, on the other hand, is significant as it opens up a gap in the partial DOS at E_f. My results, therefore, strongly suggest that the necessary ingredient for obtaining agreement with photoemission experiments is to take the correlations into account in the RS subsystem. The size of the rational approximant as a structural model for the incommensurate CCO plays a minor role in this regard. In particular, even a relatively small 5/3 approximant does a good job in modeling the essential electronic properties of CCO. I have presented results that associate the opening of the gap in the PDOS of Co atoms belonging to the RS subsystem with the formation of particular structural features in the form of $(Ca_2CoO_3)_n$ clusters that extend along the incommensurate $b-$direction. I have also shown that another significant effect of U is to bring the computed magnetic moments per Co atom in nearly perfect agreement with experimental values and to minimize the differences between the predictions of LDA+U and PBE+U. Based on my DOS analysis, I find the Co atoms that contribute to the metallic conductivity in CCO (i.e. those in the CoO_2 subsystem) to be in a mixture of Co^{3+} and Co^{4+} low-spin configurations, with a predicted concentration near 30% for Co^{4+} ions. While this value is in very good agreement with results from transport measurements, the predicted Seebeck coefficient S using this concentration of Co^{4+} ions and Heikes formula has only a fair agreement with experimentally measured values for S. I expect that further refinements of the

structural models for CCO, more sophisticated approaches for treating electron correlations, and incorporating energetically favorable point and extended defects in modeling studies will likely lead to the successful resolution of the slight discrepancies remaining between experiment and theory for this technologically and scientifically important oxide thermoelectric material.

CHAPTER 4

LATTICE AND TRANSPORT PROPERTIES OF THE MISFIT-LAYERED OXIDE THERMOELECTRIC $Ca_3Co_4O_9$ FROM FIRST PRINCIPLES

4.1 Introduction

As I mentioned in the introduction, the thermoelectric properties of CCO are intimately related to the co-existence of three conditions: a high Seebeck coefficient, a high electrical conductivity and a low thermal conductivity. The previous chapter was mainly related to electronic properties. Although I have not performed a first principles calculation of the electrical conductivity, by determining the electronic structure of CCO I showed that it is the the CoO_2 subsystem that controls the electrical conductivity of this material. Furthermore, by using my first principles results I was able to give an estimate for the Seebeck coefficient, resulting in a value of the order of experimentally measured values. Thus, having determined the electronic structure from first principles (DFT+U), and having shown that the results are in good agreement with experiments, I can now apply these tools in order to calculate the thermal conductivity.

The main goal in this chapter is to see how I can make use of the data obtained from DFT+U in order to determine vibrational and thermal properties of CCO. First, by using the interatomic forces calculated from first principles and the finite differences method I determine

the full phonon dispersion of the 3/2 and 5/3 approximants. These phonon modes are then used to calculate the specific heat of each structure and compared to experiment. Then I apply the Boltzmann Transport Equation (BTE) to calculate the thermal conductivity for each approximant along the different axes.

4.2 Computational Methods

Similar to the approach discussed in the previous Chapter, monoclinic unit cells of CCO were constructed for the different rational approximants. The lattice parameters were initially set at the experimental values [33] along the periodic directions as $a = 4.83$ Å, $c = 10.84$ Å, and $\beta = 98.13°$. Due to computational constraints, for the phonon studies I only considered the two lowest order rational approximants for CCO, namely the 3/2 and 5/3 approximants, with 42 and 66 atoms in the unit cell, respectively. The initial lattice parameters b along the incommensurate direction for these approximants are 8.79 and 13.89 Å, respectively.

The calculations were performed using the projector augmented wave (PAW) method as implemented in VASP [61], and within the generalized gradient approximation using the Perdew-Burke-Ernzerhof (PBE) functional [63]. All internal as well as lattice parameters (a, b, c, β) were allowed to relax in the structural optimizations, where I used a plane wave cutoff of 550 eV and a residual force criterion of 0.001 eV/Å. During structural optimizations, I used Monkhorst-Pack (MP) **k**-point grids of $4 \times 2 \times 2$ for the two approximants. The two approximants (3/2 and 5/3) were optimized starting from different initial configurations in order to find the most stable structure in each case. Small displacements were added to the initial structures and relaxations were perfomed with and without symmetry. The calculations were performed for the ferromag-

netic spin configuration of the Co atoms. The initial magnetic moments for all Co atoms were set at 1.3 μ_B. I tested the dependence of the convergence to the correct ground state on the initial magnetic moment by restarting all computations for the 3/2 and 5/3 approximants with different starting moments of 2.0, 1.5, and 1.0 μ_B.

As I showed in the previous chapter, a Hubbard U correction has to be included along with GGA in order to provide a better description of the correlations between the rather localized d electrons of Co. In all cases, I used the Dudarev's approach [64], as implemented in VASP. As discussed in Chapter 3, I chose a value of $U = 5$ eV ($J = 1$ eV), since it predicted an electronic structure for CCO in good agreement with experiment. In order to evaluate the effect of the U parameter on lattice and thermal properties, calculations without including U were also performed for the 3/2 approximant.

Lattice-dynamical calculations such as the phonon spectrum and the phonon density of states, were calculated by the Finite Differences Method as implemented in Phonopy [71] using the force constants obtained from DFT calculations. For both the 3/2 and 5/3 approximants, $2\times1\times1$ supercells were employed in the calculation of force constants. As explained in Chapter 2, the constant volume heat capacitu can be calculated from the computed phonon dispersions $\omega(\mathbf{q}, s)$ as

$$C_v = \sum_{\mathbf{q},s} k_B \left[\frac{\hbar\omega(\mathbf{q},s)}{k_B T}\right]^2 \frac{exp(\hbar\omega(\mathbf{q},s)/k_B T)}{\left[exp(\hbar\omega(\mathbf{q},s)/k_B T) - 1\right]^2}, \tag{4.1}$$

where $\mathbf{q}$ is a reciprocal lattice vector in the first Brillouin zone and $\omega(\mathbf{q}, s)$ is the frequency of the corresponding normal mode s. By applying the Boltzmann Transport Equation (BTE)

within the relaxation time approximation, I can also calculate the thermal conductivity tensor (see Chapter 1, Section 2.0.7.2)

$$\kappa_{\alpha\beta} = \hbar \sum_{\mathbf{q},s} v^{\alpha}_{\mathbf{q},s} v^{\beta}_{\mathbf{q},s} \tau_{\mathbf{q},s} \omega(\mathbf{q},s) \frac{\partial f^0_{\mathbf{q},s}}{\partial T}, \tag{4.2}$$

where $v^{\alpha}_{\mathbf{q},s}$ is the phonon velocity, α and β the Cartesian directions, $\tau_{\mathbf{q},s}$ the relaxation time, and $f^0_{\mathbf{q},s}$ the Bose-Einstein distribution function. For simple systems such as Si or Ge, it is possible to compute the relaxation times from first principles [72, 73], however, in the case of CCO, with a very large unit cell, such calculations are prohibitively demanding. Therefore the relaxation time was assumed to be constant, $\tau_{\mathbf{q},s} = \tau$, and taken out of the sum as an adjustable parameter. The phonon velocities were calculated by using the central difference method for frequencies obtained over a dense grid in the Brillouin zone. Since I am also interested in determining the relative contributions to the thermal conductivity coming from the CoO_2 and RS subsystems, I define a projected thermal conductivity as

$$\kappa_{\alpha\beta,\mu} = \hbar \sum_{\mathbf{q},s} |\mathbf{e}^{\mu}_{\mathbf{q},s}|^2 v^{\alpha}_{\mathbf{q},s} v^{\beta}_{\mathbf{q},s} \tau_{\mathbf{q},s} \omega(\mathbf{q},s) \frac{\partial f^0_{\mathbf{q},s}}{\partial T}, \tag{4.3}$$

where $\mathbf{e}^{\mu}_{\mathbf{q},s}$ is the subvector determined by the components of the normal mode eigenvector corresponding to atom μ (see last part of Section 2.0.7.2). In the same fashion as the Projected Density of States (PDOS) for the electronic structure, this quantity represents the individual contribution of individual atoms to the total thermal conductivity, and satisfies

$$\kappa_{\alpha\beta} = \sum_{\mu=1}^{N} \kappa_{\alpha\beta,\mu}, \tag{4.4}$$

where N is the total number of atoms in the unit cell.

4.3 Results

4.3.1 Structure

The resulting lattice parameters for the two approximants are displayed in Table I. For the 3/2 approximant I also display the optimized lattice parameters for the case of pure PBE with no Hubbard correction. Lattice and internal parameters as well as magnetic moments are in good agreement with my previous DFT+U (LDA, PBE) calculations [74] and with experimental results. As discussed in [74] we observe the formation of different clustering patterns along the incommensurate direction, **b**, for the different approximant. Using the notation $X \equiv Ca_2CoO_3$ for the sake of simplicity and denoting an $n-$unit Ca_2CoO_3 cluster by X_n, the arrangement of atoms along the b direction can be viewed as $X_n - X_m - ...$, where each X_n cluster is separated from its neighbors slightly due to the buckling of the O-Co-O chains along the c direction, but still joined with each other along the b direction with Ca-O bonds. As shown in Figure 18, the relaxation leads to the emergence of a $X_2 - X_2$ structural pattern for the 3/2 approximant composed of two 2-units. The 5/3 approximant can be viewed as two identical 3-unit clusters, $X_3 - X_3$ joined with each other. As I have mentioned before, the particular pattern adopted by a given approximation is related to the incommensurate nature of the CoO_2 and RS subsystems, and depends critically on how the system can minimize the total energy

globally within the constraints imposed by the ratio of the Fibonacci numbers. I should also mention that in our previous work, for the 3/2 approximant I found $X_1 - X_3$ clustering patterns instead of the $X_2 - X_2$ shown here. The disagreement is due to the fact that the two clustering patterns are very close in energy and therefore small variations in the starting parameters can lead to different ground state configurations. In the present chapter, since more accurate forces are required in the calculation of phonons, more stringent parameters were used than in the previous case.

TABLE VI

Experimental and computed lattice parameters for the 3/2 (DFT and DFT+U) and 5/3 (DFT+U) rational approximants. The lengths of the lattice parameters are given in Å.

Approximant	a	b_{RS}	$b_{\mathrm{CoO_2}}$	c	β
3/2 (PBE)	4.89	4.39	2.93	10.93	98.10°
3/2 (PBE+U)	4.88	4.41	2.94	10.97	98.05°
5/3 (PBE+U)	4.88	4.71	2.82	10.86	98.22°
Exp.	4.83	4.56	2.82	10.84	98.13°

4.3.2 Vibrational Spectrum and Heat Capacity

The thermoelectric capabilities of CCO for technological applications, in particular for the developement of new energy conversion devices, are intimately related to its vibrational properties. Lattice vibrations are a key contribution to the total thermal conductivity. As such, they could potentially be modified via doping or lattice distorsions in order to enhance or tune the performance of the thermoelectric. Figure 19 shows the phonon dispersions for the two approximants ($U = 5$ eV) along different symmetry directions. Differences in lengths for YΓ

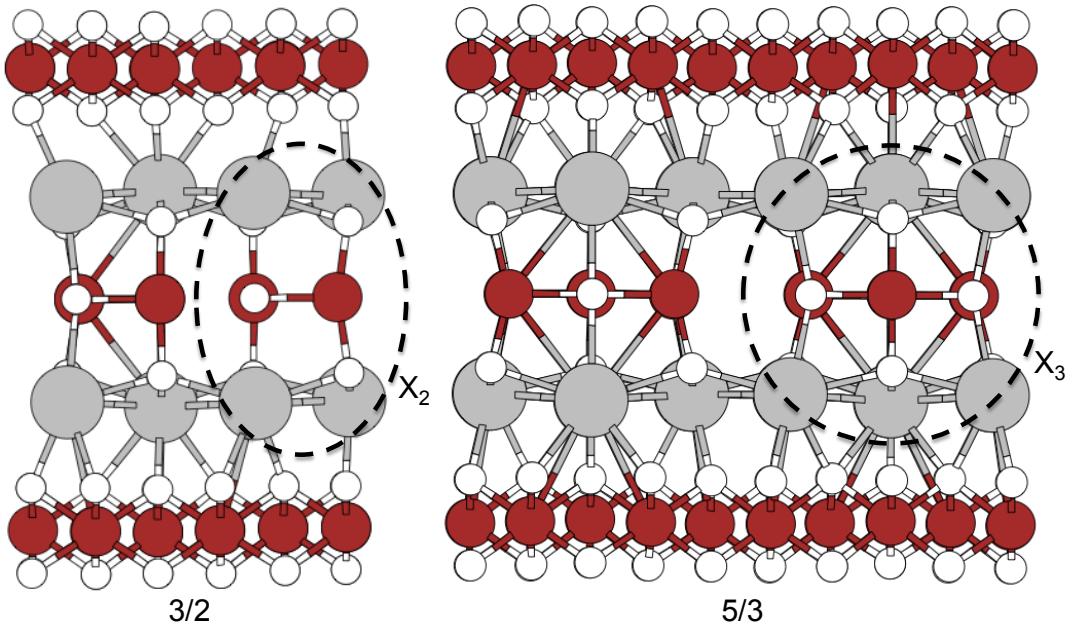

Figure 18. The relaxed structures (with $U = 5$ eV) of the 3/2 and 5/3 approximants along the a direction. Each structure shows one unit cell plus an extra CoO_2 layer along the c direction. The structural patterns, mentioned in the text, composed of $n-$unit $X \equiv Ca_2CoO_3$ clusters that occur along the b direction are clearly visible. Two different clusters, X_2 and X_3 (for the 3/2 and 5/3 approximants, respectively), are show with dashed ellipses.

paths correspond to the different sizes of the b lattice constant for the two approximants. Also, phonons on the 3/2 approximant were calculated by using an optimized $2 \times 1 \times 1$ (84 atoms) unit cell, which accounts for the shorter length for ΓX and the higher density of bands for the 3/2 with respect to the 5/3 (66 atoms in unit cell). Figure 20 shows the calculated phonon DOS for the 3/2 ($U = 0$, $U = 5$ eV) and 5/3 approximants, where negative values correspond to imaginary frequencies. First we notice that in all cases the overall structure of the phonon DOS can be divided in two bell shaped structures, centered at ≈ 6 and 14 THz, respectively. As expected, the lower frequency bell corresponds to normal vibrational modes involving the heavier atoms, Ca and Co, while the higher frequency modes correspond to vibrations of the lighter O atoms. Comparing the DFT and DFT+U case (only for the 3/2 approximant), I observe that apart from eliminating the imaginary values, the inclusion of a finite U does not change the $U = 0$ results significantly. Although different optimizations and modulations of the 3/2 structure were attempted in this latter case, it was not possible to eliminate the imaginary values of the frequency. These instabilities are mostly associated with atoms in the RS subsystem, which has a very large contribution to the DOS at FL when modeled within DFT only (see Figure 9) [75]. On the other hand, when the U is included, and thus the system becomes more insulating, I obtain positive frequencies for the two approximants (3/2 and 5/3). The major differences between the 3/2 and 5/3 cases correspond to the height of the bell centered at ≈ 14 THz, which is significantly higher for the 3/2 approximant.

These differences can be attributed to the different clustering patterns we observe in each case. Having determined the phonon spectrum we can now apply Equation 4.1 in order to

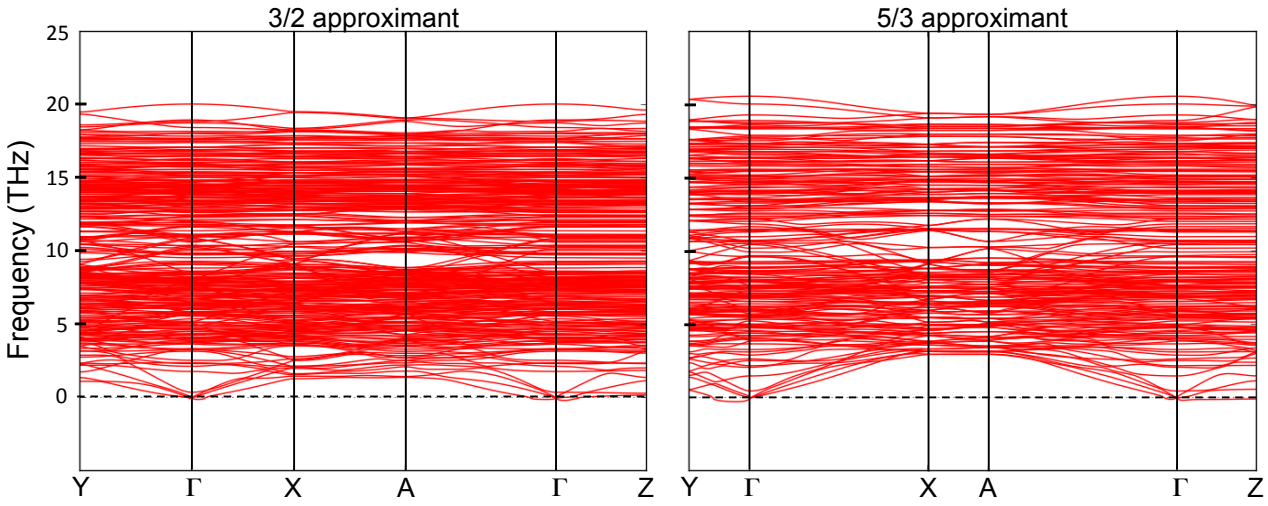

Figure 19. Phonon dispersions along different symmetry directions for the 3/2 (left) and 5/3 (right) approximants. In both cases $U = 5$ eV.

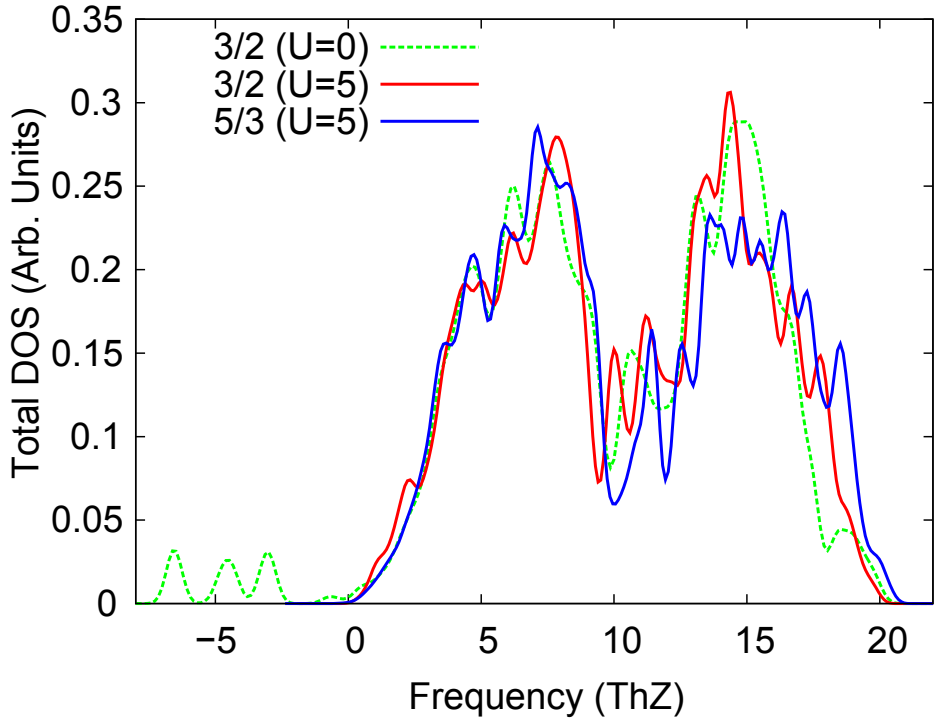

Figure 20. Phonon DOS for the 3/2 ($U = 0, 5$ eV, dashed green and solid red, respectively) and 5/3 ($U = 5$ eV, solid blue) approximants. Negative frequencies obtained for the 3/2 ($U = 0$) approximant correspond to instabilities in the RS subsystem.

calculate the constant volume heat capacity for CCO. The results are displayed in Figure 21 along with the experimental data obtained by Wu *et al.* [76]. The agreement is very good for the three cases; the maximum error corresponds to the 3/2 approximant with $U = 0$ and is only around 5% or less.

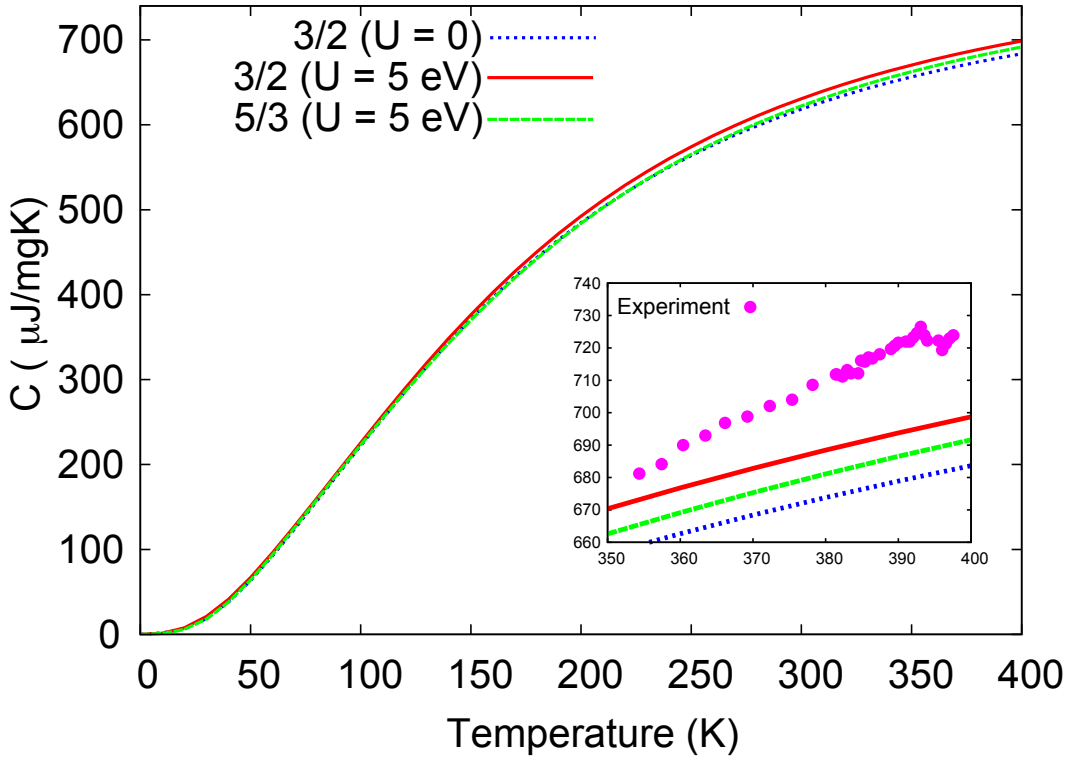

Figure 21. Calculated constant volume heat capacity for the 3/2 ($U = 0, 5$ eV, dotted blue and solid red, respectively) and 5/3 ($U = 5$ eV, dashed green) approximants. The insets compare these values with the corresponding available experimental data (pink solid circles) from Wu *et al.* [76].

4.3.3 Thermal conductivity

As described in Section 4.2, by obtaining the phonon velocities from the full phonon dispersion and then applying the BTE within the relaxation time approximation, the thermal conductivity can be calculated up to a constant τ that, as mentioned before, is taken out of the summation as an adjustable parameter. Typical values for the phonon relaxation times in similar cobaltites are usually of the order of ≈ 1 ps [77]; in this work I have chosen $\tau = 2$ ps in order to fit experimental data from Satake *et al.* [78]. Figure 22 shows the calculated thermal conductivity for the 3/2 and 5/3 approximants for $U = 5$ eV along the a, b and z directions (where z is perpendicular to a and b). These results indicate a highly anisotropic thermal conductivity, mostly between in-plane (ab) and out plane directions (along c), obtaining $\kappa_{ab}/\kappa_c \approx 6 - 8$ for both approximants, which is good agreement with experimental findings by Terasaki *et al.* in another layered cobaltite [77]. In their work they report $\kappa_{ab}/\kappa_c \approx 5 - 10$ for $Bi_{2x}Pb_xSr_2Co_2O_y$. When comparing the two approximants I observe almost the same values for thermal conductivities along a and c, but different behaviors along the incommensurate direction, b. For the 3/2 approximant, κ_b is ≈ 10 mW/Kcm below κ_a, while for the 5/3 it is the other way around. As in the case of the electronic structure, I again obtain a better agreement with experiment for the 5/3 approximant, since according to mesaurements carried out by Satake *et al.*, $\kappa_b < \kappa_a$ for CCO and other layered cobaltites incommensurate along b. This behavior, due to a higher dispersion of phonons along the non-periodic direction, is not captured by the 3/2 periodic approximant but reproduced by the 5/3 one. However, although this model is able to predict the main features of the thermal conductivity, I observe that in my

calculations saturation temperatures are reached are higher temperatures than in the experimental results by Satake *et al.*, where saturation ocurrs at ≈ 50 K. This disagreement may be one of the consequences of the simplifications involved in assuming a constant relaxation time.

By using Equation 4.4, the projected thermal conductivities for each subsystem can be evaluated. Figure 23 shows the corresponding contributions to the total thermal conductivity due to the RS and CoO_2, respectively, along the three Cartesian directions, for the 3/2 and 5/3 approximants. I observe that in all cases, the RS subsystem is the one responsible for most of the contributions to the thermal conductivity. The main differences between the results for the two approximants correspond to the RS thermal conductivities calculated along the incommensurate direction (y), which can be related to the different clustering patterns found along this direction after relaxations, affecting only the RS structure.

Figure 24 displays the thermal conductivity for the 3/2 approximant calculated for $U = 0$. I observe a simlar behavior as in the $U = 5$ eV case; the only difference is that the values of κ are up to 10% higher. The Hubbard term, by adding a repulsive interaction between electrons, loosens the strength of the binding between atoms which in turns results in smaller force constants than in the $U = 0$ case.

4.4 Summary

In this chapter I have reported first principles calculations of the lattice and thermal properties of the misfit-layered thermoelectric CCO, modeled by rational approximants, within the framework of standard DFT and DFT+U. Vibrational spectra, specific heat and thermal conductivities have been calculated for both the 3/2 and 5/3 approximants. Although for the

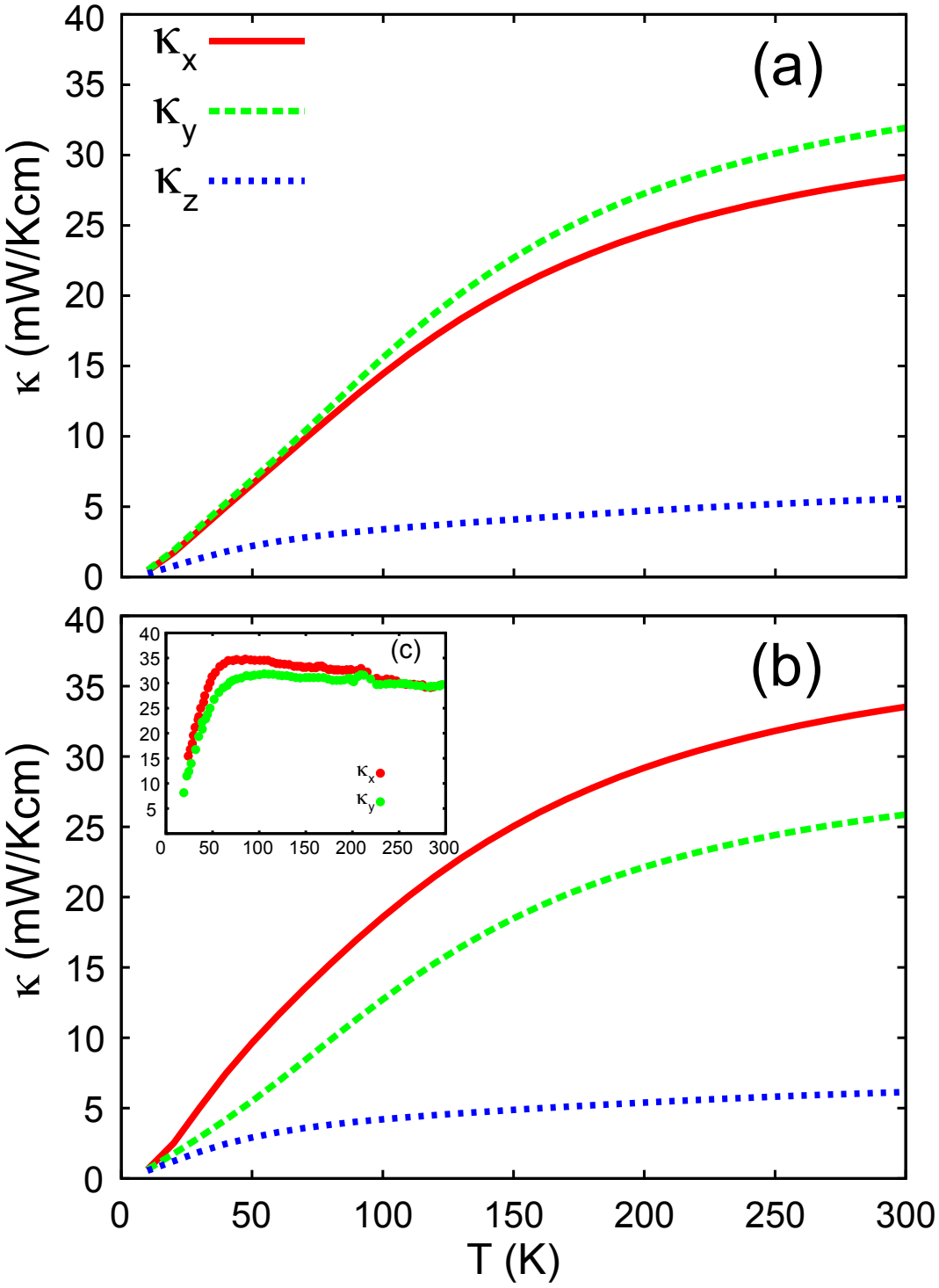

Figure 22. (a) and (b), calculated thermal conductivities for the 3/2 (top) and 5/3 (bottom) approximants along the different Cartesian axis. (c) Experimental values from Satake [78].

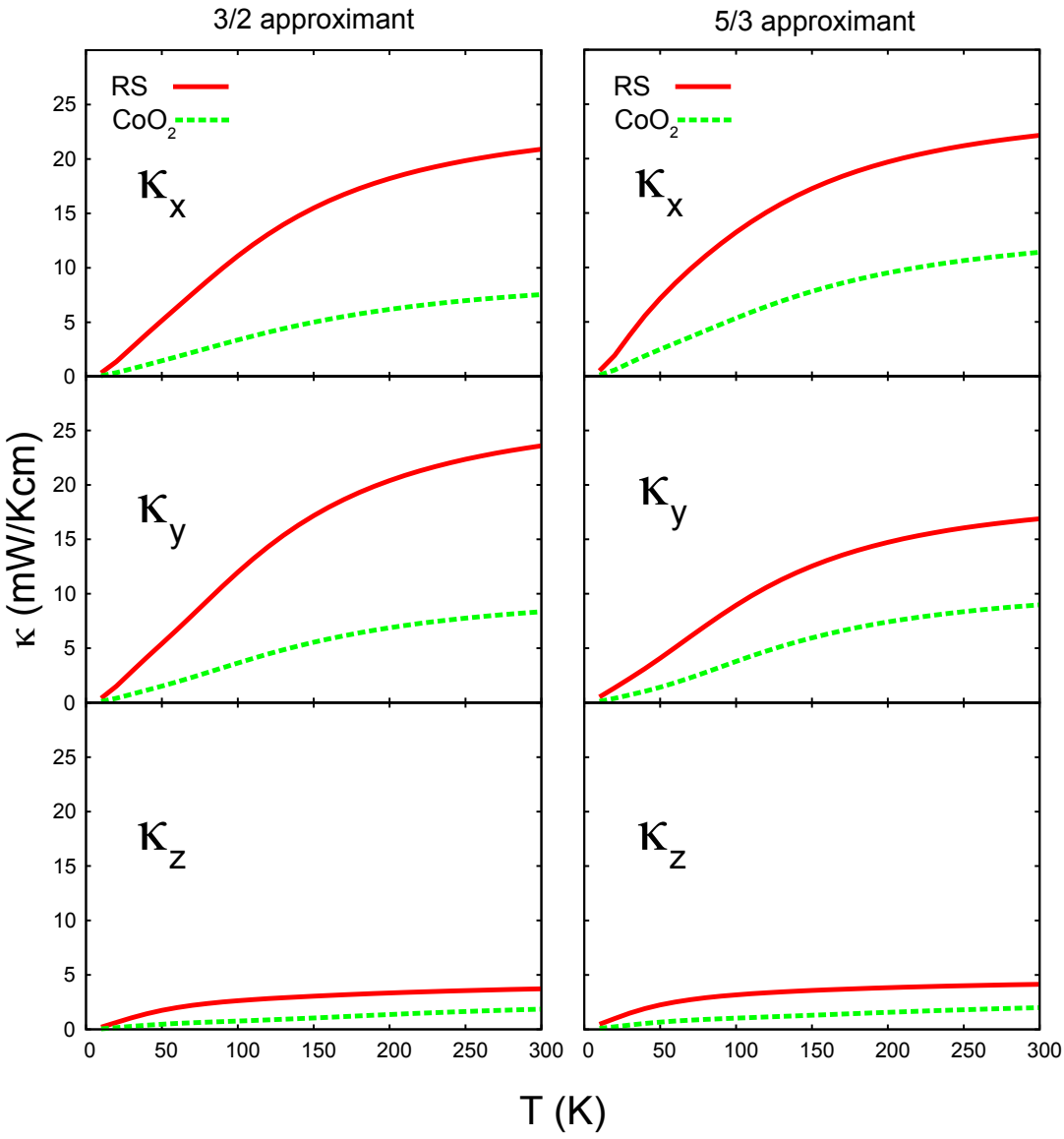

Figure 23. Partial contributions to the total thermal conductivity from each subsystem, RS (solid, red digital) and CoO_2 (dashed, green digital), along the different axis directions for the 3/2 (left) and 5/3 (right) approximants, respectively.

3/2 approximant and $U = 0$ a few negative frequencies are obtained, the phonon DOS exhibit similar features in the three cases considered in this work, i.e., 3/2 with $U = 0, 5$ eV and 5/3 with $U = 5$ eV. Calculated constant volume heat capacities are found to be within a 5% with respect to available experimental data, being the 3/2 approximant the one in better agreement with experiment when we include the U and the worst when we do not inclued it. Thermal conductivities have been calculated by using the Boltzmann Transport Equation, within the relaxation time approximation, assuming τ as an adjustable parameter. Typical values for the relaxation time are in the range $1-5$ ps. Here I obtained that for a value of $\tau = 2$ ps, calculated thermal conductivities are of the same order as the corresponding experimental values. The calculated thermal conductivities show a clear anisotropic behavior along the different lattice directions. In all the cases the ratio $\kappa_{ab}/\kappa_c \approx 5 - 10$, which is in good agreement with experimental data for other layered cobaltites. Although the thermal conductivities along a exhibit similar values for the 3/2 and 5/3 approximants (with $U = 5$ in both cases), the values along the incommensurate direction, b, follow different behaviors. For the 5/3, the value of κ_a is predicted to be greater than the value of κ_b, which is better agreement with experimental results by Satake *et al.* The opposite behavior is observed for the calculated thermal conductivities for the 3/2 approximant. This result reinforces one of the conclusion of chapter 3, where I showed how the 5/3 approximant (with $U = 5$ eV) did a better job than the 3/2 approximant in the prediction of the electronic structure when compared with experiment.

I have also evaluated the dependence of different thermal properties on U. This was only performed for the 3/2 approximant. I did not observe significant differences for the phonon DOS,

however, using $U = 5$ eV slightly improves the agreement of calculated C_v with experiment. In additon, the value of U does not alter the relative ratios between thermal conductivities along the different lattice directions, but their magnitudes seem to scale monotonically with U. Partial contributions to the total thermal conductivity of CCO were also calculated for the 3/2 and 5/3 approximants, and I showed that most of the contributions are due to the RS susbsystem. Although many approximations have to be made in order to calculate the thermal conductivity of CCO from first principles, the model proposed with a 5/3 approximant is able to predict its main features in reasonable agreement with experiment. This method can then be used in the search for better thermoelectric materials, as it gives a way to estimate the thermal conductivity as function of structure and composition. Since, in general, the lattice thermal conductivity is reduced more strongly than the electronic counterpart upon alloying, relative variations with respect to different dopants can thus be assessed from first principles.

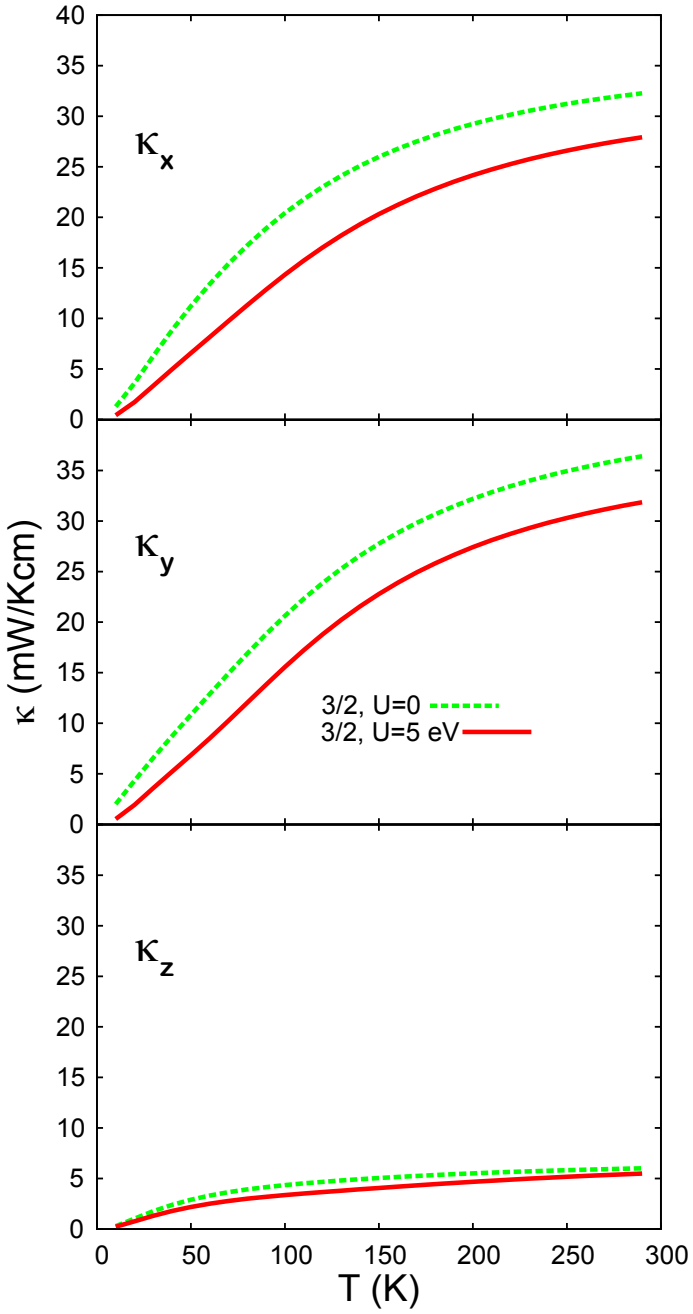

Figure 24. Comparison between calculated thermal conductivities along different Cartesian directions for the 3/2 approximant with $U = 0$ and $U = 5$ eV, respectively.

CHAPTER 5

FIRST-PRINCIPLES STUDY OF COMPENSATION MECHANISMS IN NEGATIVELY CHARGED $LaGaO_3/MgAl_2O_4$ INTERFACES

5.1 Introduction

The fascinating and diverse electrical properties of thin film heterostructures have drawn worldwide attention in recent years [79–82]. The physical origins of this diversity are inherent to the interfacial structures and include symmetry-breaking and epitaxial strain. In turn, the resulting changes in the charge distribution and crystal field can drive atomic relaxations and reconstructions, creating a much larger manifold of possible structures and, consequently, electrical properties compared to parent bulk structures. In particular, interfacial ion transport has been widely investigated in oxide materials. Higher mobility at temperatures below 800°C would have a profound impact on applications in energy conversion devices [11]. Many undoped bulk materials have good mobilities but a limited number of carriers. In many cases, despite the fact that it is possible to increase the number of charged carriers by doping, interactions between dopant ions and their charge-compensating defects lead to the formation of distinct clusters that decrease the mobilities of the migrating species [83]. Some interfaces in oxides are known to enhance ionic diffusion [84–86]. Modifications of interfacial charge to manipulate properties of the space charge layer provide another venue of changing transport properties in the proximity of an interface. If the density of the interfaces is such that space charge layers overlap, one can

expect emergent behavior of ionic transport properties that cannot be interpolated from the bulk counterpart behavior. However, it is well known that grain boundaries in acceptor-doped oxide perovskites [79] and fluorites [80] are typically positively charged relative to the bulk. This leads to oxygen vacancy depletion layers, and a consequent reduction in ionic conduction. For heterostructures with oxygen vacancies as the dominant carriers, a possible route to enhance in-plane interfacial ionic transport is to induce oxygen vacancy enrichment in space charge layers during synthesis. Here, I describe a computational study of such a thin film heterostructure.

Heterogeneous doping is a well-known strategy for enhancing ionic conductivity by increasing the concentration of mobile point defects in the vicinity of the interface (i.e., in the space charge region) [81]. Heterolayers were also demonstrated to significantly improve ionic conductivity in CaF_2/BaF_2 superlattices, with conductivity progressively increasing with increasing interfacial density [82]. Similar strategies have been employed more recently in the case of oxides, with varying degrees of success. For example, Kosacki and co-workers reported that the oxygen ion conductivity of Y_2O_3-stabilized ZrO_2 (YSZ) is significantly enhanced when grown on MgO substrates [87]. Other studies of this system have not found the same enhancement [88, 89]. Korte *et al.* found ionic conductivity to increase linearly with increasing density of phase boundaries in YSZ/Y_2O_3 heterostructures, and the activation energy was found to decrease for strained YSZ layers [90]. There has been much debate on enhanced ionic conductivity along $YSZ/SrTiO_3$ heterointerfaces. Garcia-Barriocanal *et al.* reported an eight order-of-magnitude increase in oxygen ion conductivity [91], although others have argued that the enhanced conduction in that system is electronic rather than ionic in origin [92]. These studies

not only illustrate the potential of heterointerfaces in modulating ionic transport, but also the difficulty in understanding the conduction behavior of oxide interfaces, advancing arguments on the effects of space charge, epitaxial strain and composition variations on ionic conductivity in multilayers. From a computational perspective, there have been several recent first-principles studies aimed at improving the understanding of the properties of polar interfaces [93–98]. Electronic and ionic redistribution were shown to lead to compensation of extra charge at the interface resulting in considerable changes in electronic structure of oxide heterostructures.

The perovskite $LaGaO_3$ (LGO) is an insulator, with very low ionic conductivity. Both La and Ga retain their valence state (+3) in oxides, so when LGO is doped with lower valence cations such as Sr and/or Mg, the oxygen vacancy concentration can be substantially increased. Doped LGO exhibits oxygen ion conductivity comparable to the best oxygen ion conductors [99]. Creating negatively charged interfaces with another material is another possible route to increasing the oxygen vacancy concentration in LGO and possibly inducing enhanced ionic conductivity in the space charge layers adjacent to the interfaces. Here I demonstrate that heterointerfaces in LGO heterostructures with spinel-structured $MgAl_2O_4$ (MAO) can be designed to create negatively charged interfaces. MAO is an insulator with a wide band gap and single-valence cations (+2 and +3 for Mg and Al, respectively). Thus, a charged interface between MAO and perovskite LGO is unlikely to be compensated electronically. A good epitaxial match between MAO and LGO and similar thermal expansion coefficients also motivate my choice of these two materials for this study.

My strategy to induce higher vacancy concentrations involves the use of charged atomic planes as building blocks, as charged surfaces and interfaces require compensation to maintain overall electrical neutrality. Uncompensated polarity in semi-infinite systems causes diverging electric fields, and much work has been devoted to these issues [14]. The compensation is typically achieved by redistribution of electronic charges, changes in local composition at the interface or screening by mobile ions in the space-charge layer. In the presence of mobile charge carriers near an interface, a space charge layer arises, which can be described by the Poisson-Boltzmann equation, assuming purely electrostatic interactions with the interface and each other. However, the specific interactions of mobile carriers with interfacial species near the interface can modify the expected behavior due to variations in the composition, bonding, and structure at the interface in comparison to the bulk. I explore how these interactions can be investigated using first-principles methods and whether they can be included in continuum models.

In this work, I investigate an interface between the perovskite LGO, and the spinel MAO, which both exhibit alternating positive and negative charged (001) planes (see Figure 5). Experimentally, perovskite-spinel heterointerfaces are known to form spontaneously as a result of phase separation [100]. The interfacial planes of both materials in my model are negatively charged, giving rise to an excess negative charge that is compensated by oxygen vacancies in the space charge layer. Thus, the heterostructure maintains overall electrical neutrality and, at the same time, allows us to investigate different vacancy distributions next to the interface and determine specific interactions. I compare electronic and ionic compensation mechanisms and

determine electron density distributions self-consistently in each case via first-principles calculations. Based on the results of those calculations, I model band-bending and distributions of vacancies using the Poisson-Boltzmann equation. The rest of the paper is organized as follows. In Section II, the computational methods and parameters are provided. In Section III, I present results for the computed properties of bulk LGO and MAO phases with and without vacancies, followed by structural energetics and electronic structures of the LGO(001)//MAO(001) interfaces for different oxygen vacancy distributions. In Section IV, my results from first principles computations are used to estimate the distribution of charged vacancies within the framework of the Poisson-Boltzmann equation. Finally, I summarize my results in Section V.

5.2 Computational Details

5.2.1 Method

All calculations were performed within the framework of density functional theory (DFT) using the projector augmented wave method as implemented in VASP with the Perdew-Burke-Ernzerhof exchange-correlation functional [61]. Unless specified otherwise in the next subsection, I used a cutoff energy of 530 eV for wavefunctions. The **k**-point meshes for structure optimizations, total energy, and density-of-states (DOS) calculations for the various structures considered are also given in the next subsection. All structures were optimized using criteria of total-energy-convergence to within 0.1 meV and residual forces to less than 0.02 eV/Å. DOS calculations were performed using the tetrahedron method. For DOS and total energy calculations of the relaxed structures, the number of **k**-points and the energy cutoff for wavefunctions

were chosen in order to ensure energy convergence to within 0.01 eV. Bader analysis was used to determine ionic charges.

5.2.2 Computational Procedures

5.2.2.1 Bulk

First, I optimized geometries of bulk LGO and MAO structures. Of the three polymorphs for LGO (cubic, orthorhombic and rhombohedral), I performed calculations using the orthorhombic structure (o-LGO), which is known to be the one with the lowest ground state energy [101]. Full structural optimization for o-LGO was performed on a supercell containing 20 atoms, starting from the experimental lattice constants [102] $a = 5.523$ Å, $b = 5.491$ Å, and $c = 7.772$ Å, using a $4 \times 4 \times 4$ **k**-point mesh. For MAO bulk calculations, a cubic supercell containing a total of 56 atoms was considered. Starting from the experimental cubic lattice parameter[103] $a = 8.075$ Å, the structure was fully optimized using a $6 \times 6 \times 6$ **k**-point mesh.

For structural optimization of LGO or MAO structures with oxygen vacancies (V_O) I used supercell models. For LGO I used a $\sqrt{2} \times \sqrt{2} \times 1$ supercell and considered three different cases: one V_O per cell (since the structure is quasi-cubic, various oxygen sites can be considered to be equivalent), two V_O's located at the maximal separation in the same LaO plane, and two V_O's located at the maximal separation in the same GaO_2 plane. The in-plane distance between two V_O sites is $\sqrt{2}a = 5.77$ Å. Geometry optimization for one V_O in MAO was done using the same supercell as in the bulk calculations. In these geometry optimizations, only the internal parameters were allowed to relax, keeping the lattice parameters fixed at their previously optimized values. In vacancy calculations I used $3 \times 3 \times 3$ and $5 \times 5 \times 5$ **k**-point

meshes, and wavefunction energy cutoffs of 425 and 400 eV for LGO and MAO, respectively. DOS and single-point total energy calculations were performed using a $4 \times 4 \times 4$ **k**-point mesh for LGO bulk and a $10 \times 10 \times 10$ **k**-point mesh for MAO bulk. In cases of LGO and MAO with oxygen vacancies, DOS calculations were performed using $6 \times 6 \times 6$ and $10 \times 10 \times 10$ **k**-point meshes, respectively.

5.2.2.2 Heterostructure

The model of the LGO(001)//MAO(001) interface was constructed by putting together a GaO_2-terminated LGO slab and an AlO_2-terminated MAO slab. In this way LGO and MAO slabs have non-stoichiometric structures of the type $(GaO_2)^{1-}$/ $(LaO)^{1+}$/.../$(LaO)^{1+}$/$(GaO_2)^{1-}$, and $(AlO)^{1-}$/$(1/2Mg)^{1+}$/... /$(1/2Mg)^{1+}$/$(AlO)^{1-}$, respectively, where charge per plane is given under the assumption that the ions are in their formal valence states. Since formation energies are significantly higher in the MAO structure, the extra charge due to deviations from stoichiometry is compensated by oxygen vacancies in the LGO part of the structure. The MAO portion of the (001) superlattice used in our calculations consists of 5 $(AlO)^{1-}$ and 4 $(1/2Mg)^{1+}$ stacking planes, amounting to a total of 64 atoms. For the LGO part, I used 9 $(GaO_2)^{1-}$ and 8$(LaO)^{1+}$ intermediate planes, in order to minimize the interaction between the periodic negatively charged interfaces and also to ensure a more "bulk-like" behavior away from the boundary. As a result the present model for the LGO//MAO heterostructure has the form: $(GaO_2)^{1-}\{(LaO)^{1+}(GaO_2)^{1-})\}_8//(AlO)^{1-}\{(1/2Mg)^{1+}(AlO)^{1-}\}_5$, with a total of 232 atoms. The LGO(001)//MAO(001) interface is shown schematically in Figure 25.

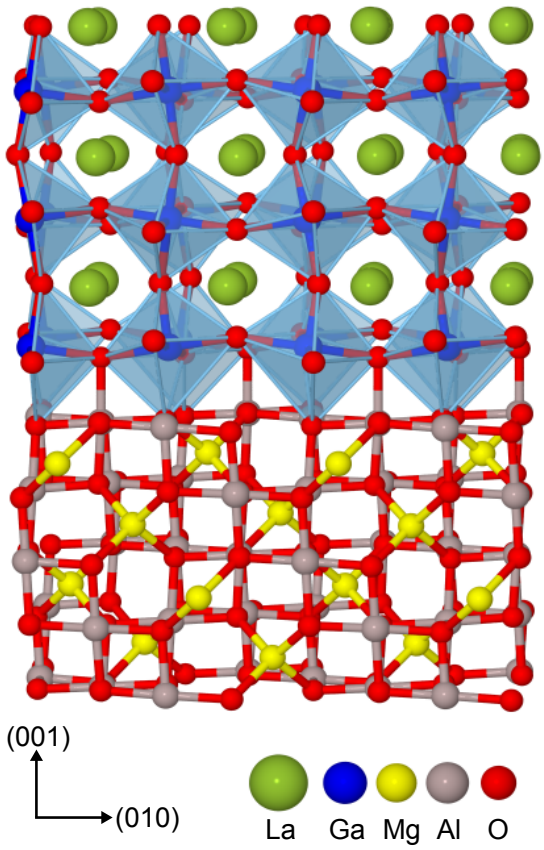

Figure 25. Side view of initial configuration of the o-LGO//MAO interface. The interface is formed by $(AlO_2)^{-1}$ and $(GaO_2)^{-1}$ planes, which results in an excess negative charge. For o-LGO, tilted octahedra with a central Ga atom are displayed.

In the present work, MAO is considered to be a substrate with multilayers of LGO and MAO grown on top of it. Therefore, the lattice parameters of quasi-cubic LGO along x and y directions (considering z to be the direction perpendicular to the interface) were fixed at the optimized lattice parameter of (001) MAO to simulate epitaxy. All internal parameters were optimized, as well as the lattice parameter along z for the whole supercell. Among the various configurations for the heterostructure of LGO on MAO, I have chosen the one with the lowest total energy, and used it in order to construct the initial structures of the interfacial structures with different vacancy configurations considered. Oxygen vacancies in the heterostructure were created in LaO and GaO_2 planes located at different distances from the interface with the same in-plane separations between two V_O sites as in the bulk.

5.2.3 Chemical Potentials

The formation energy for oxygen vacancies (E_{V_O}) per vacancy was calculated using

$$E_{V_O} = \frac{E_t(V_O) - E_t}{N_{V_O}} + \mu_O, \tag{5.1}$$

where $E_t(V_O)$ and E_t refer to the total energies of the systems with and without V_O, respectively, and N_{V_O} is the number of vacancies. The system is assumed to be in equilibrium with O_2 in gas phase. Therefore, the chemical potential of oxygen at temperature T and partial pressure p is uniquely determined as $\mu_O = \frac{1}{2}\mu_{O_2(\mathrm{gas})}(T, p)$, which can be expressed in terms of the chemical potential of oxygen at temperature T and $p^0 = 1$ atm partial pressure as $\mu_{O_2(\mathrm{gas})}(T, p) =$

$\left(\mu_{O_2}(T,p^0) + kT\ln\frac{p}{p^0}\right)$. The expression for $\mu_{O_2}(T,p^0)$ can be obtained by dividing it into enthalpy (H) and entropy (S) contributions as

$$\mu_{\mathrm{O}_2}(T,p^0) = \left(H_{\mathrm{O}_2}(T,p^0) - H_{\mathrm{O}_2}(0,p^0)\right) - TS_{\mathrm{O}_2}(T,p^0) + H_{\mathrm{O}_2}(0,p^0). \tag{5.2}$$

Assuming that $H_{\mathrm{O}_2}(0,p^0)$ corresponds to the total energy of the O_2 molecule, and by obtaining H and S from thermochemical tables [104], the above equations can be combined to give μ_O at any given T and p. In order to compute the total energy of O_2 in the gas phase, I placed an O_2 molecule in a $14 \times 15 \times 16$ Å^3 supercell, and performed spin-polarized calculations with an energy cutoff of 900 eV for the wavefunctions and Γ-point sampling.

The interface energy for a LGO//MAO heterostructure is defined as

$$E_{\mathrm{int}} = (E_t - N_{\mathrm{La}}\mu_{\mathrm{La}} - N_{\mathrm{Ga}}\mu_{\mathrm{Ga}} - N_{\mathrm{Mg}}\mu_{\mathrm{Mg}} - N_{\mathrm{Al}}\mu_{\mathrm{Al}} - N_{\mathrm{O}}\mu_{\mathrm{O}})/2A, \tag{5.3}$$

where E_t is the total energy of the LGO//MAO system, A is an interface area per supercell and N_X, μ_X refer to the number of atoms of type X in the supercell and their chemical potentials in respective bulk oxides. The factor of 2 accounts for the fact that by construction there are two identical interfaces in a periodic LGO//MAO supercell. In order to evaluate the limits on chemical potentials of Ga and Al, calculations were also performed by full relaxations from the experimental parameters [105, 106] of monoclinic $\beta - Ga_2O_3$ and trigonal $\alpha - Al_2O_3$ using **k**-point meshes of $4 \times 12 \times 8$ and $6 \times 6 \times 6$, respectively.

The chemical potentials are derived assuming thermodynamic equilibrium with $LaGaO_3$, $MgAl_2O_4$, Ga_2O_3 and Al_2O_3, which results in the following set of equations:

$$\mu_{\mathrm{La}} + \mu_{\mathrm{Ga}} + 3\mu_{\mathrm{O}} = \mu_{\mathrm{LaGaO_3}}, \tag{5.4}$$

$$\mu_{\mathrm{Mg}} + 2\mu_{\mathrm{Al}} + 4\mu_{\mathrm{O}} = \mu_{\mathrm{MgAl_2O_4}}, \tag{5.5}$$

$$2\mu_{\mathrm{Ga}} + 3\mu_{\mathrm{O}} = \mu_{\mathrm{Ga_2O_3}}, \tag{5.6}$$

$$2\mu_{\mathrm{Al}} + 3\mu_{\mathrm{O}} = \mu_{\mathrm{Al_2O_3}}, \tag{5.7}$$

where $\mu_{\mathrm{LaGaO_3}}$, $\mu_{\mathrm{MgAl_2O_4}}$, $\mu_{\mathrm{Ga_2O_3}}$, and $\mu_{\mathrm{Al_2O_3}}$ are the calculated total energies per formula unit of bulk LGO, MAO, Ga_2O_3, and Al_2O_3, respectively. I calculate vacancy formation energy (Equation 5.1), and interface energy E_{int} (Equation 5.3) by expressing all of the individual cation chemical potentials from Equation 5.4 to Equation 5.7 along with Equation 5.2 for μ_{O} .

5.3 Results and Discussion

5.3.1 Calculated Structures and Electronic Properties of Bulk LGO and MAO

The optimized bulk lattice parameters along with corresponding experimental values for LGO and MAO are given in Table I. For both LGO and MAO, the calculated lattice parameters are slightly overestimated, by $\approx 1\%$, with respect to the corresponding experimental values, giving a lattice mismatch of 4.2%, slightly bigger than the experimental value of 3.7%.

Figure 26 shows the computed partial DOS for bulk LGO and MAO. The calculated bandgap values are given in Table I. As expected, LGO shows an insulating behavior with a bandgap of 3.74 eV, which is underestimated with respect to the experimental value of 4.4 eV, but in

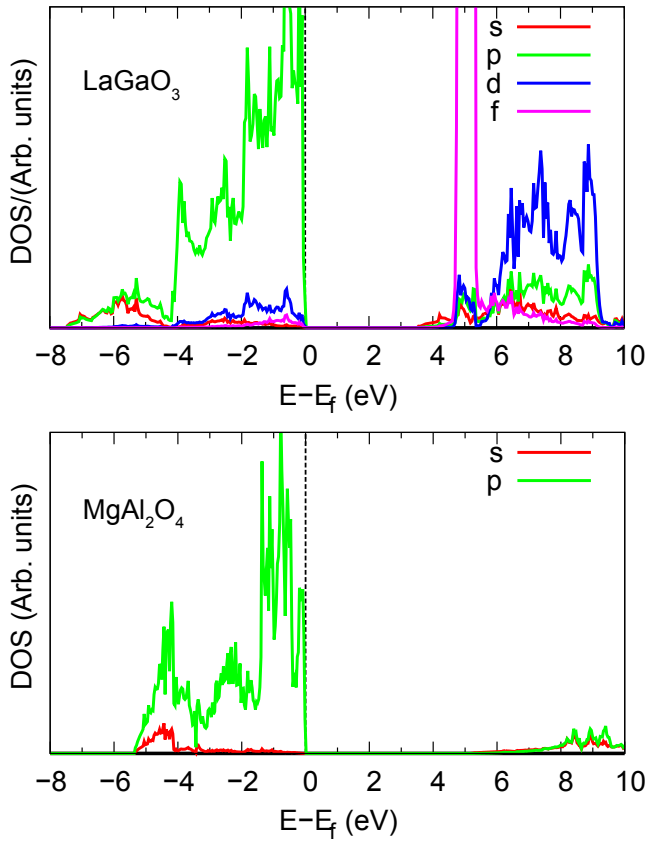

Figure 26. Projected DOS for bulk LGO (top) and MAO (bottom). Both structures display insulating behavior with bandgaps calculated to be 3.74 and 5.00 eV, respectively.

agreement with previous DFT calculations using GGA [107]. The main contributions to the DOS at the top of the valence band are from the hybridized O $2p$, and Ga $3d$ and $4p$ states. In the conduction band, the high intensity peak at ≈ 5 eV represents the unoccupied La $4f$ states. For MAO, a bandgap of 5.00 eV is underestimated with respect to the experimental value of 7.8 eV [108]. The upper valence band contains mostly O $2p$ orbitals, while the lower part of the

conduction band corresponds to unoccupied Al $3p$ and Mg $3s$ orbitals. These results for MAO are also in good agreement with previous DFT calculations using GGA [109].

TABLE VII

Calculated and experimental bandgaps and lattice parameters of LGO and MAO.

	Calculated				Experimental [102, 103, 107, 108]			
		Lattice Parameters (Å)				Lattice Parameters (Å)		
	Bandgap (eV)	a	b	c	Bandgap (eV)	a	b	c
LGO	3.74	5.57	5.55	7.88	4.4	5.523	5.491	7.772
MAO	5.00	8.16	-	-	7.8	8.075	-	-

5.3.2 Oxygen vacancies in bulk LGO and MAO

I performed geometry optimization of structures with oxygen vacancies created in the LGO and MAO bulk as described in the previous Section. The formation energies for V_{O} in LGO and MAO were calculated using different concentrations of vacancies, $N_{V_{\mathrm{O}}}/N_{\mathrm{O}}$, where $N_{V_{\mathrm{O}}}$ and N_{O} are the number of V_{O}'s and available O sites in the supercells, respectively. I considered $N_{V_{\mathrm{O}}}/N_{\mathrm{O}}$ values of 1/32 for MAO and 1/24 and 2/24 for LGO. The results for the formation energies $E_{V_{\mathrm{O}}}$ (Equation 5.1) are given in Table II. They show that the vacancy formation energy for MAO at the lowest calculated concentration is significantly higher than that for LGO (by $\approx$ 1.5 eV), suggesting that in an LGO//MAO heterostructure the formation of V_{O} should be energetically more favorable in the LGO subsystem than in MAO.

Next, I consider interactions between vacancies in LGO by comparing calculations with different oxygen vacancy concentrations. Table II shows formation energy of oxygen vacancy

TABLE VIII

Formation energies for V_O in bulk LGO and MAO. See the text for vacancy concentrations.

1/24 V_O concentration	**Formation Energy (eV)**
LGO	5.14
MAO	6.65
2/24 V_O concentration	
LaO plane (LGO)	5.28
GaO_2 plane (LGO)	5.19

for 1/24 and 2/24 vacancy concentrations, respectively. In the latter case, two V_O's, instead of one, are created in bulk LGO. In this case two scenarios were considered: two V_O's located in (a) a GaO_2 plane and (b) a LaO plane. The $V_O - V_O$ distance of 5.77 Å, was the same in both cases, which is the maximum possible in-plane distance for V_O's in the present supercell configuration. As indicated by the formation energies in Table II, the interaction of vacancies is repulsive and relatively weak, with interaction energies of 0.025 and 0.07 eV per vacancy for V_O's in GaO_2 and LaO planes, respectively, resulting in similar vacancy formation energies for 1/24 and 2/24 concentrations. Comparing the formation energies of vacancies in LaO versus the GaO_2 planes at the same concentrations, we find the vacancies to have a slight preference to be in a GaO_2 plane (by 0.045 eV). We note that in the bulk structures vacancies are formally not charged, since a neutral O atom is removed from the supercell to create a vacancy. In the forthcoming discussion of results for the heterostructures, each heterostructure considered in our calculations formally has a total of $-4e$ extra charge at the interface (per supercell), which requires two compensating positively charged oxygen vacancies, denoted by $V_O^{\bullet\bullet}$ in the Kröger-

Vink notation. Therefore, vacancy interactions in the bulk LGO and in the heterostructure might not be directly comparable.

5.3.3 Structure and Interface Energies of the LGO//MAO Heterostructures

In our model of the LGO//MAO interface, a GaO_2 plane of LGO with a nominal charge of $-1e$ per formula unit is placed next to an AlO_2 plane of MAO with the same nominal charge of $-1e$ per formula unit, introducing an extra negative charge at the interface. In polar interfaces, the required charge compensation may be achieved by different mechanisms [94, 95, 14], such as (i) a change in the number of electrons, as in $AlO_2/LaO/TiO_2$ interfaces in $LaAlO_3//SrTiO_3$ superlattices, where the extra electrons are placed in the $SrTiO_3$ conduction band, and/or (ii) by an atomic reconstruction, as in the case of the $AlO_2/SrO/TiO_2$ interfaces [93], where charge compensation is achieved by the introduction of oxygen vacancies [110]. In order to compare different compensation mechanisms and to find the most favorable, I considered the following configurations: (a) LGO//MAO interface with no vacancies, (b) LGO//MAO interface fully compensated by oxygen vacancies.

As mentioned above, for the heterostructure model considered here, two V_O's (per each of two interfaces in the supercell) are required to achieve compensation, since each GaO_2 or AlO_2 plane is represented by a total of four formula units in the supercell, resulting in an extra charge of $-4e$ per interface. In order to compare different vacancy arrangements in the heterostructure in the latter case, I calculated the LGO//MAO heterostructure with two vacancies per interface located in either the GaO_2 or LaO plane at different distances from the interface. The two V_O's

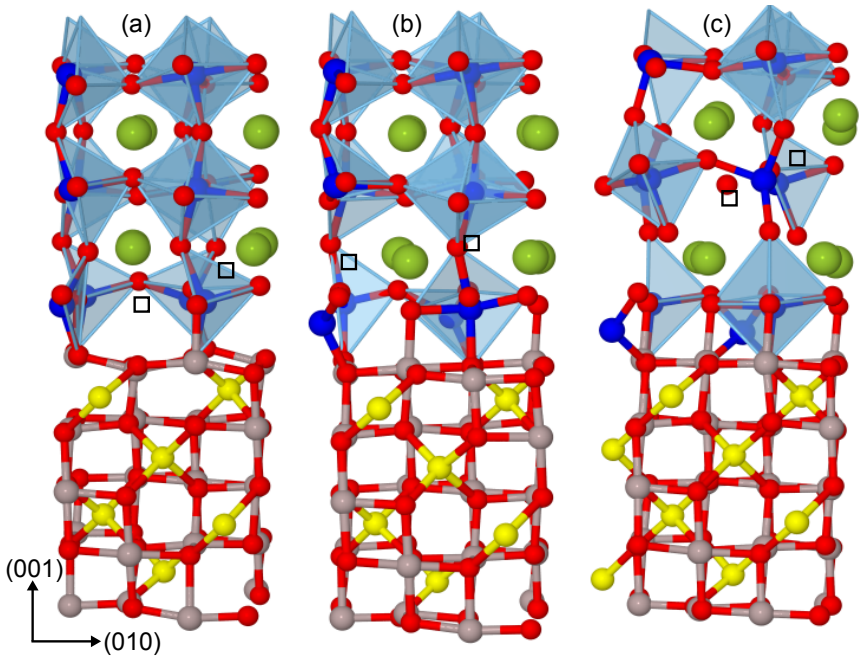

Figure 27. Relaxed structures of the LGO//MAO interface along (001) and (010) directions for vacancies located in (a) the first plane, (b) the second plane, and (c) the third plane. Small squares show the approximate location of the vacancies.

were created in either GaO_2 or LaO planes by removing negatively charged oxygen ions, thus making overall heterostructure electrically neutral (i.e. compensated).

Optimized geometries of heterostructures with vacancies in either of the first three layers are shown in Figure 27. For a more quantitative description of the structures, average displacements along z for atoms located in planes 1, 2 and 3 of LGO are presented in Figure 28. When the vacancies are in the first layer, the oxygens in this layer displace outward by about 0.3 Å on average, driven by electrostatic interactions with a negatively charged interface. Displacements of cations in the first three layers are small in this structure. There is a nearly uniform out-

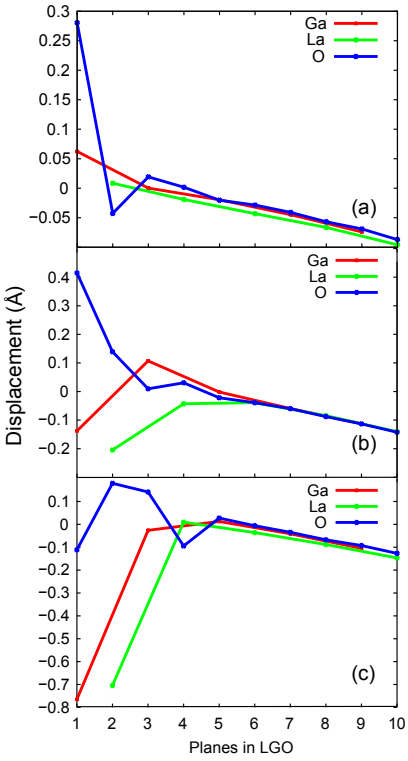

Figure 28. Average displacements for La, Ga, O as a function of the plane in which they are located when V_O's are located in (a) the first plane, (b) the second plane, and (c) the third plane.

of-plane compressive strain beyond the third layer, which is a common feature of all three structures presented in Figure 27. Structures corresponding to vacancies in the second (GaO_2) and third (LaO) planes are characterized by a more pronounced reconstruction in the interface region. When the vacancies are in the second plane (LaO), two of the Ga ions in the GaO_2 plane adjacent to the interface move towards the MAO region by about 0.15 Å following the pattern of Mg ions. The outward displacement of O atoms by 0.4 Å on average is somewhat higher than in the previous case. When the vacancies are in the third plane (GaO_2), the two

Ga ions align with Mg ions and are located exactly where the next layer of Mg atoms would be located in a periodic MAO structure. The displacements of O atoms, on the other hand, are much smaller than in previous cases. We note that the crystal field effects are expected to be strong in MAO because of the predominantly ionic character of bonding. This favors location of positive atoms (Ga) in LGO near the interface in ionic positions (Mg) of the truncated MAO lattice. Additional explanation for this structural rearrangement is a higher structural flexibility of the interfacial planes as a result of removing oxygens from the second or third planes, which weakens the bonding between the first planes next to the interface. This results in more degrees of freedom for interface reconstruction. This is not the case when vacancies are removed either from the first plane or from planes beyond the third plane into the LGO structure (not shown).

The formation energies of oxygen vacancies were calculated using Equation 5.1. Here, all energies are referenced to the same heterostructure without vacancies referred to in the compensation mechanism (a) above. These relative energies of formation are plotted in Figure 29. In many cases, due to the underestimation of bandgaps, the application of LDA or GGA exchange functionals results in incorrect formation energies. The effects are stronger when charged defects are introduced into the system, but also occur when neutral defects introduce new single-particle states that are occupied by electrons. This does not apply to our case (LGO//MAO), where neutral oxygen atoms are removed from the system and where, apart from a small reduction in the bandgap, no new single-particle states were observed in the DOS [111]. Negative vacancy formation energy indicates that an oxygen vacancy would be preferred to electronic charge

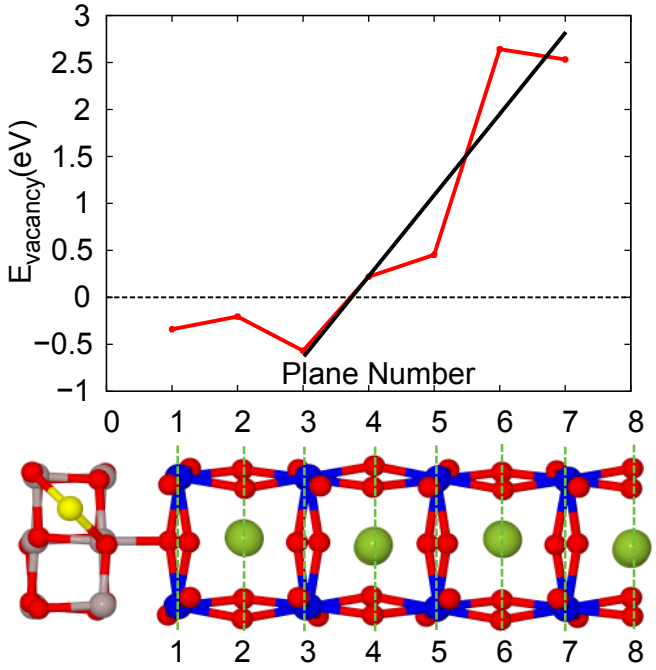

Figure 29. Formation energies for oxygen vacancies located in different LGO planes. Starting at plane 3, formation energies can be linearly interpolated, as shown by a straight line, reflecting the effect of the electrostatic potential generated by the negative charge distribution at the interface. (See Section IV).

transfer in order to compensate the excess charge at the interface. This is the case for vacancies belonging to planes 1 (GaO_2), 2 (LaO), and 3 (GaO_2), but not for vacancies located deeper in bulk LGO. The minimum in energy is achieved when the vacancies are located in plane 3 (GaO_2), corresponding to the most stable configuration. We can also calculate the formation energies for V_O's in different planes as a function of the oxygen partial pressure in the range from 10^{-12} to 1 atm at room temperature (using the formalism summarized in Section II.C). The results for the first five planes are shown in Figure 30.

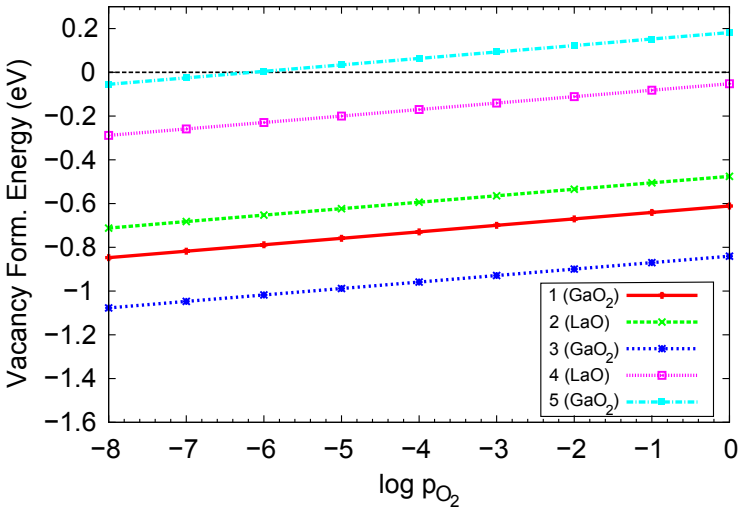

Figure 30. Formation energies of oxygen vacancy calculated as a function of oxygen partial pressure (atm) at a temperature of 298.5 K. Each line corresponds to vacancies located in a different plane.

Interface energies for the heterostructure with V_O's in the third (GaO_2) plane and for the heterostructure without vacancies were calculated using Equation 5.3. Typical values for interface energies are $\approx 1-3$ J/m^2. The results for the interface energies for the two cases - without vacancies and with vacancies in the third plane - are shown as a function of the oxygen partial pressure in Figure 31. We observe that even for very high pressures the interface with vacancies has the lower energy.

5.3.4 Charge distribution and electronic properties of LGO//MAO heterostructures

Since the electron distributions in our calculations are determined self-consistently, the electrons in the nominally charged planes can redistribute. For example, if one-electron levels associated with vacancies are lower in energy than the states in the interfacial planes, the

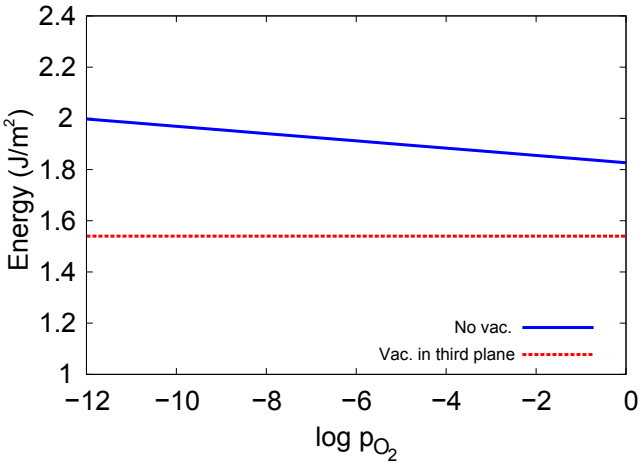

Figure 31. Interface energy computed using Equation 5.3 as a function of the oxygen partial pressure for an interface without any V_O's (solid line) and with V_O's located in the third (GaO_2) plane of LGO (dashed line).

vacancies might trap electrons and change their valence state. This is likely to affect charge compensation mechanisms and ionic conductivity in the space charge layer. In order to investigate charge compensation in the LGO//MAO heterostructure in detail, I address electron charge distribution. A Bader analysis was performed to obtain the charge state for each atom in the heterostructure and then these values were summed up for each atomic plane parallel to the interface in order to calculate the total charge per plane.

The charge profile for the structure with V_O's created in the third (GaO_2) planes from each interface is shown in Figure 32. As expected, the MAO is more ionic than LGO. In fact, the charges per plane for MAO are twice higher than those for LGO despite the fact that the nominal charges of the planes obtained by summing up formal charges of the constituent

ions are the same in both materials. The charges in the planes away from the interface are very similar to bulk charges, with the notable exception of the planes with V_O's. It is evident that after vacancy creation and relaxation the interface remains negatively charged, while V_O's exhibit positive charge and do not accept electrons from the interfacial planes or elsewhere. This charge state corresponds to two $V_O^{\bullet\bullet}$ located in the third (GaO_2) plane.

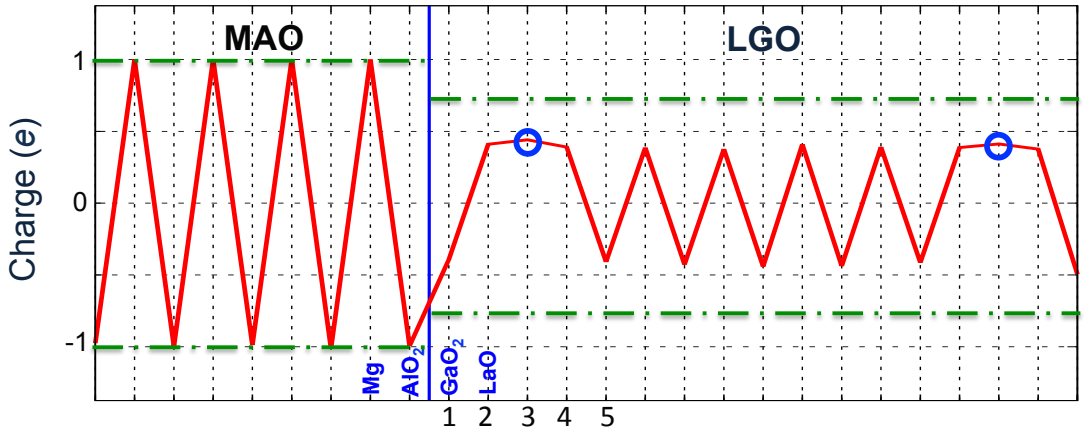

Figure 32. Total charge per plane for the LGO//MAO heterostructure with vacancies located in the third plane. (Blue) circles represent the location of the vacancies and dashed horizontal lines (green) represent the bulk values of the charge in the planes.

Next I consider the effect of different compensation mechanisms on the electronic structure. Since it is known that DFT produces bandgaps that are too low compared to experimental values, these results should be taken as qualitative. The bandgaps for heterostructures with different positions of the plane in which the vacancies are located are plotted in Figure 33. As

the vacancies are placed farther away from the interface, the bandgaps decrease. However, for the configuration with the lowest energy in our calculations (vacancies in the third plane), the heterostructure is still insulating and exhibits a bandgap of 1.78 eV. The bandgaps become small for heterostructures with vacancies located beyond the fourth plane. This decrease in the bandgap with the increasing distance between the plane containing the vacancies and the interface, can be qualitatively understood as sketched in Figure 33. The negative charge at the interface plane together with the positive charge of the plane containing the vacancies creates an electric field inside the LGO region in-between these two planes, thus generating a linear potential that bends both the valence and conduction bands. The bandgap, calculated as the difference between valence band maximum and conduction band minimum, decreases linearly with the distance. If we use an extrapolation, a large concentration of vacancies away from the interface would result in a metallic state as the distance increases. This is in contrast to the compensation mechanism without the vacancies, where the position of compensating charge does not vary. Therefore, predominantly ionic conductivity seems to be possible, since the heterostructure maintains the band gap with the compensating vacancies at the most favorable distance from the interface. In the next section, I consider the distribution of vacancies in order to validate this point.

5.4 Vacancy Distribution using the Poisson-Boltzmann Equation

In the previous sections I have determined the formation energies, charge states and microscopic configurations for vacancies in the LGO//MAO heterostructure at 0 K within the framework of DFT. However, it is also important to know how vacancies would be distributed

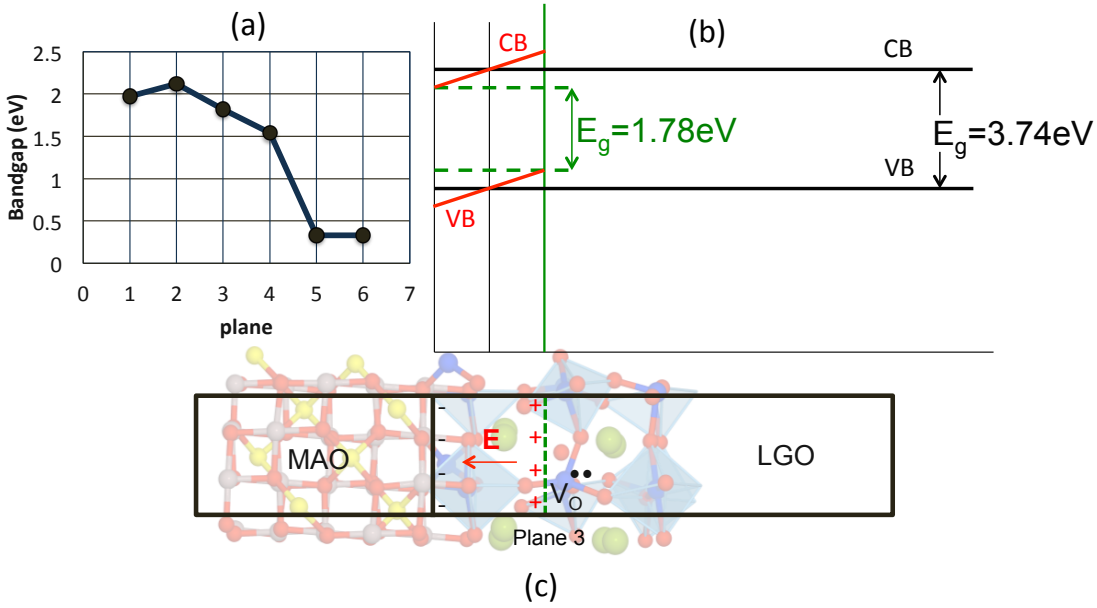

Figure 33. (a) Bandgap as a function of the location of vacancies. (b) Schematic of the valence and conduction band bending in the region between the positively charged vacancies and the negatively charged interface. Indicated value of bandgap corresponds to the case when V_O's are located in the third plane. (c) Schematic of the electric field in LGO.

at finite temperatures and thus to determine the spatial extent of the charge-compensating layer. One way to give a macroscopic description of the LGO//MAO system at finite temperature is to consider the Poisson-Boltzmann (P-B) equation, which has been used by others in the study of carrier distribution in ionic conductors [112, 113]. Within this approach, the distribution of charged carriers in the presence a surface charge density is determined by their electrostatic energy and the Boltzmann statistics. The input parameters for this model are the dielectric constant of the medium, the charge density at the interface and the charge of each mobile particle [in this case, oxygen vacancies ($V_O^{\bullet\bullet}$)]. First, we establish a correspondence

between the input parameters of the P-B model and our DFT results. We start by noticing that the formation energy for $V_O^{\bullet\bullet}$'s displayed in Figure 29 can be thought as composed of two contributions: on the one hand the energy resulting from the electrostatic interaction between the charged vacancy (charge $+2e$) and the negatively charged interface (E_e), and on the other hand an intrinsic contribution (E_i) which includes short-range effects (such as structural, chemical, etc.). In this way we can write $E_{V_\mathrm{O}} = E_i + E_e$. Guided by the discussion in the previous section (Figure 33c), we can express the electrostatic contribution as

$$E_e = \frac{\sigma e}{\epsilon_r \epsilon_0} z, \tag{5.8}$$

where z is the coordinate in the direction perpendicular to the interface, σ is the charge density at the interface, and ϵ_r is the relative dielectric constant of LGO. From Figure 29, we observe that the formation energy per $V_O^{\bullet\bullet}$ grows almost linearly starting from plane 3 (GaO_2 layer) and going into the bulk. I conclude from this observation that when the vacancies are located closer to the interface than the third atomic plane, the electrostatic contribution to E_{V_O} is not the dominant contribution to the vacancy energy since strong structural rearrangement in the interfacial region results in E_{V_O} approximately equal to E_i. On the other hand, if the vacancies are located farther away from the interface than the third plane, the relaxations in the first several planes next to the interface are much smaller and the electrostatic energy of these vacancies can be reasonably approximated by Equation 5.8. Thus, by assuming that the intrinsic contribution to the vacancy formation energy, E_i, is a constant, we can calculate σ/ϵ_r from the slope of the interpolating line shown in Figure 29. Taking into account that σ is

determined by the extra charge placed at the interface, and using the value that corresponds to $-4e$ per unit cell ($\sigma = -0.96$ C/m^2), we obtain $\epsilon_r = 24.8$, which is in very good agreement with the experimental value of 25.20 at room temperature for the (001) direction [114]. Such a good agreement between the microscopic (DFT) and the macroscopic (electrostatic) models, serves as a validation for the applicability of the P-B analysis developed in the rest of this section. We can now write the P-B equation for $V_O^{\bullet\bullet}$'s (charge $+2e$) in the LGO part of the heterostructure as

$$\frac{d^2\phi}{dz} = -\frac{2e\rho_0}{\epsilon_r\epsilon_0} e^{-\frac{2e\phi}{k_B T}}, \tag{5.9}$$

where ρ_0 is defined as the density of vacancies at a point where the potential $\phi(z)$=0, and can be determined by the requirement that the charge at the interface is compensated by the total charge of the vacancies. This equation takes into account the fact that the potential due to the interfacial charge density is screened by the vacancies. Solving Equation 5.9, we obtain the density of vacancies as a function of z

$$\rho(z) = \frac{\epsilon_r\epsilon_0 k_B T}{2e^2\left(z + \frac{\epsilon_r\epsilon_0 k_B T}{e\sigma}\right)^2}. \tag{5.10}$$

In Figure 34 I plot the vacancy concentration as a function of the distance to the interface for temperatures of 300 and 800 K, respectively. In order to show how the value of the interfacial charge would affect the equilibrium distribution, I also plot the concentration of vacancies for different interfacial charge densities ($\sigma/10$ and $\sigma/100$). We observe that for $\sigma = -0.96$ C/m^2

at both temperatures the density of vacancies decreases abruptly when going away from the interface, which means that most vacancies are located in plane 3. For an interfacial charge density of $\sigma/100$, vacancies would distribute more uniformly across the structure.

It is illustratrive to compare resulting distributions with the highest vacancy concentration ($\approx 10^{21}\text{cm}^{-3}$) of Sr- and Mg-doped LGO [115]. In the LGO//MAO heterostructure (where $\sigma = -0.96$ C/m^2) the concentration of vacancies at a distance of 4 Å from the interface (plane 3) is more than two orders of magnitude higher than for the Sr- and Mg-doped case, either at 300 or 800 K. Since the value of σ is relatively large, the concentration of vacancies in Equation 5.10 decreases like $1/z^2$ (z is measured from plane 3) when going away from the interface into LGO bulk. Therefore, at 800 K the density of vacancies 6 Å away from the interface (plane 4) is of the same order of magnitude as in the doped bulk. For that reason, to design a nanostructure with minimal vacancy concentration similar to that of Sr- and Mg- doped bulk LGO, the total thickness of the LGO slab should be below twice 6 Å. It is likely that high ionic conductivity in the LGO//MAO system could be achieved at lower average vacancy concentrations than in the doped LGO, due to decreased interactions between the charged carriers and the dopants [83], resulting in higher mobility in the heterostructure.

From the P-B model we can also obtain the difference of potential between the interface and a point at a distance z from it in LGO as

$$\phi(z) - \phi(0) = \frac{k_B T}{e} ln \left[1 + \frac{e\sigma z}{\epsilon_r \epsilon_0 k_B T} \right]. \tag{5.11}$$

Earlier I have mentioned that one of the requirements for a good ionic conductor was the absence of any electrical conductivity. I have shown that at $T = 0$ K the LGO//MAO heterostructure remained insulating for all the different vacancy configurations (Section III.D). Now we can revisit this question in the light of the P-B formalism. In order to have electronic conductivity in the system the electrostatic energy of an electron should be enough to promote this electron from the valence to the conduction band, overcoming the bandgap. For that to happen $E_{\text{gap}} = e\,[\phi(z) - \phi(0)]$, where E_{gap} corresponds to the bandgap for bulk LGO calculated to be 3.74 eV (more than 1 eV smaller than the bandgap for MAO). Using this condition together with Equation 5.11 and solving for z, it is possible to estimate the value of the critical thickness of the LGO part of the heterostructure for which electronic conductivity will start to occur. In this case, the values I obtain for the critical thickness are well above the possible heterostructure size, even for a temperature of 1000 K, indicating that electronic conductivity would be very unlikely in the system. Therefore, according to this model, even for high temperatures our LGO//MAO heterostructure would remain insulating.

5.5 Summary

I have studied the possibility of enhancing ionic conductivity in LGO by the design of LGO//MAO heterostructures with excess negative charge in the interfacial planes. My study reveals that compensation by oxygen vacancies is a favorable mechanism for thin LGO slabs. DFT calculations for vacancies placed at different distances from the interface exhibit a non-monotonic formation energy behavior in the first three planes, followed by a nearly linear increase in energy consistent with electrostatic interactions. The vacancy formation energy was

found to be the lowest for vacancies located in the third LGO plane away from the interface. Calculated charge distributions indicate that there is no charge migration/redistribution from the negatively charged interface towards the bulk, and that the compensating vacancies exhibit a charge consistent with a charge state $V_{\mathrm{O}}^{\bullet\bullet}$. Furthermore, I showed that although there is a decrease in the bandgap, the LGO//MAO heterostructure with vacancies still remains insulating. These two conditions, i.e. the presence of charged ionic defects and the absence of electronic conductivity, are essential requirements for a good ionic conductor. Finally, based on these results, a Poisson-Boltzmann model was used in order to describe the vacancy distribution, showing that even at high temperatures most vacancies are highly localized around the first atomic planes of the LGO structure and that electronic conduction is very unlikely. In light of the recent advances in synthesis of oxide heterostructures and the encouraging first-principles results reported here, I therefore suggest that it is possible to synthesize such a heterostructure with excess negative charge at the interfaces. This is likely to lead to enhanced ionic conductivity in such a layered system.

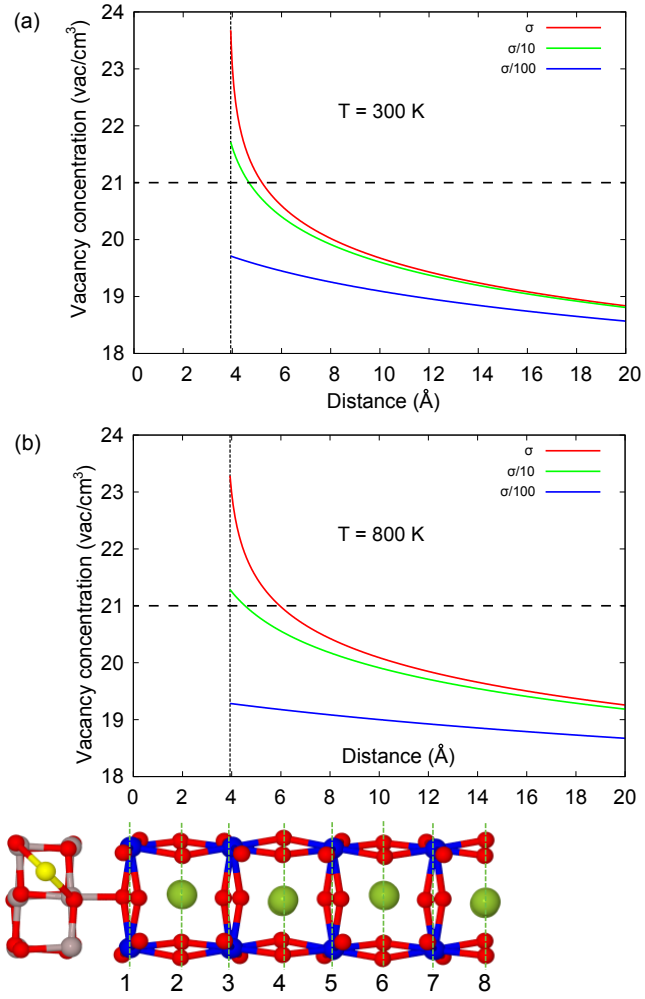

Figure 34. Poisson-Boltzmann concentration of vacancies in LGO (log scale) calculated for different charge densities at the interface and at temperatures of (a) 300, and (b) 800 K. Dashed horizontal lines correspond to the highest concentration of vacancies in Sr- and Mg-doped LGO.

CHAPTER 6

SUMMARY AND CONCLUDING REMARKS

In this thesis I have studied two different complex oxides that have potential applications in alternative-energy technologies. In Chapter 3, I investigated the electronic properties of the misfit-layered thermoelectric $Ca_3Co_4O_9$ (CCO) from first principles within the framework of Density Functional Theory. This was not a trivial task, since DFT techniques for the study of bulk materials usually rely on the periodicity of the system, which is not the case for CCO, as the structure is composed of two subsystems, rocksalt (RS) Ca_2CoO_3 and hexagonal CoO_2, which are incommensurate with each other. The approach I followed was to model the CCO structure by using Fibonacci rational approximants, which in the limiting case converge to the incommensurate stoichiometry ratio observed in the experiments. However, this is still a formidable problem. If we take into account that the smallest of these approximants contains a total of 42 atoms in its unit cell, for higher order approximants the limit of our computational capabilities is reached very soon (the largest one considered was the 13/8, with a total of 174 atoms in the unit cell). As mentioned in the introduction, although CCO has been the subject of extensive experimental studies the number of theoretical/computational studies is very scarce. In addition, the only DFT study of the electronic structure of CCO predicted the RS subsystem to be the one responsible for the electrical conductivity, while experimentally the opposite behavior was observed. In Chapter 3 of this thesis I considered two hypotheses for this disagreement. First, since previous theoretical calculations had been performed on the

lowest-order approximant, there was a possibility that this was a size effect, and that better agreement might perhaps be obtained with larger approximants. Second, earlier calculations only used plain DFT, which typically fails to give a good account of the on-site interactions due to localized d orbitals of transition metal elements, and the disagreement could have been due to the lack of a more realistic modeling of electron correlations. The main conclusion was that although the size of the approximant has indeed some effect on the electronic properties, the right physics is only captured when a Hubbard term is added to the Hamiltonian within the framework of the DFT+U method. More specifically, I found that, including correlations effects, the 5/3 approximant does a very good job of reproducing the electronic properties of CCO.

As mentioned in the Introduction, an important property that affects the figure of merit of a thermoelectric material is its thermal conductivity. In Chapter 4, I applied the conclusions of the previous chapter in order to determine the phonon modes of CCO by using DFT+U and the finite-difference methods. Here, due to the significant computational demand, I limited my study to the 3/2 and 5/3 approximants, respectively. For the 3/2 approximant, the $U = 0$ case was also considered in order to evaluate the sensitivity of the results to the value of U. With the full phonon spectra, it was then possible to compute different thermal properties, such as the constant volume heat capacity (C_v). This quantity was calculated for the 3/2 ($U = 0,5$ eV) and 5/3 approximants, obtaining in each case a very good agreement with available experimental data. Although the better agreement is obtained for the 3/2 ($U = 5$ eV) approximant, in all cases, the differences are only of a few percents. These results thus served

as an indirect validation of the method. The next step was to apply the Boltzmann transport equation (BTE) within the relaxation time approximation in order to calculate the thermal conductivity. Although the relaxation time could also be calculated from first principles, this requires the evaluation of anharmonic three phonon processes, a task impossible to achieve in a reasonable time in a such large system with current computational capabilities. Therefore, the approach I followed was to leave the relaxation time as a fitting parameter. I calculated the thermal conductivities for the 3/2 and 5/3 approximants of CCO. The main result was that both approximants are able to reproduce the large anisotropy found in the experiments between the direction perpendicular to the layering of the two subsystems and the parallel ones. However, although the two approximants agreed very well in the predicted thermal conductivities along the commensurate directions, they exhibited different behaviors along the incommensurate one. As in the study of the electronic structure (Chapter 3), here again the 5/3 approximant does a better job, since the resulting thermal conductivity with this approximant along the incommensurate direction is lower than that along the periodic direction, in good agreement with experimental findings.

Overall, most of what I presented in Chapters 3 and 4 was devoted to the development of a model that allowed the theory and the experiment to be in better agreement with each other. In the introduction I mentioned that in the case of CCO the theory lagged behind experiment. Now in the conclusion of this thesis, I would like to argue that after my studies of the electronic and thermal properties of CCO, the gap has been significantly reduced. These techniques could thus be applied in future studies of the same system in order to design new

ways of improving the thermoelectric properties of CCO. For example, by using the electronic structure determined in Chapter 3 and the BTE for electrons, both the Seebeck coefficient and the electrical conductivity can also be calculated. In this way, all the parameters involved in the figure of merit can thus be determined from first principles. Consequently, one can explore various strategies in order to increase the figure of merit of CCO, such as the effect of dopants and the effect of different stacking orders between the two subsystems. Hopefully these studies will allow the theory to lead experiment in a systematic way towards the development of better thermoelectric properties in CCO alloys and/or nanostructures.

In Chapter 5, I followed a philosophically different approach, in which my computations lead the experimental investigations. Solid oxide fuel cells (SOFCs) offer an alternative for new, cleaner and more efficient ways of generating energy. However, the high temperature at which SOFCs operate as well as the stability of their components impose severe restrictions for their applicability in modern technologies. Lower temperature SOFC are also desirable due to the fact that a higher efficiency could be attained by lowering the operational temperature. Most of the characteristics of a SOFC are determined by the solid oxide electrolyte that allows the diffusion of oxygen ions from the cathode towards the anode, thus restoring the charge balance inside the cell. One of the best candidates for intermediate temperature SOFC is the perovskite $LaGaO_3$ (LGO), which exhibits a very high ionic conductivity when either doped with Sr or Mg. However, there are several reasons to search for different alternatives to doping. First, doping typically introduces disorder, which in turns lowers the conductivity. Second, these dopants can interact with charged carriers and trap them into forming clusters, which again is detrimental

for the ionic conductivity of LGO. The idea I developed in Chapter 5 was to increase the number of ionic carriers in LGO by computational design of a heterostructure containing a negatively charged LGO//$MgAl_2O_4$ (MAO) interface. From the theory of polar interfaces it is known that such an interface requires some mechanism of charge compensation, which in this case, as explained in the introduction, was expected to be accomplished by the spontaneous formation of oxygen vacancies in LGO. This hypothesis was tested in Chapter 5, where I showed that oxygen vacancies are not only a very favorable compensation mechanism, but the LGO//MAO interface is also stable, in the sense that there is no migration of charge towards or from the interface. In addition, I verified that the LGO//MAO polar interface remains insulating, which is another prerequisite for a good ionic conductor (to be impervious to electronic conduction). In the last part of Chapter 5, I combined the Poisson-Boltzmann equation with the DFT results in order to obtain the distribution of vacancies at finite temperatures. I found that even at high temperatures, vacancies remain located in the LGO planes close to the interface region. Finally, I concluded in Chapter 5 that by synthesizing such a polar LGO//MAO heterostructure it could be possible to enhance the ionic conductivity of LGO. It is worth mentioning that experiments along these lines are presently being carried out at the Argonne National Laboratory.

Although not shown in this thesis (but following the same principles employed in Chapter 5), part of my research during my PhD was also devoted to the computational design and study of other polar interfaces, such as LGO//$CaHfO_3$ and LGO//$SrZrO_3$. Currently, I am studying metal-insulator transitions in the $SrFeO_3$//$LaFeO_3$ interface. The latter has the peculiarity of exhibiting polaron transport, which in the case of the superlattice transitions towards

electronic/hole conductivity at a much lower Sr concentration than the alloy with the same stoichiometry. In the near future my research is going to continue to focus on the computational design of complex oxide interfaces, but more specifically on systems that exhibit or may exhibit multi-ferroic phenomena. I expect that the techniques that I have learned and the expertise that I have gained during my PhD in computational materials modeling will certainly be very useful in elucidating structure/property relationships in these and many other technologically and scientifically important complex oxide materials.

CITED LITERATURE

[1] M. Varela, T. J. Pennycook, J. Gazquez, A. Y. Borisevich, S. T. Pantelides, and S. J. Pennycook. *Complex Oxide Materials*. Wiley-VCH Verlag GmbH & Co. KGaA, 2012.

[2] D. W. Bruce, D. O'Hare, and R. I. Walton. *Functional Oxides*. Inorganic Materials Series. Wiley, 2011.

[3] `http://www.depts.ttu.edu/coe/publications/envision/snapshots/wang.php`.

[4] R. Venkatasubramanian, E. Siivola, T. Colpitts, and B. O'quinn. Thin-film thermoelectric devices with high room-temperature figures of merit. *Nature*, 413(6856):597–602, 2001.

[5] T.C. Harman, P.J. Taylor, D.L. Spears, and M.P. Walsh. Thermoelectric quantum-dot superlattices with high ZT. *Journal of Electronic Materials*, 29(1):L1–L2, 2000.

[6] H. Ohta, K. Sugiura, and K. Koumoto. Recent progress in oxide thermoelectric materials: p-type $Ca_3Co_4O_9$ and n-type $SrTiO_3$. *Inorg. Chem*, 47(19):8429–8436, 2008.

[7] Y. Wang, Y. Sui, X. Wang, W. Su, and X. Liu. Enhanced high temperature thermoelectric characteristics of transition metals doped $Ca_3Co_4O_{9+\delta}$ by cold high-pressure fabrication. *Journal of Applied Physics*, 107(3):033708–033708, 2010.

[8] M. Shikano and R. Funahashi. Electrical and thermal properties of single-crystalline $(Ca_2CoO_3)_{0.7}CoO_2$ with a CaCoO structure. *Applied Physics Letters*, 82:1851, 2003.

[9] G. A. Slack and D. M. Rowe (Editor). *CRC Handbook of Thermoelectrics*. Taylor & Francis, 2010.

[10] M. Shizuya, M. Isobe, Y. Baba, T. Nagai, M. Osada, K. Kosuda, S. Takenouchi, Y. Matsui, and E. Takayama-Muromachi. New misfit-layered cobalt oxide $(CaOH)_{1.14}CoO_2$. *Journal of Solid State Chemistry*, 180(1):249–259, 2007.

[11] E. D. Wachsman and K. T. Lee. Lowering the temperature of solid oxide fuel cells. *Science*, 334(6058):935–939, 2011.

[12] T. Ishihara. *Perovskite Oxide for Solid Oxide Fuel Cells*. Fuel cells and hydrogen energy. Springer London, Limited, 2009.

[13] `http://mypages.iit.edu/~smart/garrear/fuelcells.htm`.

[14] J. Goniakowski, F. Finocchi, and C. Noguera. Polarity of oxide surfaces and nanostructures. *Reports on Progress in Physics*, 71(1), 2008.

[15] R. M. Martin. *Electronic Structure: Basic Theory and Practical Methods*. Cambridge University Press, 2004.

[16] D. P. Dreizler and E. K. U. Gross. *Density Functional Theory: an approach to the quantum many body problem*. Springer-Verlag, Germany.

[17] C. Fiolhais, F. Nogueira, and M. A. L. Marques. *A Primer in Density Functional Theory*. Lecture Notes in Physics. Springer, 2003.

[18] N. W. Ashcroft and N. D. Mermin. *Solid State Physics*. Science: Physics. Saunders College, 1976.

[19] D. J. Chadi and M. L. Cohen. Special points in the Brillouin Zone. *Physical Review B*, 8:5747–5753, 1973.

[20] J. D. Joannopoulos and M. L. Cohen. Electronic charge densities for ZnS in the wurtzite and zincblende structures. *Journal of Physics C: Solid State Physics*, 6(9):1572, 1973.

[21] H. J. Monkhorst and J. D. Pack. Special points for Brillouin-zone integrations. *Physical Review B*, 13(12):5188–5192, 1976.

[22] V. I. Anisimov, F. Aryasetiawan, and A. I. Lichtenstein. First-principles calculations of the electronic structure and spectra of strongly correlated systems: the LDA+ U method. *Journal of Physics: Condensed Matter*, 9(4):767, 1997.

[23] V. I. Anisimov, J. Zaanen, and O. K. Andersen. Band theory and mott insulators: Hubbard U instead of stoner I. *Physical Review B*, 44:943–954, 1991.

[24] A. Ohtomo, D. A. Muller, J. L. Grazul, and H. Y. Hwang. Artificial charge-modulation in atomic-scale perovskite titanate superlattices. *Nature*, 419(6905):378–380, 2002.

[25] S. Okamoto and A. J. Millis. Electronic reconstruction at an interface between a Mott insulator and a band insulator. *Nature*, 428(6983):630–633, 2004.

[26] I. Terasaki, Y. Sasago, and K. Uchinokura. Large thermoelectric power in $NaCo_2O_4$ single crystals. *Physical Review B*, 56:R12685–R12687, 1997.

[27] L. Seguin, G. Amatucci, M. Anne, Y. Chabre, P. Strobel, J. M. Tarascon, and G. Vaughan. Structural study of NiO_2 and CoO_2 as end members of the lithiated compounds by in situ high resolution x-ray powde diffraction. *Journal of Power Sources*, 81-82:604–606, 1999.

[28] R. Funahashi and I. Matsubara. Thermoelectric properties of Pb- and Ca-doped $(Bi_2Sr_2O_4)_xCoO_2$ whiskers. *Applied Physics Letters*, 79(3):362–364, 2001.

[29] I. Matsubara, R. Funahashi, M. Shikano, K. Sasaki, and H. Enomoto. Cation substituted $(Ca_2CoO_3)_xCoO_2$ films and their thermoelectric properties. *Applied Physics Letters*, 80(25):4729–4731, 2002.

[30] Y. Y. Wang, N. S. Rogado, R. J. Cava, and N. P. Ong. Spin entropy as the likely source of enhanced thermopower in $Na_xCo_2O_4$. *Nature*, 423(6938):425–428, 2003.

[31] J. Androulakis, P. Migiakis, and J. Giapintzakis. $La_{0.95}Sr_{0.05}CoO_3$: An efficient room-temperature thermoelectric oxide. *Applied Physics Letters*, 84(7):1099–1101, 2004.

[32] A. C. Masset, C. Michel, A. Maignan, M. Hervieu, O. Toulemonde, F. Studer, B. Raveau, and J. Hejtmanek. Misfit-layered cobaltite with an anisotropic giant magnetoresistance: $Ca_3Co_4O_9$. *Physical Review B*, 62:166–175, 2000.

[33] Y. Miyazaki, M. Onoda, T. Oku, M. Kikuchi, Y. Ishii, Y. Ono, Y. Morii, and T. Kajitani. Modulated Structure of the Thermoelectric Compound $[Ca_2CoO_3]_{0.62}CoO_2$. *Journal of the Physical Society of Japan*, 71(2):491–497, 2002.

[34] J. Sugiyama, J. H. Brewer, E. J. Ansaldo, H. Itahara, K. Dohmae, Y. Seno, C. Xia, and T. Tani. Hidden magnetic transitions in the thermoelectric layered cobaltite $[Ca_2CoO_3]_{0.62}[CoO_2]$. *Physical Review B*, 68:134423, 2003.

[35] W.-S. Seo, S. Lee, Y. Lee, M.-H. Lee, Y. Masuda, and K. Koumoto. High-resolution transmission electron microscopy study of $Ca_3Co_4O_9$. *Journal of Electron Microscopy*, 53(4):397–401, 2004.

[36] T. Takeuchi, T. Kondo, T. Takami, H. Takahashi, H. Ikuta, U. Mizutani, K. Soda, R. Funahashi, M. Shikano, M. Mikami, S. Tsuda, T. Yokoya, S. Shin, and T. Muro. Contribution of electronic structure to the large thermoelectric power in layered cobalt oxides. *Physical Review B*, 69:125410, 2004.

[37] Y. F. Hu, W. D. Si, E. Sutter, and Q. Li. In situ growth of *c*-axis-oriented $Ca_3Co_4O_9$ thin films on Si(100). *Applied Physics Letters*, 86(8):082103, 2005.

[38] P. Limelette, V. Hardy, P. Auban-Senzier, D. Jérome, D. Flahaut, S. Hébert, R. Frésard, Ch. Simon, J. Noudem, and A. Maignan. Strongly correlated properties of the thermoelectric cobalt oxide $Ca_3Co_4O_9$. *Physical Review B*, 71:233108, 2005.

[39] S. Bhattacharya, D. K. Aswal, A. Singh, C. Thinaharan, N. Kulkarni, S.K. Gupta, and J.V. Yakhmi. Anisotropic electrical transport studies of $Ca_3Co_4O_9$ single crystals grown by the flux method. *Journal of Crystal Growth*, 277(14):246 – 251, 2005.

[40] T. Burnus, Z. Hu, M. W. Haverkort, J. C. Cezar, D. Flahaut, V. Hardy, A. Maignan, N. B. Brookes, A. Tanaka, H. H. Hsieh, H.-J. Lin, C. T. Chen, and L. H. Tjeng. Valence, spin, and orbital state of Co ions in one-dimensional $Ca_3Co_2O_6$: An x-ray absorption and magnetic circular dichroism study. *Physical Review B*, 74:245111, 2006.

[41] H. W. Eng, P. Limelette, W. Prellier, Ch. Simon, and R. Frésard. Unconventional hall effect in oriented $Ca_3Co_4O_9$ thin films. *Physical Review B*, 73:033403, 2006.

[42] M. S. Dresselhaus, G. Chen, M. Y. Tang, R. G. Yang, H. Lee, D. Z. Wang, Z. F. Ren, J.-P. Fleurial, and P. Gogna. New directions for low-dimensional thermoelectric materials. *Advanced Materials*, 19(8):1043–1053, 2007.

[43] G. Yang, Q. Ramasse, and R. F. Klie. Direct measurement of charge transfer in thermoelectric $Ca_3Co_4O_9$. *Physical Review B*, 78:153109, 2008.

[44] H. Muguerra, D. Grebille, and F. Bourée. Disordered misfit $[Ca_2CoO_3][CoO_2]_{1.62}$ structure revisited *via* a new intrinsic modulation. *Acta Crystallographica Section B*, 64(2):144–153, 2008.

[45] Y. Wakisaka, S. Hirata, T. Mizokawa, Y. Suzuki, Y. Miyazaki, and T. Kajitani. Electronic structure of $Ca_3Co_4O_9$ studied by photoemission spectroscopy: Phase separation and charge localization. *Physical Review B*, 78:235107, 2008.

[46] T. A. Tyson, Z. Chen, Q. Jie, Q. Li, and J. J. Tu. Local structure of thermoelectric $Ca_3Co_4O_9$. *Physical Review B*, 79:024109, 2009.

[47] T. Sun, J. Ma, Q. Y. Yan, Y. Z. Huang, J. L. Wang, and H. H. Hng. Influence of pulsed laser deposition rate on the microstructure and thermoelectric properties of $Ca_3Co_4O_9$ thin films. *Journal of Crystal Growth*, 311(16):4123–4128, 2009.

[48] Q. Qiao, A. Gulec, T. Paulauskas, S. Kolesnik, B. Dabrowski, M. Ozdemir, C. Boyraz, D. Mazumdar, A. Gupta, and R. F. Klie. Effect of substrate on the atomic structure and physical properties of thermoelectric $Ca_3Co_4O_9$ thin films. *Journal of Physics-Condensed Matter*, 23(30), 2011.

[49] I. Matsubara, R. Funahashi, M. Shikano, K. Sasaki, and H. Enomoto. Cation substituted $(Ca_2CoO_3)_xCoO_2$ films and their thermoelectric properties. *Applied Physics Letters*, 80(25):4729–4731, 2002.

[50] G. J. Xu, R. Funahashi, M. Shikano, I. Matsubara, and Y. Q. Zhou. Thermoelectric properties of the Bi- and Na- substituted $Ca_3Co_4O_9$ system. *Applied Physics Letters*, 80(20):3760–3762, 2002.

[51] D. Wang, L. Chen, Q. Yao, and J. Li. High-temperature thermoelectric properties of $Ca_3Co_4O_{9+\delta}$ with Eu substitution. *Solid State Communications*, 129(9):615–618, 2004.

[52] H. Q. Liu, X. B. Zhao, T. J. Zhu, Y. Song, and F. P. Wang. Thermoelectric properties of Gd, Y co-doped $Ca_3Co_4O_{9+\delta}$. *Current Applied Physics*, 9(2):409 – 413, 2009.

[53] L. Xu, F. Li, and Y Wang. High-temperature transport and thermoelectric properties of $Ca_3Co_{4-x}Ti_xO_9$. *Journal of Alloys and Compounds*, 501(1):115 – 119, 2010.

[54] G. D. Tang, Z. H. Wang, X. N. Xu, L. Qiu, L. Xing, and Y. W. Du. Thermoelectric properties of $Ca_3Co_4O_{9+\delta}$ with Lu substitution. *Journal of Materials Science*, 45(15):3969–3973, 2010.

[55] G. D. Tang, X. N. Xu, C. P. Tang, Z. H. Wang, Y. He, L. Qiu, L. Y. Lv, L. Xing, and Y. W. Du. The spin-entropy enhancement induced by Ce doping in $Ca_3Co_4O_{9+\delta}$. *EPL*, 91(1), 2010.

[56] T. Sun, H. H. Hng, Q. Y. Yan, and J. Ma. Enhanced high temperature thermoelectric properties of Bi-doped $c-$axis oriented $Ca_3Co_4O_9$ thin films by pulsed laser deposition. *Journal of Applied Physics*, 108(8), 2010.

[57] R. Asahi, J. Sugiyama, and T. Tani. Electronic structure of misfit-layered calcium cobaltite. *Physical Review B*, 66:155103, 2002.

[58] G. D. Tang, H. H. Guo, T. Yang, D. W. Zhang, X. N. Xu, L. Y. Wang, Z. H. Wang, H. H. Wen, Z. D. Zhang, and Y. W. Du. Anisotropic thermopower and magnetothermopower in a misfit-layered calcium cobaltite. *Applied Physics Letters*, 98(20), 2011.

[59] D. P. DiVincenzo and P. J. Steinhardt. *Quasicrystals: The State of the Art.* World Scientific, Singapore, 2 edition, 1991.

[60] V. I. Anisimov, I. V. Solovyev, M. A. Korotin, M. T. Czyżyk, and G. A. Sawatzky. Density-functional theory and nio photoemission spectra. *Physical Review B*, 48:16929–16934, 1993.

[61] G. Kresse and J. Hafner. *Ab initio* molecular dynamics for liquid metals. *Physical Review B*, 47:558–561, 1993.

[62] D. M. Ceperley and B. J. Alder. Ground state of the electron gas by a stochastic method. *Physical Review Letters*, 45:566–569, 1980.

[63] J. P. Perdew, K. Burke, and M. Ernzerhof. Generalized gradient approximation made simple. *Physical Review Letters*, 77:3865–3868, 1996.

[64] S. L. Dudarev, G. A. Botton, S. Y. Savrasov, C. J. Humphreys, and A. P. Sutton. Electron-energy-loss spectra and the structural stability of nickel oxide: An LSDA+U study. *Physical Review B*, 57:1505–1509, 1998.

[65] D. J. Singh. Electronic structure of $NaCo_2O_4$. *Physical Review B*, 61:13397–13402, 2000.

[66] P. Zhang, W. Luo, V. H. Crespi, M. L. Cohen, and S. G. Louie. Doping effects on the electronic and structural properties of CoO_2: An LSDA + U study. *Physical Review B*, 70:085108, 2004.

[67] Matteo Cococcioni and Stefano de Gironcoli. Linear response approach to the calculation of the effective interaction parameters in the LDA + U method. *Physical Review B*, 71:035105, 2005.

[68] P. Giannozzi, S. Baroni, N. Bonini, M. Calandra, R. Car, C. Cavazzoni, D. Ceresoli, G. L. Chiarotti, M. Cococcioni, I. Dabo, A. Dal Corso, S. de Gironcoli, S. Fabris, G. Fratesi, R. Gebauer, U. Gerstmann, C. Gougoussis, A. Kokalj, M. Lazzeri, L. Martin-Samos, N. Marzari, F. Mauri, R. Mazzarello, S. Paolini, A. Pasquarello, L. Paulatto, C. Sbraccia, S. Scandolo, G. Sclauzero, A. P. Seitsonen, A. Smogunov, P. Umari, and R. M. Wentzcovitch. QUANTUM ESPRESSO: a modular and open-source software project for quantum simulations of materials. *Journal of Physics-Condensed Matter*, 21(39), 2009.

[69] W. Koshibae, K. Tsutsui, and S. Maekawa. Thermopower in cobalt oxides. *Physical Review B*, 62:6869–6872, 2000.

[70] G. K. H. Madsen and D. J. Singh. Boltztrap. a code for calculating band-structure dependent quantities. *Computer Physics Communications*, 175(1):67 – 71, 2006.

[71] A. Togo, F. Oba, and I. Tanaka. First-principles calculations of the ferroelastic transition between rutile-type and $CaCl_2$-type SiO_2 at high pressures. *Physical Review B*, 78:134106, 2008.

[72] D. A. Broido, M. Malorny, G. Birner, N. Mingo, and D. A. Stewart. Intrinsic lattice thermal conductivity of semiconductors from first principles. *Applied Physics Letters*, 91(23):231922, 2007.

[73] A. Ward and D. A. Broido. Intrinsic phonon relaxation times from first-principles studies of the thermal conductivities of si and ge. *Physical Review B*, 81:085205, 2010.

[74] A. Rébola, R. Klie, P. Zapol, and S. Öğüt. First-principles study of the atomic and electronic structures of misfit-layered calcium cobaltite $(Ca_2CoO_3)(CoO_2)_{1.62}$ using rational approximants. *Physical Review B*, 85:155132, 2012.

[75] H. A. Jahn and E. Teller. Stability of Polyatomic Molecules in Degenerate Electronic States. I. Orbital Degeneracy. *Royal Society of London Proceedings Series A*, 1937.

[76] T. Wu, T. A. Tyson, H. Chen, J. Bai, H. Wang, and C. Jaye. A structural change in $Ca_3Co_4O_9$ associated with enhanced thermoelectric properties. *Journal of Physics-Condensed Matter*, 24(45), 2012.

[77] I. Terasaki, H. Tanaka, A. Satake, S. Okada, and T. Fujii. Out-of-plane thermal conductivity of the layered thermoelectric oxide $Bi_{2-x}Pb_xSr_2Co_2O_y$. *Physical Review B*, 70:214106, 2004.

[78] A. Satake, H. Tanaka, T. Ohkawa, T. Fujii, and I. Terasaki. Thermal conductivity of the thermoelectric layered cobalt oxides measured by the harman method. *Journal of applied physics*, 96(1):931–933, 2004.

[79] R. A. de Souza. The formation of equilibrium space-charge zones at grain boundaries in the perovskite oxide $SrTiO_3$. *Physical Chemistry Chemical Physics (Incorporating Faraday Transactions)*, 11:9939, 2009.

[80] X. Guo and R. Waser. Electrical properties of the grain boundaries of oxygen ion conductors: Acceptor-doped zirconia and ceria. *Progress in Materials Science*, 51(2):151–210, 2006.

[81] J. Maier. Ionic conduction in space charge regions. *Progress in Solid State Chemistry*, 23(3):171 – 263, 1995.

[82] N. Sata, K. Eberman, K. Eberl, and J. Maier. Mesoscopic fast ion conduction in nanometre-scale planar heterostructures. *Nature*, 408(6815):946–949, 2000.

[83] M. S. Islam. Computer modelling of defects and transport in perovskite oxides. *Solid State Ionics*, 154155(0):75–85, 2002.

[84] M. Sase, K. Yashiro, K. Sato, J. Mizusaki, T. Kawada, N. Sakai, K. Yamaji, T. Horita, and H. Yokokawa. Enhancement of oxygen exchange at the hetero interface of (La,Sr)Co_3 /(La,Sr)$_2CoO_4$ in composite ceramics. *Solid State Ionics*, 178(35-36):1843 – 1852, 2008.

[85] M. Sase, F. Hermes, K. Yashiro, K. Sato, J. Mizusaki, T. Kawada, N. Sakai, and H. Yokokawa. Enhancement of Oxygen Surface Exchange at the Hetero-interface of (La,Sr)CoO_3/(La,Sr)$_2CoO_4$ with PLD-Layered Films. *Journal of The Electrochemical Society*, 155(8):B793–B797, 2008.

[86] K. Yashiro, T. Nakamura, M. Sase, F. Hermes, K. Sato, T. Kawada, and J. Mizusaki. Composite cathode of perovskite-related oxides, (La,Sr)$CoO_{3-\delta}$/(La,Sr)$_2CoO_{4-\delta}$, for solid oxide fuel cells. *Electrochemical and Solid-State Letters*, 12(9):B135–B137, 2009.

[87] I. Kosacki, C. M. Rouleau, P. F. Becher, J. Bentley, and D. H. Lowndes. Nanoscale effects on the ionic conductivity in highly textured YSZ thin films. *Solid State Ionics*, 176(13-14):1319 – 1326, 2005.

[88] X. Guo, E. Vasco, S. Mi, K. Szot, E. Wachsman, and R. Waser. Ionic conduction in zirconia films of nanometer thickness. *Acta Materialia*, 53(19):5161 – 5166, 2005.

[89] A. Karthikeyan, C.-L. Chang, and S. Ramanathan. High temperature conductivity studies on nanoscale yttria-doped zirconia thin films and size effects. *Applied Physics Letters*, 89(18), 2006.

[90] C. Korte, A. Peters, J. Janek, D. Hesse, and N. Zakharov. Ionic conductivity and activation energy for oxygen ion transport in superlattices-the semicoherent multilayer system YSZ (ZrO_2 + 9.5 mol% Y_2O_3)/Y_2O_3. *Phys. Chem. Chem. Phys.*, 10:4623–4635, 2008.

[91] J. García-Barriocanal, A. Rivera-Calzada, M. Varela, Z. Sefrioui, E. Iborra, C. Leon, S. J. Pennycook, and J. Santamaria. Colossal ionic conductivity at interfaces of epitaxial ZrO_2:Y_2O_3/$SrTiO_3$ heterostructures. *Science*, 321(5889):676–680, 2008.

[92] X. Guo. Comment on "Colossal Ionic Conductivity at Interfaces of Epitaxial ZrO_2:Y_2O_3/$SrTiO_3$ Heterostructures". *Science*, 324(5926):465, 2009.

[93] R. Pentcheva and W. E. Pickett. Charge localization or itineracy at $LaAlO_3$/$SrTiO_3$ interfaces: Hole polarons, oxygen vacancies, and mobile electrons. *Physical Review B*, 74:035112, 2006.

[94] R. Pentcheva and W. E. Pickett. Avoiding the Polarization Catastrophe in $LaAlO_3$ Overlayers on $SrTiO_3$(001) through Polar Distortion. *Physical Review Letters*, 102:107602, 2009.

[95] R. Pentcheva and W. E. Pickett. Electronic phenomena at complex oxide interfaces: insights from first principles. *Journal of Physics-Condensed Matter*, 22(4), 2010.

[96] V. K. Lazarov, M. Weinert, S. A. Chambers, and M. Gajdardziska-Josifovska. Atomic and electronic structure of the Fe_3O_4(111)/MgO(111) model polar oxide interface. *Physical Review B*, 72:195401, 2005.

[97] R. Oja and R. M. Nieminen. Modeling charge-imbalanced $NaNbO_3$/$SrTiO_3$ superlattices: Lattice relaxation and metallicity. *Physical Review B*, 80:205420, 2009.

[98] N. C. Bristowe, Emilio Artacho, and P. B. Littlewood. Oxide superlattices with alternating p and n interfaces. *Physical Review B*, 80:045425, 2009.

[99] T. Ishihara, H. Matsuda, and Y. Takita. Doped $LaGaO_3$ perovskite type oxide as a new oxide ionic conductor. *Journal of the American Chemical Society*, 116(9):3801–3803, 1994.

[100] H. Zheng, Q. Zhan, F. Zavaliche, M. Sherburne, F. Straub, Maria P. Cruz, L.-Q. Chen, U. Dahmen, and R. Ramesh. Controlling self-assembled perovskite-spinel nanostructures. *Nano Letters*, 6(7):1401–1407, 2006. PMID: 16834419.

[101] A. Kuwabara and I. Tanaka. First principles calculation of defect formation energies in Sr- and Mg-doped $LaGaO_3$. *The Journal of Physical Chemistry B*, 108(26):9168–9172, 2004.

[102] L. Vasylechko, A. Matkovski, A. Suchocki, D. Savytskii, and I. Syvorotka. Crystal structure of $LaGaO_3$ and (La,Gd)GaO_3 solid solutions. *Journal of Alloys and Compounds*, 286(12):213 – 218, 1999.

[103] K. E. Sickafus, J. M. Wills, and N. W. Grimes. Structure of Spinel. *Journal of the American Ceramic Society*, 82(12):3279–3292, 1999.

[104] NIST-JANAF Thermochemical Tables. `http://kinetics.nist.gov/janaf/`.

[105] J. Åhman, G. Svensson, and J. Albertsson. A reinvestigation of β-gallium oxide. *Acta Crystallographica Section C*, 52(6):1336–1338, 1996.

[106] The Mineral and Locality Database. `http://www.mindat.org/min-1136.html`.

[107] K. Ogisu, A. Ishikawa, Y. Shimodaira, T. Takata, H. Kobayashi, and K. Domen. Electronic band structures and photochemical properties of LaGa-based oxysulfides. *The Journal of Physical Chemistry C*, 112(31):11978–11984, 2008.

[108] M. L. Bortz, R. H. French, D. J. Jones, R. V. Kasowski, and F. S. Ohuchi. Temperature dependence of the electronic structure of oxides: MgO, $MgAl_2O_4$ and Al_2O_3. *Physica Scripta*, 41(4):537–541, 1990.

[109] S. M. Hosseini. Structural, electronic and optical properties of spinel $MgAl_2O_4$ oxide. *Physica Status Solidi B - Basic Solid State Physics*, 245(12):2800–2807, 2008.

[110] N. Nakagawa, H. Y. Hwang, and D. A. Muller. Why some interfaces cannot be sharp. *Nature Materials*, 5(3):204–209, 2006.

[111] A. Janotti and C. G. Van de Walle. Native point defects in ZnO. *Physical Review B*, 76:165202, 2007.

[112] J. Maier. Chemical potential of charge carriers in solids. *Zeitschrift fur Physikalische Chemie-International Journal of Research in Physical Chemistry & Chemical Physics*, 219(1):35–46, 2005.

[113] E. Fabbri, D. Pergolesi, and E. Traversa. Ionic conductivity in oxide heterostructures: the role of interfaces. *Science and Technology of Advanced Materials*, 11(5), 2010.

[114] D. C. Dube, H. J. Scheel, I. Reaney, M. Daglish, and N. Setter. Dielectric properties of lanthanum gallate ($LaGaO_3$) crystal. *Journal of Applied Physics*, 75(8):4126–4130, 1994.

[115] P. Huang and A. Petric. Superior oxygen ion conductivity of lanthanum gallate doped with strontium and magnesium. *Journal of The Electrochemical Society*, 143(5):1644–1648, 1996.

VITA

ALEJANDRO RÉBOLA

University of Illinois at Chicago, Department of Physics (M/C 273)

845 West Taylor Street, Chicago, IL 60607

E-mail: arebol2@uic.edu, Tel: (312) 413-2783, Fax: (312) 996-9016

EDUCATION

- Ph.D. in Physics: University of Illinois at Chicago, Chicago, IL (2013).

  Thesis: *First Principles Studies of Complex Oxides for Energy Applications.*

  Advisor: Prof. Serdar Öğüt.

  Co-Advisor: Dr. Peter Zapol (Argonne National Laboratory).

- M.S. in Physics: National University of Rosario, Argentina (2003).

  Thesis: *Machine Learning Modeling of Sonic Profiles in Oil Wells*

  Advisor: Prof. Alejandro Ceccatto.

- B.S. in Physics: National University of Rosario, Argentina (2002).

RESEARCH

- First Principles Studies for Enhanced Ionic Conductivity in Oxide Hetero-structures, Interface Co-doping, Metal-Insulator Transitions in $SrFeO_3/LaFeO_3$ Interfaces (Argonne National Laboratory, 2011-2013).
- Lattice and Transport Properties of the Misfit-Layered Oxide Thermoelectric $Ca_3Co_4O_9$ from First Principles (University of Illinois at Chicago, 2010-2013).
- Effects of Impurities in Magnetic Systems and Superconductors, Quantum Interference Effects between Impurities (University of Illinois at Chicago, Chicago, IL, 2008-2010)
- Machine Learning: Development of Automatic Classifiers and Non-Linear Time Series Predictors (National University of Rosario, Argentina, 2002-2003).

HONORS AND AWARDS

- Dean's Scholar Award, University of Illinois at Chicago (2012).
- James Kouvel Fellowship, University of Illinois at Chicago (2012).
- National Science Foundation Scientists, Kids and Teachers Fellowship (2008-2009).
- Fulbright Scholarship (2006-2008).

PUBLICATIONS

- A. Rébola, P. Zapol, J. Eastman, Serdar Öğüt, "First-principles study of compensation mechanisms in negatively charged $LaGaO_3/MgAl_2O_4$ interfaces", Phys. Rev. B **87**, 245117 (2013).
- A. Rébola, R. F. Klie, P. Zapol, and Serdar Öğüt,"First-principles study of the atomic and electronic structures of misfit-layered calcium cobaltite $(Ca_2CoO_3)(CoO_2)_{1.62}$ using rational approximants", Phys. Rev. B **85**, 155132 (2012).
- R. F. Klie, Q. Qiao, T. Paulauskas, A. Güleç, A. Rébola, Serdar Öğüt, J. C. Idrobo, S. T. Pantelides, S. Kolesnik, S. Dabrowski, M. Özdemir, C. Boyraz, D. Mazumdar, A. Gupta, "Observations of Co^{4+} in a Higher Spin State and the Increase in the Seebeck Coefficient of Thermoelectric $Ca_3Co_4O_9$" Phys. Rev. Lett. **108**, 196601 (2012).
- P. F. Verdes, P. M. Granitto, M. I. Szeliga, A. Rébola, and H. A. Ceccatto, "Symmetric-Embedding Prediction of the CATS Benchmark", Neurocomputing **70**, 2363 (2007).
- Acero S., Aquilano R., Ocampo S. and Rebola A., "Thin Spherically Symmetric Radiating Shells and Black Holes", Modern Physics Letters A **11**, 177 (1996)

CONTRIBUTED PRESENTATIONS

1. *Lattice and Transport Properties of the Misfit-Layered Oxide Thermoelectric $Ca_3Co_4O_9$ from First Principles.*

   APS meeting, Baltimore, MD (2013).

2. *First Principles Study of $LaGaO_3/MgAl_2O_4$ (001) Polar Interfaces.*

   APS meeting, Boston, MA (2012).

3. *First Principles Study of Misfit-Layered Calcium Cobaltite Using Fibonacci Approximants.*

   APS meeting, Dallas, TX (2011).

TEACHING EXPERIENCE

- Teaching Assistant in Physics, University of Illinois at Chicago: Assisted and instructed students in classroom and laboratory settings, prepared quizzes, graded lab reports, exams and homework, tutored undergraduate students (2006-2011).
- SKIT fellow at Chicago Public Schools: Worked along with high school teachers and students as part of an innovative program for teaching science and mathematics in urban classrooms (2008-2009).
- Teaching Assistant, Universidad Nacional de Rosario (Rosario, Argentina): Instructed students in classroom, graded exams and homework, tutored undergraduate students (2003-2006).

COMPUTATIONAL SKILLS

- Density Functional Theory codes: VASP and QUANTUM ESPRESSO.
- Miscellaneous: Fortran, Python, C, Unix shell programming, Mathematica, Latex, Boltztrap, Phonopy.

PROFESSIONAL MEMBERSHIPS

- American Physical Society (2010-Current)

LANGUAGE SKILLS

- Spanish (Native)
- English (Fluent)
- Portuguese (Fluent)
- French (Intermediate)
- Italian (Intermediate)

REFERENCES

- Prof. Serdar Öğüt

  Department of Physics

  University of Illinois at Chicago

  Phone: (312) 413-2786

  E-mail: ogut@uic.edu

- Dr. Peter Zapol

  Materials Science Division

  Argonne National Laboratory

  Phone: (630)252-6085

  E-mai: zapol@anl.gov

- Prof. Robert Klie

  Department of Physics

  University of Illinois at Chicago

  Phone: (312) 996-6064

  E-mail: rfklie@uic.edu

- Dr. Claudio Javier Gazza

  Instituto de Física Rosario (IFIR)

  Universidad Nacional de Rosario

  Department of Physics

  Phone: (+54) (341) 485-3200 ext. 127

  E-mail: gazza@ifir-conicet.gov.ar